Doctoral Thesis

Synthesis of Graphene-Based Hybrid Nanomaterials and Their Applications

Minju Park

Department of Chemical Engineering

Graduate School of UNIST

2020

Synthesis of Graphene-Based Hybrid Nanomaterials and Their Applications

Minju Park

Department of Chemical Engineering

Graduate School of UNIST

Synthesis of Graphene-Based Hybrid Nanomaterials and Their Applications

A thesis submitted to the Graduate School of UNIST
in partial fulfillment of the requirements
for the degree of Doctor of Philosophy

Minju Park

12/13/2019

Approved by

_____

Advisor
Dong-Woog Lee

Synthesis of Graphene-Based Hybrid Nanomaterials and Their Applications

Minju Park

This certifies that the thesis of Minju Park is approved.

12/13/2019

signature

_____

Advisor: Dong-Woog Lee

signature

_____

Byeong-Su Kim: Thesis Committee Member #1

signature

_____

Hyun-Kon Song: Thesis Committee Member #2

signature

_____

Guntae Kim: Thesis Committee Member #3

signature

_____

Jungki Ryu: Thesis Committee Member #4;

Abstract

This thesis describes approaches to develop new types of graphene-based nanomaterials and their practical applications in various fields. Diverse functionalities can be achieved by the chemical modification of graphene oxide (GO), which makes it easy to host and grow functional nanomaterials on the surface of graphene. Furthermore, GO-based nanomaterials can be hybridized with inorganic nanomaterials using a layer-by-layer assembly (LbL) method, which is a versatile technique to fabricate multilayer thin films. Based on these integrated nanostructures, we have explored their potential uses as additives in a non-aqueous suspension, carbocatalysts for biomass reforming, and electrocatalysts for oxygen reduction, hydrogen evolution, and biomass reforming reaction.

This thesis is divided into four parts: (1) The synthesis of GO, (2) Chemical modifications of GO for non-aqueous suspensions, (3) Graphene-based carbocatalysts for biomass reforming, and (4) a Graphene-based electrocatalyst.

The first part introduces the general experimental method for GO and its mass production. Based on the conventional synthetic process of GO, we successfully developed a synthetic process for its mass production, resulting in large amounts as well as a high-quality product.

The second part suggests various approaches for the chemical functionalization of GO with various organic molecules. Diverse functional groups of GO are easily modifiable to different structures and functionalities, thus its derivative can offer extraordinary possibilities for various utilizations. In particular, to use graphene derivatives in real applications, its dispersion stability is an important issue. Herein, we developed diverse GO-derivatives with chemical modification to improve its dispersion stability in non-aqueous suspensions.

The third part represents a GO-based carbocatalyst for biomass reforming. GO and its derivatives are promising metal-free heterogeneous catalysts due to their high surface areas and rich chemical properties. We developed a bifunctional boron-doped sulfonated graphene oxide by chemical modification and demonstrated its excellent catalytic conversion of biomass into valuable chemicals.

In the last part, various forms of graphene derivatives were fabricated and utilized as electrocatalysts for oxygen evolution reactions and electrochemical biomass reforming. A series of nitrogen-doped reduced graphene nanosheets were synthesized and exhibiting varying degrees and configurations of nitrogen depending on the type of precursors used. Furthermore, three-dimensional hybrid electrocatalytic electrodes were assembled by the LbL method toward simultaneous biomass conversion and hydrogen evolution reactions. In this research, we highlight how the nanostructure of electrocatalysts can be precisely controlled and how it affects their electrocatalytic performance.

Contents

List of Figures

Chapter 1.

Chapter 2

Chapter 3

Figure 5.3. (a) Photographs of each suspension prepared in this study (conc. 0.50 mg mL^{-1}). (b) Zeta-potential for functionalized NGO*n* derivatives as a function of pH.

Figure 5.4. Representative height-mode AFM images of (a) GO and (b) NGO3 with the corresponding line scan profiles.

Figure 5.5. Representative height-mode AFM images of NGO3 with the corresponding line scan profiles. The height of monolayer and bilayer is about 1.12 nm and 2.14 nm, respectively.

Figure 5.6. XPS survey spectra for various samples in this study. (b) Deconvoluted high-resolution XPS N1s spectra of all NRGO*n*. (c) Total N contents of NRGO*n*. (d) Schematic representation of nitrogen bonding configurations in N-doped graphene nanosheets.

Figure 5.7. (a) Linear sweep voltammograms (LSVs) of all NRGO*n* electrocatalysts prepared in the study, including that of a control set of TRGO. RDE tests were acquired at a rotation rate of 2500 rpm and a scan rate of 10 mV s^{-1} in O_2-saturated 0.10 M KOH electrolyte solution. (b) Comparison of the onset potential (white bar) and limiting current density (black bar) of each catalyst as determined by RDE experiments. Electron transfer number (*n*) based on the Koutecky-Levich equation is located on the top of the bar graph. The onset potential and limiting current were measured at -0.02 mA cm^{-2} and -0.50 V (*vs*. SCE), respectively. (c) LSVs of RRDE experiments of TRGO, NRGO3, and commercial 20 wt% Pt/C catalysts in an O_2-saturated 0.10 M KOH aqueous solution at 3200 rpm. (d) The plot of the peroxide yields (%) and the electron transfer number (*n*) of electrocatalysts.

Figure 5.8. RDE measurements at 10 mV s^{-1} scan rate in O_2-saturated 0.5 M KOH electrolyte. (a) Linear Sweep Voltammograms for (a) NRGO1, (b) NRGO2, (c) NRGO3, (d) NRGO4, (e) NRGO5, and (f) TRGO at 2500 rpm.

Figure 5.9. The chronoamperometric durability response for 10000 s with Pt/C and NRGO3. NRGO3 exhibited a slow attenuation with high current retention of 73%, which is higher than that of Pt/C in the O_2-saturated 0.1 M KOH solution at -0.25 V (*vs.* SCE) with 1600 rpm.

Figure 5.10. XPS survey spectra of (a) B-doped and (b) S-doped graphene nanosheets with corresponding deconvoluted high-resolution B1s and S2p spectra in the inset, respectively.

Figure 5.11. Schematic representation of LbL-assembled hybrid 3D multilayer thin film electrodes

toward bifunctional biomass reforming and H_2 production

Figure 5.12. TEM image of (a) DMAP-Au NPs suspension and (b) DMAP-Pd NPs suspension.

Figure 5.13. UV/vis absorbance spectra of representative (a) Au_n, (b) Pd_n, and (c) $(AuPd)_n$ multilayer thin films. The inset image shows the samples prepared with the corresponding number of bilayers (BLs, n). (d) UV/vis absorbance maxima at 215 nm for each multilayer electrode, (e) film thickness measured by surface profiler, and (f) quartz crystal microbalance (QCM) analysis of the $(AuPd)_n$ electrodes as a function of the number of BLs (n).

Figure 5.14. Architecture controlled multilayer thin film electrodes. Representative cross-sectional TEM, STEM and EDS mapping images of (a) $(AuPd)_7$, (b) Au_7/Pd_7 and (c) Pd_7/Au_7 multilayer thin film electrodes assembled on an ITO-coated substrate. (Scale bar: 50 nm)

Figure 5.15. Representative AFM images of (a) Pd_7/Au_7, (b) Au_7/Pd_7, and (c) $(AuPd)_7$ multilayer thin film electrodes. R_{rms} values of the AFM images are averaged over a 5 × 5 μm^2 area.

Figure 5.16. LSV curves of the Pd_7/Au_7 multilayer film at a scan rate of 2.0 mV s^{-1} in 1.0 M KOH with and without 10 mM HMF.

Figure 5.17. LSV curves of (a) Pd_n and (b) Au_n multilayer films electrodes according to the number of BLs, and (c) LSV curves of Au_{14} and Pd_{14} multilayer films, and (d) Comparison of the electrochemical performance toward the HMF oxidation as a function of the number of BLs. All LSVs were recorded in 1.0 M KOH with 10 mM HMF at a scan rate of 2.0 mV s^{-1}.

Figure 5.18. Electrocatalytic activity for HMF oxidation reaction of all film electrodes prepared in the study. (a) Linear sweep voltammograms (LSVs) measured at a scan rate of 2 mV s^{-1} with 10 mM HMF in 1.0 M KOH electrolyte and (b) comparison of the peak potential (black) and current density at the peak potential (gray) of each film electrode with corresponding architecture.

Figure 5.19. (a) Schematic reaction pathways for the sequential oxidation of HMF to FDCA through various reaction intermediates. (b) Yield of the final product FDCA from each electrode during the electrochemical oxidation, and (c) comparison of relative concentration ratio between HFCA and FDCA from different type of electrodes at 120 min. Reaction condition: 10 mL of 5 mM HMF in 1.0 M KOH; anode potential 0.82 V *vs.* RHE.

Figure 5.20. (a) Chromatograms for standard 5-(hydroxymethyl)furfural (HMF), 5-hydroxymethyl-2-furancarboxylic acid (HFCA), 5-formyl-2-furancarboxylic acid (FFCA), 2,5-Furandicarboxylic acid (FDCA), and 2,5-furandicarboxaldehyde (FDA) intermediates formed during the HMF oxidation measured via HPLC. (b) Representative HPLC traces of HMF oxidation catalyzed by Pd_7/Au_7 multilayer electrode at 0.82 V *vs.* RHE in 10 mL of 5 mM HMF in 1.0 M KOH.

Figure 5.21. Conversion of HMF during the electrochemical oxidation according to the reaction time. Reaction condition: 10 mL of 5 mM HMF in 1.0 M KOH; anode potential 0.82 V *vs.* RHE.

Figure 5.22. (a) Schematic reaction pathways for the sequential oxidation of HMF on Pd and Au NPs. Putative reaction mechanism with (b) Pd_7/Au_7 and (c) Au_7/Pd_7 multilayer electrodes to convert HMF to FDCA.

Figure 5.23. (a) LSV curves with Au_7/Pd_7 and Pd_7/Au_7 multilayer electrodes to convert HFCA to FDCA, and (b) FDCA yield from HFCA measured by HPLC. All LSVs were recorded in 1.0 M KOH with 10 mM HFCA at a scan rate of 2.0 mV s^{-1}.

Figure 5.24. LSV curves for the Pd_7/Au_7 electrode in 1.0 M KOH with and without 10 mM HMF at a scan rate of 2.0 mV s^{-1}.

Figure 5.25. Electrocatalytic activity for HER. (a) Linear sweep voltammograms (LSVs) of all electrodes prepared in the study at a scan rate of 2 mV s^{-1} with 10 mM HMF in 1.0 M KOH electrolyte, and (b) comparison of the onset potential (black bar) with current density at -0.2 mA cm^{-2} and current density at -0.4 V *vs.* RHE (gray bar) of each electrode .

Figure 5.26. The corresponding Tafel plot of HER in Figure 5.25(a). Inset numbers represent the slope of each plots.

Figure 5.27. Schematic description of HER mechanism with (a) $(AuPd)_7$, (b) Pd_7/Au_7, and (c) Au_7/Pd_7 multilayer electrodes. Gray balls with solid line represent adsorbed H (H_{ads}) and desorbed H with dashed line

Figure 5.28. Nyquist plots of three different multilayered film electrodes (Au_7/Pd_7, Pd_7/Au_7, and $(AuPd)_7$) measured in a frequency range of 100 kHz to 50 mHz at -0.276 V (*vs*. RHE) in 1.0 M KOH with 10 mM HMF.

Figure 5.29. (a) Illustration of the optimized two-electrode full-cell system in this study to simultaneous generation of H_2 in cathode and FDCA in anode. (b) LSV curves of two-electrode full-cell system for HMF oxidation in 1.0 M KOH solution with 10 mM HMF using a scan rate of 2.0 mV s^{-1}. (c) Schematic description of $(AuPd)_7$ multilayer electrode for cathode and Pd_7/Au_7 multilayer for anode. Gray balls with solid line represent adsorbed H (H_{ads}) and desorbed H with dashed line.

Figure 5.30. (a) Schematic description of photo-electrocatalytic HMF oxidation with Pd_7/Au_7 electrode. (b) LSV curves for HMF oxidation with and without irradiation.

List of Tables

Chapter 2

Chapter 3

Chapter 4

Chapter 1.
Introduction of Carbon-Based Nanomaterials

1.1. Carbon-Based Nanomaterials

Although metal-based materials have been playing a critical role for various industrial processes, they still suffer from multiple disadvantages, including their high cost, limited resources, corrosion phenomenon, and toxicity on the environment.[1] To overcome these limitations, carbon-based nanomaterials are considered as a fascinating system to replace metal-based materials. Since carbon atoms can participate in diverse hybridization states (sp, sp^2, sp^3), it enables to form multi-dimensional structures such as 0-dimensional (0D) fullerene, carbon dots (CDs), and nanodiamonds, 1D carbon nanotubes (CNTs), 2D graphene, and 3D graphite (**Figure 1.1**).[2] Not only diverse dimensionalities, their unique features such as remarkable mechanical, electronic, optical, and chemical properties make carbon-nanomaterials have been recently demonstrated to be promising metal-free alternatives in various applications.

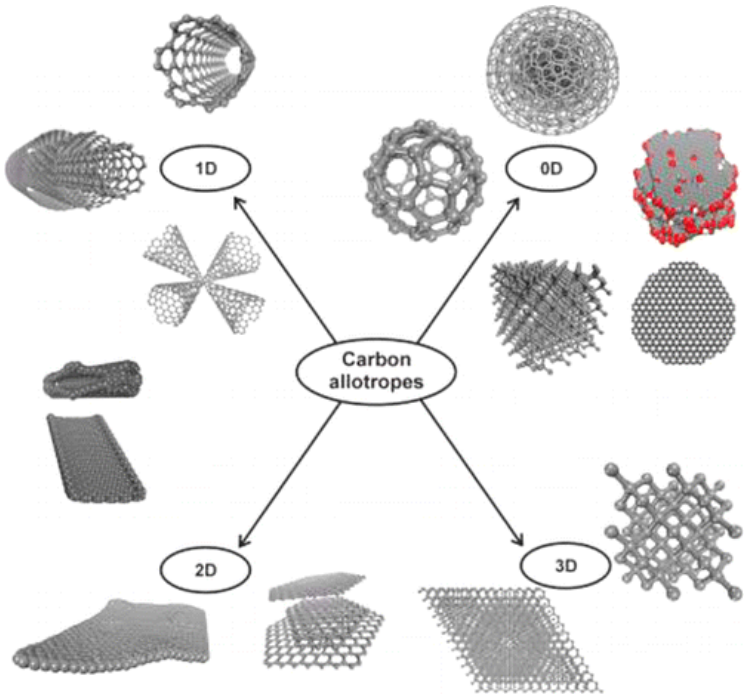

Figure 1.1. Representative illustration of multidimensional carbon derivatives.[3] Reprinted with permission from *Chem. Rev.* **2015,** *115*, 4744-4822. Copyright 2015 American Chemical Society.

1.2. Graphene and Graphene Oxide (GO)

Among carbon-based nanomaterials, it is undeniable that graphene is the most promising carbon allotropes due to its extraordinary properties. Graphene consists of a one-atom thick 2D sheet comprising sp^2 bonded carbon structure. Its extended π-conjugated network yields unique thermal, mechanical, and electrical properties.[4-6] Single-layer graphene was theoretically demonstrated by Wallace *et al*. in 1947, however, it is hard to realize, because 2D materials were thought to be thermodynamically unstable at finite temperatures.[7] In 2004, Geim et al. firstly isolated single-layer graphene from graphite by mechanical exfoliation.[8] This led to an explosion of interest about graphene to probe intrinsic properties and utilize in various applications. Pristine graphene exhibits outstanding electrical, mechanical, and chemical properties such as high electrical conductivity (1738 S/m), high mobility (15000 $cm^2/V{\cdot}s$), low density (0.77 mg/m^3), and large surface area (2630 m^2/g).[8-9] Nevertheless, pristine graphene is hard to chemically modify or utilize in various applications due to their inactive structure. Moreover, expensive process and aggregation issues remain a critical limitation for the large-scale utilization of graphene. To explore the unique properties of graphene and further extend its practical application, defective graphene, graphene oxide (GO) offers an attractive means to develop reliable and cost-effective synthetic methods for solution-processable graphene derivatives.[10]

Generally, GO is synthesized by the Hummers' method by the oxidative treatment of graphite (**Figure 1.2**), which yields oxidize graphene nanosheets decorated with epoxide and hydroxyl groups on the basal plane and carboxyl and carbonyl groups at the edge sites (**Figure 1.3**(a)).[10-14] Compared with pristine graphene, the oxygenated functional groups in GO make remarkable structural defects on the surface. This is accompanied with some loss of electrical conductivity, which possibly limits the application of GO in electrically active devices. On the other hand, the presence of functional groups can provide potential advantages for using GO in numerous other applications. The oxygen-containing functional groups make GO strongly hydrophilic and provide excellent solvent dispersity.[15] Thus, these advantages are beneficial for processing and further utilization of GO. Moreover, the resulting GO suspension can be deposited on various substrates to prepare multilayer thin films such as spin-coating,[16-17] spraying,[18] drop casing,[19] or layer-by-layer (LbL) assembly.[20-21] These methods can be applied for efficient electrodes or catalysts materials.

Furthermore, functional groups of GO could be easily modifiable with a wide range of structures and functionalities (**Figure 1.3**(b)).[22] Using well known chemical strategies, GO can be employed to functionalize various organic molecules and inorganic nanomaterials through covalent or noncovalent bonding. Therefore, its derivatives can be designed and applied to diverse applications such as catalysts, devices, sensors, and bio-applications.[10, 23-25]

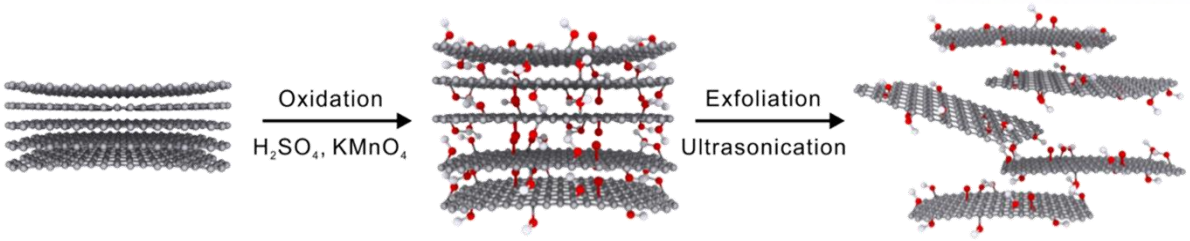

Figure 1.2. Synthesis of GO by Hummers' method from graphite flake.

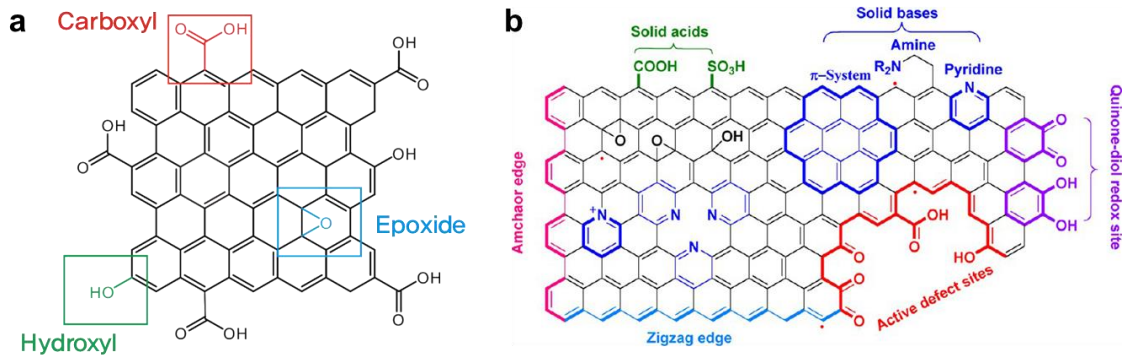

Figure 1.3. (a) Oxygen-containing functional groups of GO including carboxylic acid groups, hydroxyl groups, and epoxide groups, and (b) diverse functionalities of GO-derivatives by chemical modification.[22] Reprinted with permission from *Acc. Chem. Res.* **2013,** *46*, 2275-2285. Copyright 2013 American Chemical Society.

1.3. Chemical Modification of Carbon-Based Nanomaterials

The chemically exfoliated GO nanosheets possess oxygenated functional groups such as hydroxyl and epoxy groups on the basal planes and carboxylic and ketone groups at the edge sites. The presence of various functional groups renders GO excellent platforms for hosting or growing the other functional materials through chemical modification including covalent or noncovalent functionalization.

Specifically, using well known coupling agents, GO can be functionalized with various small molecules. For example, carboxylic acid groups can be activated with several agents using N-ethyl-N'-(3-dimethylaminopropyl)carbodiimide methiodide (EDC),[26] thionyl chloride ($SOCl_2$),[27-28] N,N'-Dicyclohexylcarbodiimide (DCC),[29] carbonyldiimidazole (CDI),[30-31] or 1-[Bis(dimethylamino)-methylene]-1H-1,2,3-triazolo[4,5-b]pyridinium 3-oxide hexafluoro-phosphate (HATU).[32] Subsequent addition of nucleophilic species, such as amines or hydroxyls, produce covalently attached functional groups with graphene oxide *via* the formation of amides or esters. In this thesis, we utilize EDC and CDI-mediated coupling reactions, which is widely used to couple carboxylic acid groups and amine molecules. At first, EDC is a cross-linking agent to react carboxylic acid groups with amine groups, producing amide bonds (**Figure 1.4** and **Figure 1.5**). One of the main advantages of EDC is water solubility, which allows direct conjugation of GO suspensions without prior organic solvent dissolution. Moreover, the excess of reagents and byproducts can be easily removed by dialysis process. In contrast, CDI is a useful coupling agent in organic solvent. Although the reactivity of CDI is less than that of acid chlorides ($SOCl_2$), it is more easily handled and avoids the formation of acid chloride, which can cause side reactions. During this reaction, the amide bond is formed between carboxylic acid groups and amine groups with CO_2 formation as a driving force (**Figure 1.6**).

In addition to various kinds of coupling agents, GO itself can react with small molecules by well-known synthetic strategies. For example, the phenylsulfonic acid group can be directly functionalized on to graphene lattice by anchoring sulfonic acid-containing aryl radicals *via* diazonium chemistry.[33-34] Since phenylsulfonic acid group has a very low pK_a value (-6.62), this negative charge group induces a significant repulsive force between the graphene nanosheets. Therefore, the highly charged sulfonate group may prevent the aggregation of graphitic sheets improve dispersion stability in various solvents. Furthermore, epoxy groups decorating on the basal plane of the GO nanosheets can be tailored with hydroxyl groups under basic condition. Base provides strong nucleophilic moieties and they can attack epoxy groups by S_N2 reaction process.[35] Functionalization mainly occurred on the surface of the graphene nanosheets; thus, it represents different properties compared with functionalization with carboxylic acid groups.

After chemical modification, the successful functionalization of each molecule on the GO nanosheets was confirmed by zeta potential, UV/visible absorbance, Fourier-transform infrared spectroscopy (FT-IR), and X-ray photoelectron spectroscopy (XPS).

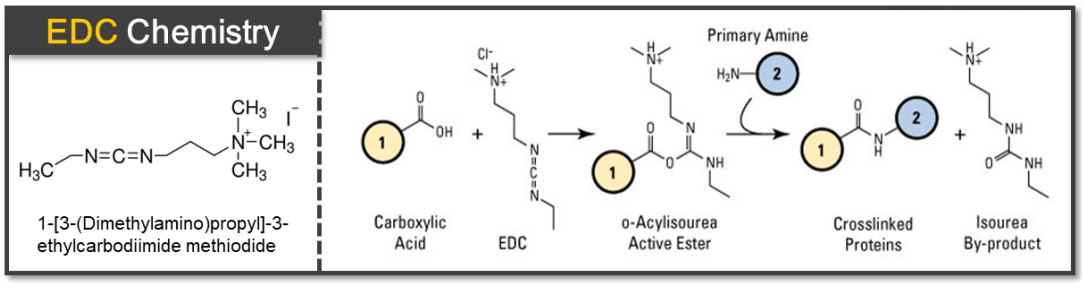

Figure 1.4. General reaction pathway through EDC chemistry with carboxylic acid and amine functional groups.

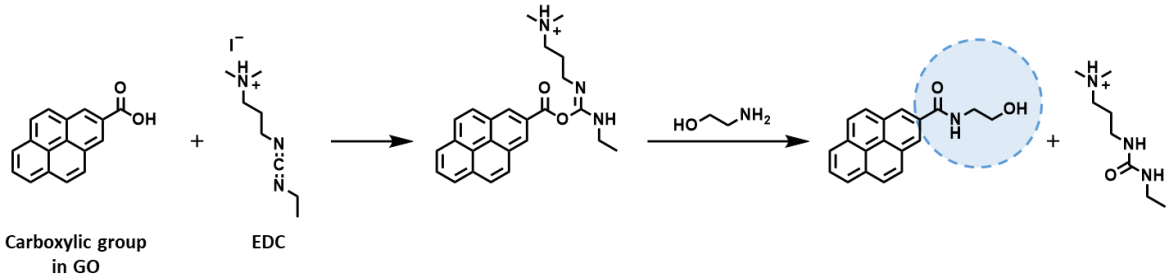

Figure 1.5. Reaction mechanism between carboxylic acid group in GO and amine molecules with the EDC coupling agent.

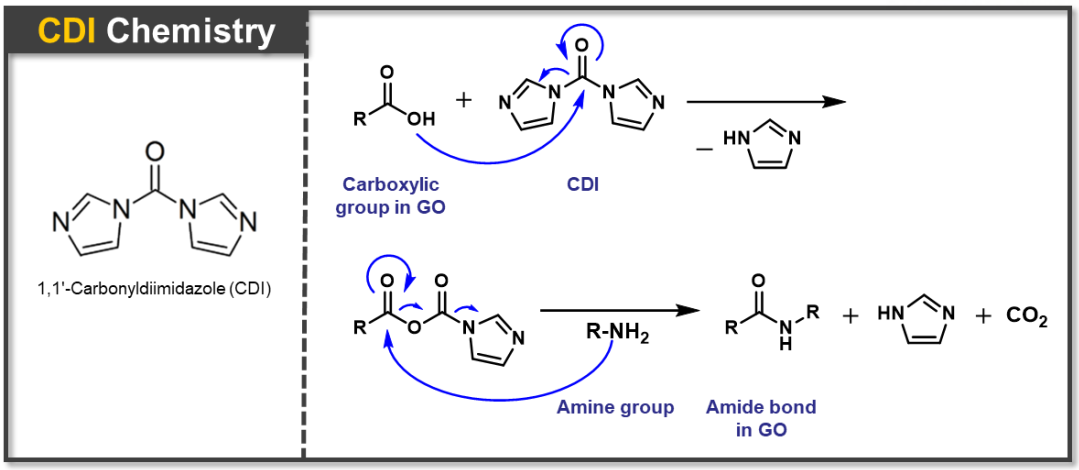

Figure 1.6. Reaction mechanism between carboxylic acid group in GO and amine molecules with the CDI coupling agent.

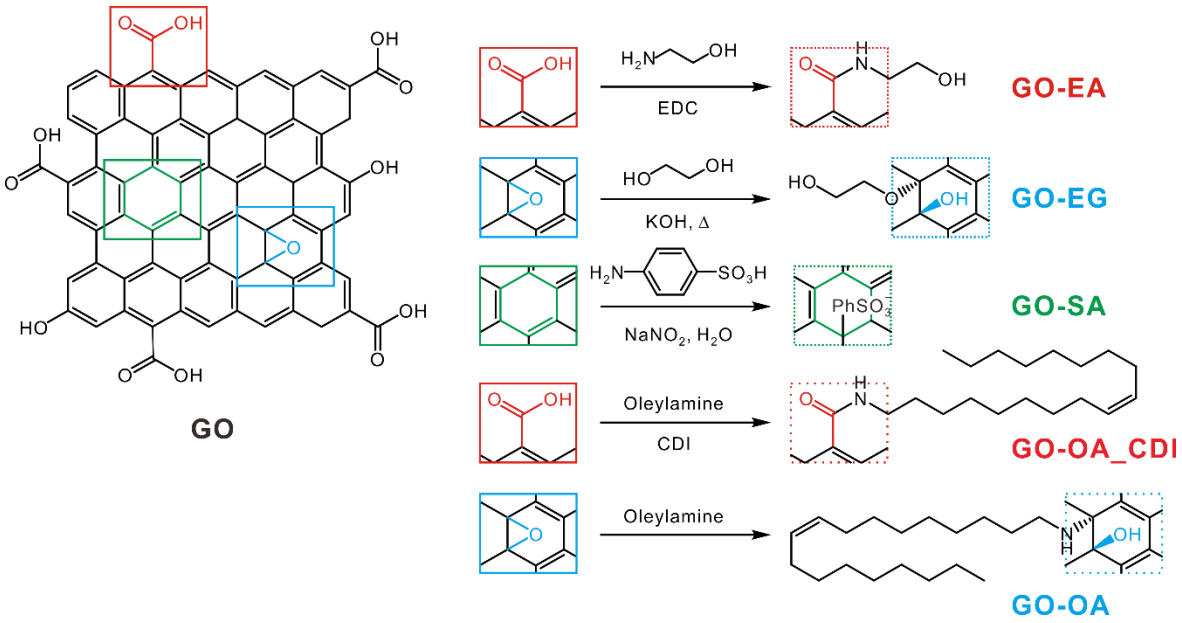

Figure 1.7. Various approaches to chemically functionalize GO with organic molecules.

1.4. Hybrid Graphene-Based Nanomaterials

To date, a broad range of novel materials such as organic molecules, inorganic nanomaterials, polymers, and biomaterials have been reported for various hybridization based on GO. Not only chemical modification, GO is an ideal template to hybridize metal nanoparticles or organic molecules owing to their abundant functional groups and large surface area.[36-37] To synthesize hybrid nanomaterials, *ex situ* hybridization is a representative method, which immobilizes as-prepared metal nanoparticles and GO by covalent or noncovalent interactions such as van der Waals interaction, hydrogen bonding, π-π stacking, or electrostatic interaction. One possible approach is layer-by-layer (LbL) assembly, which can make 3D hybrid multilayer structure. The LbL assembly is versatile method for fabricating thin film, and it is assembled through sequential adsorption of oppositely charged components by attractive forces such as electrostatic interactions and hydrogen bonding (**Figure 1.8**).[36] Thus, the highly ordered and multilayered architectures can be manufactured reproducibly by LbL assembly, allowing nano-scale level control of thickness and composition of hybrid nanomaterials. Furthermore, in addition to achieving nanoscale uniformity, the LbL technique can preserve the unique characteristics of constituent materials and impart synergetic effects between its diverse conjugate materials (**Figure 1.9**).

Based on this knowledge, graphene-based nanomaterials can be complexed with the counterpart such as other carbon materials, polymers or inorganic nanomaterials, and utilized in various applications including catalysts, electrodes, sensors, energy storage and conversion system, and bio applications. Especially, graphene-based LbL assembly was first demonstrated by Kotov et al. in 1996 with graphite oxide platelets and polyelectrolytes.[38] After a remarkable achievement on the physical properties of graphene sheets by Geim, Novoselov, and other significant interests in graphene, many researchers have devoted significant effort to the field of graphene-based nanocomposite thin films.[8] In this thesis, we focus on graphene-based LbL films prepared by the electrostatic interactions between negatively charged GO and positively charged nanoparticles.

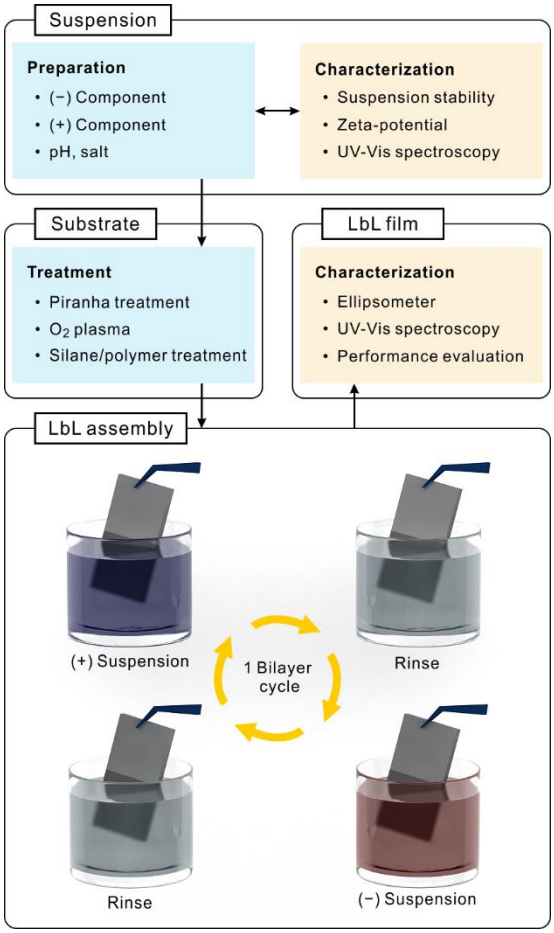

Figure 1.8. General workflow and illustration of LbL assembly.[37] Reprinted with permission from *Chem. Mater.* **2017,** *29*, 69-79. Copyright 2017 American Chemical Society.

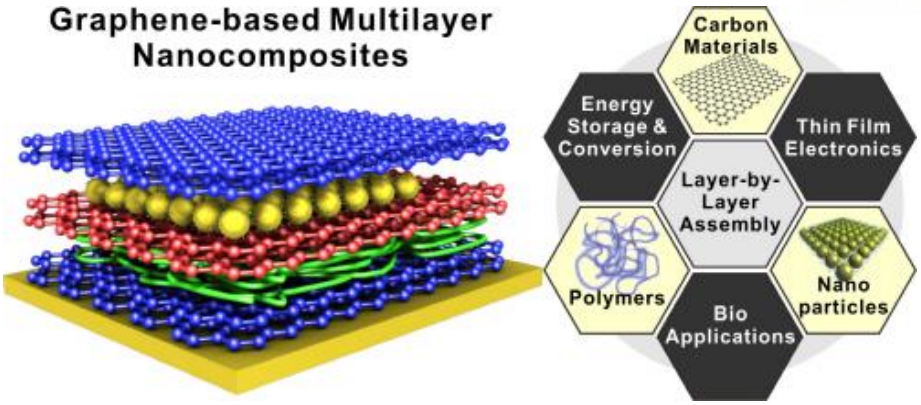

Figure 1.9. Schematic illustration of graphene-based multilayer nanocomposites and the potential applications.[36] Reprinted with permission from *Chem. Mater.* **2015,** *27*, 3785-3796. Copyright 2015 American Chemical Society.

1.5. Overview of Thesis

This thesis, comprised of 5 chapters, describes graphene-based hybrid nanomaterials and their potential applications in various fields.

Chapter 2 provides a detailed description of the synthesis of GO and the general experimental characterizations used in this thesis. Specifically, GO was prepared by a modified Hummers' method of graphite oxidation. Moreover, we demonstrated how to develop a synthetic method for the mass production of GO with an extensively low level of impurities. In addition, Chapter 2 gives a brief background on the procedures used to characterize graphene-based nanomaterials, including zeta potential, ultra-violet/visible spectrum (UV/vis) absorbance, Fourier-Transform-Infrared spectroscopy (FT-IR), inductively coupled plasma atomic emission spectroscopy (ICP-AES), and atomic force microscopy (AFM).

Chapter 3 introduces the chemical modification of GO and its utilization in non-aqueous suspensions. To improve the dispersion stability in organic solvents such as ethylene glycol (EG) and commercial oil, GO is covalently functionalized with EG-like molecules and a long aliphatic chain. Moreover, this chapter describes a new analytical method for the assessment of dispersion stability and successfully quantifies the instability index based on transmission profiles under centrifugation cycles.

Chapter 4 demonstrates the utilization of GO-derivatives as carbocatalysts in an organic reaction. In particular, bifunctional boron-doped sulfonated graphene oxide (BS-GO) was developed to demonstrate its excellent catalytic performance for biomass reforming. Furthermore, this chapter investigates the origin of the catalytic active sites and successfully unveils the catalytic mechanism.

Chapter 5 investigates the electrocatalytic applications of GO-based nanomaterials. In Chapter 5.2, nitrogen-doped GO-derivatives are synthesized and utilized as electrocatalysts in an oxygen reduction reaction (ORR). As a series of nitrogen-doped GO-derivatives exhibited varying degrees and configurations of nitrogen, this chapter clearly demonstrates the relation between the electrocatalytic performance and the structures of the GO-derivatives. Chapter 5.3 introduces the nanoarchitectonics of GO-based multilayers with an LbL assembly method. GO-based multilayer films are fabricated with nanosized GO, Au, and Pd nanoparticles and they are applied to an electrocatalytic reaction for simultaneous biomass reforming and hydrogen production. This chapter highlights how the internal architecture of LbL multilayer electrodes can be precisely controlled and affect their electrocatalytic performance by its nanoarchitecture.

1.6. References

(1) Yu, D.; Nagelli, E.; Du, F.; Dai, L., Metal-Free Carbon Nanomaterials Become More Active Than Metal Catalysts and Last Longer. *J. Phys. Chem. Lett.* **2010,** *1*, 2165-2173.

(2) Hirsch, A., The Era of Carbon Allotropes. *Nat. Mater.* **2010,** *9*, 868-871.

(3) Georgakilas, V.; Perman, J. A.; Tucek, J.; Zboril, R., Broad Family of Carbon Nanoallotropes: Classification, Chemistry, and Applications of Fullerenes, Carbon Dots, Nanotubes, Graphene, Nanodiamonds, and Combined Superstructures. *Chem. Rev.* **2015,** *115*, 4744-4822.

(4) Geim, A. K.; Novoselov, K. S., The Rise of Graphene. *Nat. Mater.* **2007,** *6*, 183-191.

(5) Sun, Y.; Wu, Q.; Shi, G., Graphene Based New Energy Materials. *Energy Environ. Sci.* **2011,** *4*, 1113-1132.

(6) Nair, R. R.; Blake, P.; Grigorenko, A. N.; Novoselov, K. S.; Booth, T. J.; Stauber, T.; Peres, N. M. R.; Geim, A. K., Fine Structure Constant Defines Visual Transparency of Graphene. *Science* **2008,** *320*, 1308-1308.

(7) Wallace, P. R., The Band Theory of Graphite. *Phys. Rev.* **1947,** *71*, 622-634.

(8) Novoselov, K. S.; Geim, A. K.; Morozov, S. V.; Jiang, D.; Zhang, Y.; Dubonos, S. V.; Grigorieva, I. V.; Firsov, A. A., Electric Field Effect in Atomically Thin Carbon Films. *Science* **2004,** *306*, 666-669.

(9) Stankovich, S.; Dikin, D. A.; Dommett, G. H. B.; Kohlhaas, K. M.; Zimney, E. J.; Stach, E. A.; Piner, R. D.; Nguyen, S. T.; Ruoff, R. S., Graphene-Based Composite Materials. *Nature* **2006,** *442*, 282-286.

(10) Dreyer, D. R.; Park, S.; Bielawski, C. W.; Ruoff, R. S., The Chemistry of Graphene Oxide. *Chem. Soc. Rev.* **2010,** *39*, 228-240.

(11) Hummers, W. S.; Offeman, R. E., Preparation of Graphitic Oxide. *J. Am. Chem. Soc.* **1958,** *80*, 1339-1339.

(12) Chen, D.; Feng, H.; Li, J., Graphene Oxide: Preparation, Functionalization, and Electrochemical Applications. *Chem. Rev.* **2012,** *112*, 6027-6053.

(13) Dikin, D. A.; Stankovich, S.; Zimney, E. J.; Piner, R. D.; Dommett, G. H. B.; Evmenenko, G.; Nguyen, S. T.; Ruoff, R. S., Preparation and Characterization of Graphene Oxide Paper. *Nature* **2007,** *448*, 457-460.

(14) Stankovich, S.; Dikin, D. A.; Piner, R. D.; Kohlhaas, K. A.; Kleinhammes, A.; Jia, Y.; Wu, Y.; Nguyen, S. T.; Ruoff, R. S., Synthesis of Graphene-Based Nanosheets Via Chemical Reduction of Exfoliated Graphite Oxide. *Carbon* **2007,** *45*, 1558-1565.

(15) Li, D.; Müller, M. B.; Gilje, S.; Kaner, R. B.; Wallace, G. G., Processable Aqueous Dispersions of Graphene Nanosheets. *Nat. Nanotechnol.* **2008,** *3*, 101-105.

(16) Robinson, J. T.; Zalalutdinov, M.; Baldwin, J. W.; Snow, E. S.; Wei, Z.; Sheehan, P.; Houston, B. H., Wafer-Scale Reduced Graphene Oxide Films for Nanomechanical Devices. *Nano Lett.* **2008,** *8*, 3441-3445.

(17) Robinson, J. T.; Perkins, F. K.; Snow, E. S.; Wei, Z.; Sheehan, P. E., Reduced Graphene Oxide Molecular Sensors. *Nano Lett.* **2008,** *8*, 3137-3140.

(18) Gilje, S.; Han, S.; Wang, M.; Wang, K. L.; Kaner, R. B., A Chemical Route to Graphene for Device Applications. *Nano Lett.* **2007,** *7*, 3394-3398.

(19) Schniepp, H. C.; Li, J.-L.; McAllister, M. J.; Sai, H.; Herrera-Alonso, M.; Adamson, D. H.; Prud'homme, R. K.; Car, R.; Saville, D. A.; Aksay, I. A., Functionalized Single Graphene Sheets Derived from Splitting Graphite Oxide. *J. Phys. Chem. B* **2006,** *110*, 8535-8539.

(20) Zhu, Y.; Tour, J. M., Graphene Nanoribbon Thin Films Using Layer-by-Layer Assembly. *Nano Lett.* **2010,** *10*, 4356-4362.

(21) Yu, A.; Park, H. W.; Davies, A.; Higgins, D. C.; Chen, Z.; Xiao, X., Free-Standing Layer-by-Layer Hybrid Thin Film of Graphene-MnO_2 Nanotube as Anode for Lithium Ion Batteries. *J. Phys. Chem. Lett.* **2011,** *2*, 1855-1860.

(22) Su, C.; Loh, K. P., Carbocatalysts: Graphene Oxide and Its Derivatives. *Acc. Chem. Res.* **2013,** *46*, 2275-2285.

(23) Ahn, E. C.; Wong, H. S. P.; Pop, E., Carbon Nanomaterials for Non-Volatile Memories. *Nat. Rev. Mater.* **2018,** *3*, 18009.

(24) Pyun, J., Graphene Oxide as Catalyst: Application of Carbon Materials Beyond Nanotechnology. *Angew. Chem. Int. Ed.* **2011,** *50*, 46-48.

(25) Georgakilas, V.; Tiwari, J. N.; Kemp, K. C.; Perman, J. A.; Bourlinos, A. B.; Kim, K. S.; Zboril, R., Noncovalent Functionalization of Graphene and Graphene Oxide for Energy Materials, Biosensing, Catalytic, and Biomedical Applications. *Chem. Rev.* **2016,** *116*, 5464-5519.

(26) Liu, Z.; Robinson, J. T.; Sun, X.; Dai, H., Pegylated Nanographene Oxide for Delivery of Water-Insoluble Cancer Drugs. *J. Am. Chem. Soc.* **2008,** *130*, 10876-10877.

(27) Niyogi, S.; Bekyarova, E.; Itkis, M. E.; McWilliams, J. L.; Hamon, M. A.; Haddon, R. C., Solution Properties of Graphite and Graphene. *J. Am. Chem. Soc.* **2006,** *128*, 7720-7721.

(28) Liu, Z.-B.; Xu, Y.-F.; Zhang, X.-Y.; Zhang, X.-L.; Chen, Y.-S.; Tian, J.-G., Porphyrin and Fullerene Covalently Functionalized Graphene Hybrid Materials with Large Nonlinear Optical Properties. *J. Phys. Chem. B* **2009,** *113*, 9681-9686.

(29) Veca, L. M.; Lu, F.; Meziani, M. J.; Cao, L.; Zhang, P.; Qi, G.; Qu, L.; Shrestha, M.; Sun, Y.-P., Polymer Functionalization and Solubilization of Carbon Nanosheets. *Chem. Commun.* **2009**, 2565-2567.

(30) Kim, H.; Kim, W. J., Photothermally Controlled Gene Delivery by Reduced Graphene Oxide–Polyethylenimine Nanocomposite. *Small* **2014,** *10*, 117-126.

(31) Kim, H.; Lee, D.; Kim, J.; Kim, T.-i.; Kim, W. J., Photothermally Triggered Cytosolic Drug Delivery Via Endosome Disruption Using a Functionalized Reduced Graphene Oxide. *ACS Nano* **2013,** *7*, 6735-6746.

(32) Mohanty, N.; Berry, V., Graphene-Based Single-Bacterium Resolution Biodevice and DNA Transistor: Interfacing Graphene Derivatives with Nanoscale and Microscale Biocomponents. *Nano Lett.* **2008,** *8*, 4469-4476.

(33) Si, Y.; Samulski, E. T., Synthesis of Water Soluble Graphene. *Nano Lett.* **2008,** *8*, 1679-1682.

(34) Englert, J. M.; Dotzer, C.; Yang, G.; Schmid, M.; Papp, C.; Gottfried, J. M.; Steinrück, H.-P.; Spiecker, E.; Hauke, F.; Hirsch, A., Covalent Bulk Functionalization of Graphene. *Nat. Chem.* **2011,** *3*, 279-286.

(35) Park, M.; Song, K.; Lee, T.; Cha, J.; Lyo, I.; Kim, B.-S., Tailoring Graphene Nanosheets for Highly Improved Dispersion Stability and Quantitative Assessment in Nonaqueous Solvent. *ACS Appl. Mater. Interfaces* **2016,** *8*, 21595-21602.

(36) Lee, T.; Min, S. H.; Gu, M.; Jung, Y. K.; Lee, W.; Lee, J. U.; Seong, D. G.; Kim, B.-S., Layer-by-Layer Assembly for Graphene-Based Multilayer Nanocomposites: Synthesis and Applications. *Chem. Mater.* **2015,** *27*, 3785-3796.

(37) Ahn, E.; Lee, T.; Gu, M.; Park, M.; Min, S. H.; Kim, B.-S., Layer-by-Layer Assembly for Graphene-Based Multilayer Nanocomposites: The Field Manual. *Chem. Mater.* **2017,** *29*, 69-79.

(38) Kotov, N. A.; Dékány, I.; Fendler, J. H., Ultrathin Graphite Oxide–Polyelectrolyte Composites Prepared by Self-Assembly: Transition between Conductive and Non-Conductive States. *Adv. Mater.* **1996,** *8*, 637-641.

Chapter 2.

Graphene Oxide: Synthesis and Characterizations

2.1. Introduction

Recently, most researches have used the Hummers' method to synthesize GO through combination of potassium permanganate and sulfuric acid.[1] When permanganate is reacted with sulfuric acid, dark green oil, known as dimanganese heptoxide, is formed (equation (1) and (2)).[2-4] Mn_2O_7 can selectively oxidize unsaturated aliphatic double bonds in aromatic lattice during oxidation of graphite.

$$KMnO_4 + 3H_2SO_4 \rightarrow K^+ + MnO_3^+ + H_3O^+ + 3HSO_4^- \quad (1)$$

$$MnO_3^+ + MnO_4^- \rightarrow Mn_2O_7 \quad (2)$$

The most widely accepted structure of GO is the Lerf-Klinowski model.[5] According to this structure, epoxide and hydroxyl groups are decorated at the basal plane of GO, while carboxylic acids, carboxylates, or several hydroxyl groups present on the edge sites. In addition, the strong oxidants break graphene sheets into small pieces, and make more functional groups and defects on the graphene lattice. Since strong oxidants react randomly with graphite, the structure of GO varies depending on the oxidation conditions and the graphite precursor. Flake graphite is commonly used for carbon source. Additionally, sheet size of GO can be tunable according to the carbon precursor. For example, in our previous researches, nanosized graphene sheets (nGO) were successfully synthesized from a graphite nanofiber.[6] Average dimension of conventional GO is about 0.37 μm^2, in contrast, nGO represents the much smaller dimension about 0.17 μm^2.

Until now, the precise atomic structure of GO is still ambiguous due to the nonstoichiometric functional groups and atomic compositions. Nevertheless, oxygenated functional groups of GO render it good dispersion stability in many solvents, thus, it can be beneficial for processing and further derivatization in numerous applications. In addition, using well-known chemical strategy, functional groups can be customized as well as employed to immobilize diverse active nanomaterials through covalent or noncovalent interactions. Therefore, the chemical uniqueness of GO, which can be chemically, thermally, or electrochemically engineered, allows the diverse tunability of its intrinsic properties.[7]

To utilize GO in practical applications, it is essential to develop advanced technique for large-scale production of GO. In this thesis, we successfully developed the synthetic method for mass production of GO. Chapter 2 represents experimental methods for the preparation of GO as well as large-scale GO, and their characterizations. More specific details are described in the following chapters.

2.2. Experimental

2.2.1. Typical synthetic method for GO (Conventional GO)

2.2.1.1. Pretreatment of graphite

GO is synthesized from graphite powder (Sigma Aldrich, < 20 μm) by a modified Hummers' method. As a pretreatment step to ensure complete oxidation, graphite powder (1.0 g), $K_2S_2O_8$ (0.5 g), and P_2O_5 (0.5 g) are mixed with 3.0 mL of concentrated H_2SO_4 until the reactants are completely dissolved. The mixture is heated at 80 °C for 4.5 h and diluted with 500 mL of DI water after reaction. After that, the product is filtered and washed with DI water to remove remained acid. The solid is transferred to a drying dish and left overnight under ambient conditions.

2.2.1.2. Oxidation of graphite

The pretreated graphite, which is black color, is added to the 26 mL of H_2SO_4 and stirred until well dispersed. $KMnO_4$ (3.0 g) is added slowly in an ice bath, ensuring the temperature remained below 10 °C. During this step, dark green oil is represented due to the formation of dimanganese heptoxide. After that, the mixture is reacted at 35 °C for 2 h. As following, DI water (46 mL) is added in an ice bath. The color of mixture is changed from dark green to dark brown in this process. Then, the mixture reacts at 35 °C for 2 h. To quench the oxidation step after reaction, the mixture is diluted with 140 mL of DI water and H_2O_2 (30%, 2.5 mL) is added, resulting in a brilliant yellowish solution with bubbling. The product is settled down at least a day, and clear supernatant is decanted. As following, the mixture is filtered and washed with 500 mL of HCl soliton (10%) to remove remained metal composition. The resulting solid is dried at the 25 °C and diluted with DI water to dialysis for 2 weeks to remove remaining metals and reagents. Finally, the product is centrifuged with vigorous washing with water, and dark brown GO powder is obtained through drying at 50 °C in vacuum oven for a day.

2.2.2. Mass production for GO (Large-scale GO)

2.2.2.1. Pretreatment of graphite

Synthetic method for large-scale GO is almost similar with conventional method except purification process. As a pretreatment step, $K_2S_2O_8$ (7.5 g) and P_2O_5 (7.5 g) are mixed in 500 mL round bottom flask using a funnel. Concentrated H_2SO_4 (40 mL) is added and stirred until the reactants are completely dissolved. The mixture is heated at 80 °C for 10-15 min in the water bath and graphite powder (10 g) is added to the mixture. The mixture is reacted 80 °C for 4.5 h and transferred into a 2.0 L Erlenmeyer flask to dilute with DI water (1.0 L). After that, the product is filtered and washed with DI water to remove remained acid. In this step, collected powder is continuously rinsed until pH 7. The solid is transferred to a drying dish and left overnight under ambient conditions.

2.2.2.2. Oxidation of graphite

In 2.0 L of Erlenmeyer flask, H_2SO_4 (375 mL) is poured and the flask is placed in an ice bath until temperature reaches around 5 °C (about 30-40 min). The pretreated graphite is added to flask and stirred until mixture is fully well dispersed. $KMnO_4$ (50 g) is added slowly in an ice bath, ensuring the temperature remained below 10 °C. After that, the mixture is reacted at 35 °C for 3 h. As following, chilled DI water (1.0 L) is prepared in an ice bath. The reacted mixture is transferred to the ice bath and waiting to chill. When the mixture is cooled, chilled water is slowly poured into the oxidized reaction mixture (Total addition time should take between 1.5 to 2 h). Then the mixture is finally diluted with 2.0 L of DI water and H_2O_2 solution (35%, 40 mL) is slowly added until bubble formation is ceased. The product is settled down at least a day, and clear supernatant is decanted.

2.2.2.3. Purification

The precipitation is transferred to the 500 mL of centrifuge bottles and dispersed in diluted HCl solution (3.0%). The mixture is centrifuged at 5000 rpm for 10 min, repeating the centrifugation three more times. After the final decanting, the product is transferred to a 1.0 L of bottle and re-dispersed with dilute HCl (3.0%) up to a 1.0 L volume. Prepared graphite oxide is stored in HCl solution at 4 °C to avoid additional reduction. In this process, approximately more than 20 g of graphite oxide can be prepared.

2.2.2.4. Exfoliation

The required amount of graphite oxide is transferred from the stored bottle and diluted with DI water (concentration: 2.0-3.0 g/L). The mixture is centrifuged at 8500 rpm for 10 min and redispersed in DI water. The centrifugation is repeated until pH of decanting water is greater than 6. After ultrasonication process, the product is centrifuged at 500 rpm for 30 min. Finally GO suspension is collected after discarding the pellet.

2.2.3. Synthesis of nGO

The synthetic process for nanosized graphene oxide (nGO) is identical with conventional GO except the graphite precursor. As a pretreatment step to ensure complete oxidation, graphite nanofiber (1.0 g), $K_2S_2O_8$ (0.75 g), and P_2O_5 (0.75 g) are mixed with 5.0 mL of concentrated H_2SO_4 until the reactants are completely dissolved. Following process is same with synthesis of GO described in Chapter 2.2.1.

2.3. Results and Discussion

In general, the characterize chemical functionality and atomic composition of GO, Fourier-transform infrared spectroscopy (FT-IR), X-ray photoelectron spectroscopy (XPS), inductively coupled plasma optical emission spectroscopy (ICP-OES), and elemental analysis (EA) have been used to qualitatively and quantitatively identify the surface composition. To verify the quality of Large-scale GO, it was confirmed by various investigations. In **Figure 2.1**, the FT-IR spectra revealed that the conventional GO displayed characteristic peaks of oxygen functional groups at ~3200, 1730, 1407, 1224, and 1047 cm^{-1}, which is corresponding to O-H stretching, C=O stretching, O-H bending, C-O epoxy, and C-O alkoxy bonding, respectively (**Table 2.1**). Moreover, C=C aromatic stretching peak is appeared at 1626 cm^{-1}. Along with the same line, Large-scale GO represents the completely same FT-IR spectra with conventional GO. This result indicates that large-scale GO was well synthesized and oxygenated functional groups were well introduced onto the graphite surface.

The atomic composition of conventional GO and Large-scale GO is investigated with XPS measurement. As shown in **Table 2.2**, oxygen containing functional groups are successfully introduced in both conventional GO and Large-scale GO. Moreover, small amount of sulfur is detectable in conventional GO about 2.15%, because mass sulfur-containing reagent (H_2SO_4) is used for preparing GO. In case of Large-scale GO, the remained sulfur is almost completely removed rather than conventional GO due to the considerable purification process.

Additionally, we confirmed the complete removal of metal salts in graphite oxide by ICP-OES, which is another critical issue to qualify GO. The remaining impurities could neutralize charge of GO, thereby increasing aggregation and destabilization in solvents.[8] Moreover, residual metal can dramatically alter the electronic, catalytic, and electrochemical properties of graphene. Therefore, it is necessary to remove residual metal completely. According to precious research, the main impurities in GO are Mn, Fe, and K.[9] In this regard, the concentration of three metal impurities are measured by ICP-OES. As shown in **Table 2.3**, the levels of metal impurities in our experiment are significantly lower than those reported in other studies.[10-11] Furthermore, Large-scale GO represents much lower impurities value than that of conventional GO.

AFM images demonstrated that both conventional GO and Large-scale GO were mainly composed of a monolayer of graphene nanosheets with an average thickness of 0.9 ± 0.03, and 1.45 ± 0.10 nm, respectively (**Figure 2.2**). Thus, all these measurements confirmed that GO was successfully synthesized in large scale as well as high quality with extremely low contents of metal impurities.

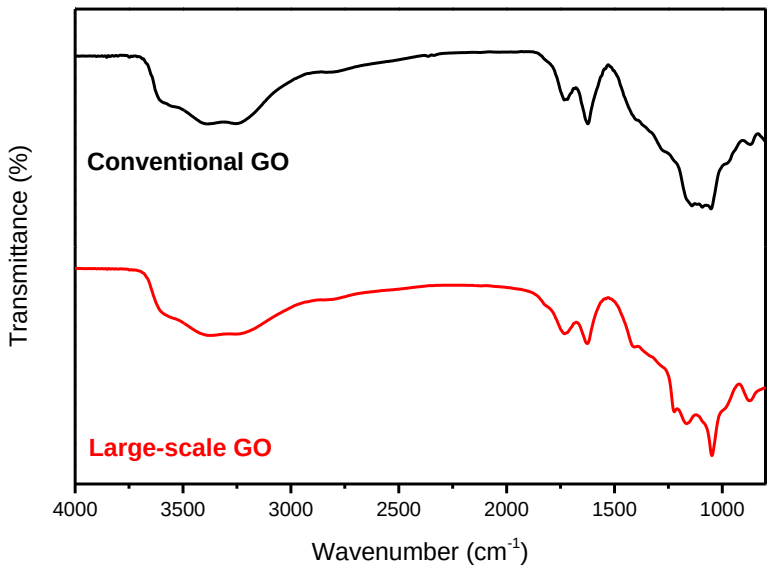

Figure 2.1. FT-IR spectra of GO synthesized by conventional method and large-scale production.

Table 2.1. Characteristic Peaks Table of GO with FT-IR Measurement.

Wavenumber (cm^{-1})	Strength	Assignment
3200 ~	Broad	O-H stretching (H-bonded –OH)
1730	Weak	C=O stretching (Carbonyl/carboxyl)
1626	Medium	C=C stretching (C=C aromatics)
1407	Strong	O-H bending
1224	Strong	C-O epoxy
1047	Strong	C-O alkoxy

Table 2.2. Relative Atomic Ratio (%) Based on XPS Measurement.

	Conventional GO	Large-scale GO
C1s	66.88	71.09
O1s	30.56	27.42
N1s	0.28	0.27
S2p	2.15	0.68
C/O ratio	2.19	2.59

Table 2.3. The Concentration of Metal Impurities (ppm) in Respective GO Solution.

	Conventional GO	Large-scale GO	Reference[9]
Mn	0.223	0.043	2290
Fe	0.164	0.031	82
K	0.364	0.095	820

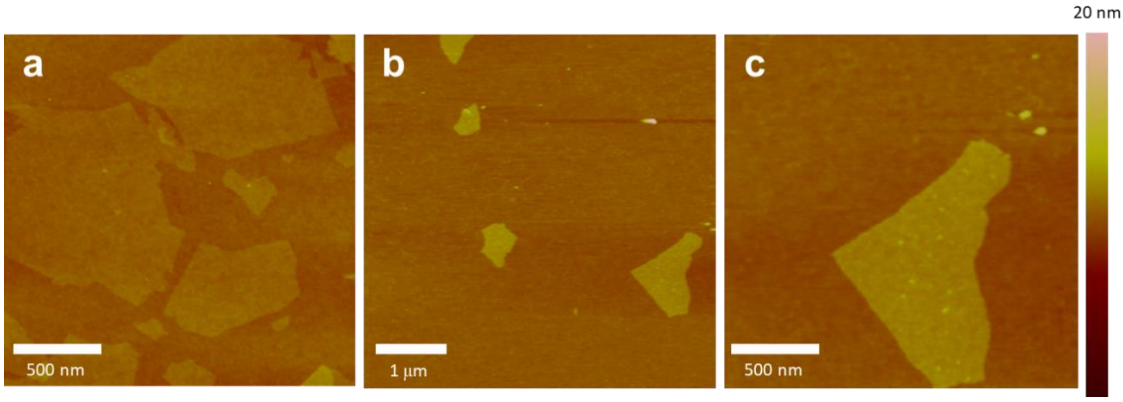

Figure 2.2. Representative AFM images of (a) conventional GO and (b), (c) Large-scale GO. All GO samples were deposited on a silicon wafer from an aqueous dispersion.

2.4. Conclusion

In summary, we successfully developed the synthetic method for mass production of GO. To verify the quality of Large-scale GO, it was confirmed by various investigations including FT-IR, XPS, ICP-OES, and AFM. All these measurements clearly represented that Large-scale GO was successfully synthesized with similar quantitative oxygenated functional groups compared with conventional GO. Moreover, the quality of Large-scale GO was highly improved with significant lower contents of metal impurities rather than that of previous reported results.

2.5. References

(1) Hummers, W. S.; Offeman, R. E., Preparation of Graphitic Oxide. *J. Am. Chem. Soc.* **1958,** *80*, 1339-1339.

(2) Koch, K. R., Oxidation by Mn207: An Impressive Demonstration of the Powerful Oxidizing Property of Dimanganeseheptoxide. *J. Chem. Edu.* **1982,** *59*, 973.

(3) Dimiev, A. M.; Tour, J. M., Mechanism of Graphene Oxide Formation. *ACS Nano* **2014,** *8*, 3060-3068.

(4) Kang, J. H.; Kim, T.; Choi, J.; Park, J.; Kim, Y. S.; Chang, M. S.; Jung, H.; Park, K. T.; Yang, S. J.; Park, C. R., Hidden Second Oxidation Step of Hummers Method. *Chem. Mater.* **2016,** *28*, 756-764.

(5) Lerf, A.; He, H.; Forster, M.; Klinowski, J., Structure of Graphite Oxide Revisited. *J. Phys. Chem. B* **1998,** *102*, 4477-4482.

(6) Gu, M.; Choi, J.; Lee, T.; Park, M.; Shin, I.-S.; Hong, J.; Lee, H.-W.; Kim, B.-S., Diffusion Controlled Multilayer Electrocatalysts Via Graphene Oxide Nanosheets of Varying Sizes. *Nanoscale* **2018,** *10*, 16159-16168.

(7) Eda, G.; Chhowalla, M., Chemically Derived Graphene Oxide: Towards Large-Area Thin-Film Electronics and Optoelectronics. *Adv. Mater.* **2010,** *22*, 2392-2415.

(8) Li, D.; Müller, M. B.; Gilje, S.; Kaner, R. B.; Wallace, G. G., Processable Aqueous Dispersions of Graphene Nanosheets. *Nat. Nanotechnol.* **2008,** *3*, 101-105.

(9) Wong, C. H. A.; Sofer, Z.; Kubešová, M.; Kučera, J.; Matějková, S.; Pumera, M., Synthetic Routes Contaminate Graphene Materials with a Whole Spectrum of Unanticipated Metallic Elements. *Proc. Natl. Acad. Sci. USA* **2014,** *111*, 13774-13779.

(10) Wang, L.; Ambrosi, A.; Pumera, M., "Metal-Free" Catalytic Oxygen Reduction Reaction on Heteroatom-Doped Graphene Is Caused by Trace Metal Impurities. *Angew. Chem. Int. Ed.* **2013,** *52*, 13818-13821.

(11) Su, C.; Acik, M.; Takai, K.; Lu, J.; Hao, S.-j.; Zheng, Y.; Wu, P.; Bao, Q.; Enoki, T.; Chabal, Y. J.; Ping Loh, K., Probing the Catalytic Activity of Porous Graphene Oxide and the Origin of This Behaviour. *Nat. Commun.* **2012,** *3*, 1298.

Chapter 3.

Chemical Modification of Graphene Oxide for Non-Aqueous Suspensions

3.1. Introduction

To explore the unique features of graphene and further extend its practical application, GO its derivatives offer an attractive means of developing reliable and cost-effective synthetic methods for solution-processable graphene. To apply graphene derivatives in real applications, dispersion stability is an important issue. Hydrophilic functional groups of GO provide good dispersion stability in water; however, aggregation is still observed at high concentrations, and it becomes more severe in organic solvents. This problem brings technical limitations for the fabrication of graphene-based materials in organic solvents. Therefore, it is necessary to develop stable graphene suspensions in organic media for practical applications. Many approaches have been proposed to improve the dispersion stability of GO. For example, GO is functionalized with alkyl chain[1] and polymer[2] to be dispersed in organic media. However, the problem is that they only have worked in low concentration ranges. Furthermore, typical analysis for the long-term suspension stability has been limited to visual observation without quantified stability values. To overcome these challenges, herein, we developed diverse GO-derivatives with chemical functionalization to improve dispersion stability in non-aqueous suspensions.

3.2. Tailoring Graphene Derivatives for Superior Dispersion Stability and Quantitative Assessment

3.2.1. Abstract

Aggregation is a critical limitation for the practical application of graphene-based materials. Herein, we report that graphene oxide (GO) nanosheets chemically modified with ethanolamine (EA), ethylene glycol (EG), and sulfanilic acid (SA) demonstrate superior dispersion stability in organic solvents, specifically EG, based on the differences in their covalent chemistries. Functionalized GO was successfully dispersed in EG at a concentration of 9.0 mg mL^{-1} (0.50 vol%), the highest dispersion concentration reported to date. Moreover, our study introduces a unique analytical method for the assessment of dispersion stability and successfully quantifies the instability index based on transmission profiles under centrifugation cycles. Interestingly, GO-EG and GO-EA exhibited highly improved dispersion stabilities approximately 96 and 48 times greater than that of GO in EG solvent, respectively. This finding highlights the critical role of surface functional groups in the enhancement of chemical affinity and miscibility in the surrounding media. We anticipate that the novel structural designs and unique tools presented in this study will further the understanding and application of chemically functionalized carbon materials.

[*] Chapter 3.2 is reproduced in part with permission from Park, M.; Song, K.; Lee, T.; Cha, J.; Lyo, I.; Kim, B.-S., *ACS Appl. Mater. Interfaces* **2016**, *8*, 21595-21602. Copyright 2016 American Chemical Society.

3.2.2. Introduction

While graphene has attracted significant interest due to its unique structure and outstanding properties, aggregation remains a critical obstacle for the large-scale application of pristine graphene.[3-6] To explore the unique features of graphene and further extend its practical application, chemically modified graphene, such as graphene oxide (GO) and reduced graphene oxide (rGO) suspensions, offer an attractive means of developing reliable and cost-effective synthetic methods for solution-processable graphene derivatives. GO is synthesized by the oxidative treatment of graphite, which yields oxidized graphene sheets decorated with hydroxyl and epoxide groups on the basal plane and carbonyl and carboxyl groups at the edge.[7] The presence of oxygen-containing functional groups renders GO strongly hydrophilic and provides excellent aqueous dispersity; however, aggregation is still observed at relatively high concentrations due to van der Waals interactions between the basal planes of the graphene nanosheets. Moreover, irreversible aggregation becomes more severe in organic solvents due to the disruption of hydrogen bonds between the oxygen functional groups and the solvent.[8] This phenomenon inhibits the solvent-philicity of GO and often poses technical difficulties for the fabrication of graphene-based materials and devices using organic solvents. Therefore, the large-scale production of graphene suspensions that are stable at high concentrations is important for practical applications.[9-13]

A number of approaches have been proposed to improve the dispersion stability of GO in both aqueous and organic media, including the addition of stabilizing molecules or surfactants on the surface of graphene, surface modification of the graphene sheet, and solvent exchange.[14-17] For example, Ruoff and co-workers reported a solvent exchange method to disperse rGO in organic solvents.[18] Furthermore, covalent functionalization of the surface of graphene has been suggested to improve its dispersion stability in various organic solvents.[2, 8, 17, 19-20] Despite their widespread use, many approaches have only been implemented in relatively low concentration ranges (typically 0.1–1.0 mg mL^{-1}, maximum of 3.6 mg mL^{-1}, **Table 3.1**). Furthermore, analysis of the long-term suspension stability has been limited to either visual inspection or turbidity- and UV/vis-based optical characterization, which inevitably require diluted concentrations with unquantified stability values.

Herein, we present three different covalent functionalization approaches to improve the dispersion stability of GO nanosheets in non-aqueous solvent. Among the many organic solvents, ethylene glycol (EG) was selected as the target testbed due to its miscibility with water and its widespread usage in antifreeze and coolants for heat transfer systems.[21-24] Moreover, when coupled with the outstanding thermal and mechanical properties of graphene-based structures, GO dispersion will open promising avenues for future nanofluids for thermal management applications.[21, 25-27] Specifically, we introduced three types of molecules, including ethanolamine, ethylene glycol, and phenyl sulfonate groups, onto the GO nanosheets to demonstrate how the dispersion stability could be

tailored by varying the functional molecules. Furthermore, another objective of this study was to provide an unequivocal assessment of the dispersion stability of functionalized GO nanosheets in both aqueous and non-aqueous solvents. The results reveal that the superior dispersion stability of functionalized GO nanosheets can be compared in a quantitative manner, which has been largely unexplored to date. We believe that this method provides a versatile strategy to achieve functionalized GO nanosheets with high dispersion stability in a desired solvent through the appropriate choice of functional group.

3.2.3. Experimental

3.2.3.1. Preparation of GO Suspension and Covalent Surface Modification

Initially, graphite oxide powder was prepared by the oxidation of graphite (Sigma-Aldrich, <20 μm) using a modified Hummer's method and exfoliated to give a brown dispersion of graphene oxide (GO) under ultrasonication (typical concentration of 1.00 mg mL^{-1}). For the chemical functionalization of the carboxylic acid groups of GO with ethanolamine (GO-EA), 50 mL of the pristine GO suspension was reacted with 10 mL of EA in the presence of 1.0 g *N*-ethyl-*N*'-(3-dimethyl aminopropyl)carbodiimide methiodide (EDC) for 12 h at room temperature, followed by extensive dialysis (SpectraPore MWCO 12–14 K) for 4 days to remove any byproducts and remaining reactants. Ethylene glycol-functionalized GO (GO-EG) was synthesized by the reaction of the epoxy group of GO and EG. A 5.0 mL of EG was mixed with 0.3 g of potassium hydroxide at 50 °C for 1 h, and the mixture was added to 50 mL of GO suspension. After the reaction, the purification steps were identical to the process for GO-EA. Sulfonate graphene oxide (GO-SA) was synthesized through an aryl diazonium reaction of sulfanilic acid. The aryl diazonium salt was prepared from the reaction of 460 mg of sulfanilic acid and 200 mg of sodium nitrite in 100 mL of water (the mixture turned yellow as the reaction proceeded). After 7.0 mL of 1.0 M HCl solution was added to this mixture in an ice bath under stirring, the yellow color of the reaction mixture disappeared, and the dispersion was stored in the ice bath for over 2 h.[28-29] After the reaction, the purification steps were identical to the process for GO-EA.

3.2.3.2. Stability Test

The stability of the functionalized GO dispersions was investigated by observing the sedimentation behavior under centrifugation at 4000 rpm (2300 *g*) using a LUMiFuge LF 111 instrument (L.U.M. GmbH, Berlin, Germany). Initially, the functionalized GO suspensions were freeze-dried to remove water and then redispersed in water and EG at a concentration of 9.0 mg mL^{-1} by ultrasonication. The dispersions were transferred to measuring tubes, and an optoelectronic sensor system enabled the spatial and temporal changes in the light transmission to be monitored during the centrifugation. The temperature was held constant at 25 °C, and the local transmission was determined over the entire sample. Thus, the instability index and the velocity of the sedimentation were investigated simultaneously based on the transmission profiles of the samples. The red lines represent the transmission profiles in the early stages, and the green lines correspond to later stages. It was possible to describe the separation process based on the time and relative position under centrifugation and to trace the overall separation processes.[30]

3.2.3.3. Characterizations

The ζ-potential of the colloidal suspensions was measured using a ζ-potential analyzer (Malvern, Zetasizer nano-zs). The elemental analyzer (Flash 2000) was used to determine the relative atomic composition, which was used to determine the structure of the unknown compound after the chemical modification of GO. FT-IR spectroscopy was used to determine the chemical structure and bonding of the functionalized GO materials with ATR-mode (Varian 670). The surface morphologies of the GO and functionalized GO were examined using an atomic force microscope (AFM, Dimension D3100, Veeco). The average thickness was calculated by choosing 30 random points, and the average area was calculated by a SemAfore 5.21 program with 20 random nanosheets. X-ray photoelectron spectroscopy (XPS, Thermo Fisher, K-alpha) was used to detect the elemental composition and the chemical state of the functionalized GO dispersions. The stability of the dispersions was investigated using a LUMiFuge LF 111 instrument (L.U.M. GmbH, Berlin, Germany). The concentrations of impurities were quantified using inductively coupled plasma optical emission spectroscopy (ICP-OES, 700-ES, Varian) in triplicate, and the average value was used in this study. The rheological behavior was determined using a Haake MARS III instrument, which measures viscosity as a function of shear rate. The temperature was maintained at room temperature.

3.2.4. Results and Discussion

3.2.4.1. Preparation of GO-Derivatives through Covalent Functionalization.

The GO nanosheet was prepared by the oxidation of graphite according to a modified Hummers' method.[31] The chemical functional groups introduced on the surface of the graphene nanosheet, including carboxylic acids, phenolic alcohols, and epoxy groups, rendered the GO suspension negatively charged over a wide range of pH conditions (ζ-potential of −40 mV).[32] In the initial stage of our work, we prepared a series of GO nanosheets chemically functionalized with three different molecules as following, ethanolamine (EA), ethylene glycol (EG), and sulfanilic acid (SA) (**Figure 3.1**). These molecules were introduced to enhance the dispersion stability of graphene nanosheets in the target solvent based on the differences in their covalent chemistries.

First, *N*-ethyl-*N*'-(3-dimethylaminopropyl)carbodiimide methiodide (EDC)-mediated surface functionalization of GO was achieved through the reaction of carboxylic acids and the amine groups of EA, and the product is denoted hereafter as GO-EA. In our previous studies, identical methods have been successfully integrated to introduce various amine functional molecules onto the surface of GO.[33-35] Because the carboxylic acid groups are mostly located at the edge, functionalized EA was predominantly attached at the edge of the graphene nanosheets. Second, graphene oxide functionalized with EG (GO-EG) was synthesized through the reaction of epoxy groups and hydroxyl groups under basic conditions. Epoxy groups decorate on the basal plane of the GO nanosheets; therefore, functionalization mainly occurred on the surface of the graphene nanosheets. We postulate that EG-like molecules, such as EA and EG, would improve the dispersion stability in EG solvent due to the similarity of their molecular structures. Furthermore, we demonstrated how the dispersion stability could be enhanced by varying the location of the functional groups. Finally, sulfonated graphene oxide (GO-SA) was prepared by directly anchoring sulfonic acid-containing aryl radicals to the surface of graphene sheets via diazonium chemistry.[28, 36] The phenylsulfonic acid group has a very low pK_a (−6.62),[37] and this negative charge of the sulfonate group induces a significant repulsive force between the graphene nanosheets. For this reason, the highly charged sulfonate groups of GO-SA may prevent the graphitic sheets from aggregating and thereby improve their water solubility. By synthesizing these three different GOs, we demonstrate how the dispersion stability can be enhanced by varying the location and chemical structure of the functionalized molecules.

3.2.4.2. Characterization of GO-Derivatives.

The successful functionalization of each molecule on the GO nanosheet was confirmed by FT-IR and X-ray photoelectron spectroscopy (XPS) (**Figure 3.2**). The FT-IR spectra revealed that the

pristine GO displayed three characteristic peaks at 3200–3500, 1725, and 1315 cm^{-1} corresponding to the hydroxyl (OH), carboxylic acid (COOH), and epoxy (C–O–C) groups, respectively.[38-40] The functionalized GO-EA and GO-EG exhibited two additional peaks at 2966 and 2865 cm^{-1}, indicating asymmetric and symmetric stretching modes of C-H bonds from ethylene spacer group in ethanolamine and ethylene glycol, respectively.[41] The peak intensity of the carboxylic acid was considerably lower after the functionalization of GO-EA, leading to the formation of an amide bond with EA at around 1640 cm^{-1}. Since the location of peak with conjugated C=C bond and amide bond was overlapped, it was hard to deconvoluted, however, the overall peak intensity was clearly increased. A decrease in the epoxy band was also observed in both GO-EA and GO-EG, which indicates that the ring-opening reaction of epoxides was inevitable with excess amine and alkoxide groups. In a separate reaction of GO-SA, peaks were observed at 1382 and 1072 cm^{-1}, corresponding to respective asymmetric and symmetric S=O stretching, confirming the presence of the sulfonic acid group.[28] In order to further analyze the atomic composition of the functionalized GO nanosheets, XPS and elemental analysis were performed. As shown in **Figure 3.2**(b), we found a distinct evolution of nitrogen peak in GO-EA (approximately 6.7 at.%), while negligible nitrogen content was detected in GO, GO-EG, and GO-SA. In accordance with the XPS analysis, elemental analysis data confirmed the successful introduction of the functional groups onto the GO nanosheet (**Table 3.2**). For example, nitrogen was only detected in GO-EA, indicating the functionalization of amine groups onto the GO. Moreover, the sulfonate group of GO-SA was introduced on the surface of the GO nanosheet up to 1.0% after the anchoring of the sulfonic acid groups.

The complete removal of metal salts, which often remain in graphite oxide, is another critical issue to dispersion stability of fabricated GO. These residual impurities could neutralize the charge of GO, thereby increasing aggregation and destabilization.[4] In addition to the contaminating materials originating from the chemical reagents used during synthesis, metal impurities not associated with the synthetic process were also observed. According to previous research, the main ion impurities in GO are Mn, Fe, and K.[42] As a result of the extensive purification cycles we employed, our GO and its derivatives retained metallic impurities at the level of several ppm, as measured by inductively coupled plasma optical emission spectroscopy (ICP-OES). These levels are much lower than those reported in other studies (**Table 3.3**).[42-44] Thus, we confirmed that the observed dispersion stability is mainly due to the presence of functional groups on the surface of the GO nanosheets.

Atomic force microscopy (AFM) images demonstrated that the prepared GO nanosheets were mainly composed of a monolayer of graphene nanosheets with an average thickness of 1.39 ± 0.14 nm and an area of 0.039 ± 0.010 μm^2 (**Figure 3.3**(a) and **Figure 3.4**). It should be noted that the single-layer GO nanosheet was significantly thicker than the pristine graphene due to the presence of oxygen functional groups, atomic-scale roughness arising from structural defects, and adsorbed

solvent molecules, in agreement with previous studies.[4, 9, 45-46] After chemical modification, the thicknesses of GO-EA (1.97 ± 0.19 nm), GO-EG (1.65 ± 0.16 nm), and GO-SA (1.57 ± 0.20 nm), which were averaged over 30 samples, were greater than that of GO (1.39 ± 0.14 nm) (**Figure 3.3**(b)-(d)). In addition, there were slight changes in the area of the graphene nanosheets in GO derivatives, GO-EA (0.025 ± 0.013 μm^2), GO-EG (0.053 ± 0.023 μm^2), and GO-SA (0.036 ± 0.018 μm^2), reflecting the fact that the mild nature of this synthetic approach does not alter the intrinsic properties of the graphene nanosheet.

Further investigation of the structural changes during functionalization was also conducted by Raman spectral analysis (**Figure 3.5**). GO displayed two prominent peaks at 1334 and 1604 cm^{-1}, which correspond to the symmetry A_{1g} mode of the D band and the E_{2g} mode of the sp^2 carbon atoms of the G band, respectively.[45, 47] It is well established that the D band corresponds to structural defects, an amorphous structure, or edges that break the symmetry, while the G band is associated with graphitic sp^2 carbon domains.[48] The strong intensity of the D band indicated a high density of defects and the presence of edge functional groups in GO and covalently functionalized GO. Neither the D nor the G peak positions changed after the functionalization, and the peak intensity ratio of I_D/I_G remained almost constant (1.12–1.21), implying that the structure of the carbon domain was maintained during chemical functionalization. Taken together, we argue that the dispersability of the functionalized GO derivatives was mainly influenced by the different covalent chemistries that introduced the various functional groups onto the surface of the GO nanosheets.

3.2.4.3. Quantitative Assessment for the Dispersion Stability

To obtain detailed quantitative information about the dispersion stability, we utilized a new method based on measuring sedimentation behavior under a high centrifugation force. The separation analysis of the functionalized GO materials was performed by a LUMiFuge system, which determines the space- and time-resolved extinction profiles between the bottom and the fluid level during centrifugation (**Figure 3.6**). Using centrifugation force enables the acceleration of the sedimentation of particles, leading to clarification of the dispersion. NIR transmission profiles were measured in situ every minute under centrifugation at 4000 rpm (2300 *g*) at room temperature.[39] Several reports have utilized this method to analyze the sedimentation behavior of carbon-based materials[39, 49-50]; however, only a few studies have reported the sedimentation behavior of graphene-based materials.[51-52] As mentioned earlier, while the assessment of the dispersion stability of GO has suffered as a result of the limitations of traditional approaches, which rely on the visual- or UV/vis spectroscopy-based inspection of a diluted suspension for a relatively long time period (several weeks or even years), this new investigation presents the following advantages: (1) the dispersion stability can be quantified by

calculating the instability index and sedimentation velocity; (2) a highly concentrated (9.0 mg mL^{-1}) suspension was quantified, corresponding to the highest concentration reported to date; (3) the timescale for the measurement was effectively reduced by using high-speed centrifugation; and (4) the sedimentation behavior and size distribution could be explored at the same time as the dispersion stability.

In the case of a stable suspension, the interval between each transmission profile is small due to slow sedimentation. On the other hand, fast sedimentation, which is indicative of an unstable suspension, causes a considerable change in transmission over a short time. Furthermore, each particle settles independently according to its size; thus, a broad size distribution leads to horizontal changes in the transmission.

All functionalized GO derivatives were dispersed in water (top panel in **Figure 3.7**) and EG (bottom panel in **Figure 3.7**) at a concentration of 9.0 mg mL^{-1}, which is considerably higher than the typical working concentration ranges (below 1.0 mg mL^{-1}). The initial transmission value at $t = 0$ was not related to the stability of the dispersion. However, the change in transmission over time is directly related to the dispersion stability and sedimentation velocity. The profiles of unmodified GO in water gradually shifted to the right, which suggests that sedimentation occurred under centrifugation (**Figure 3.7**(a)). In accordance with the sedimentation profile curve, the inset image clearly indicated the precipitation of unstable graphene nanosheets during measurement. In addition, it is worth noting that the vertical slope in the transmission profiles suggested that the GO dispersion was composed of uniformly sized nanosheets possessing an identical sedimentation velocity throughout the measurements. In contrast, the GO-EA suspension in water displayed slightly slanted transmission profiles (**Figure 3.7**(b)). This observation indicates that there was a size distribution in the suspension. The existing size distribution of GO-EA could originate from the reactivity of EA, which may react with the carboxylic acid group at the edges of the graphene nanosheets as well as the epoxide groups on the basal plane, eventually producing a bond bridging the two layers of graphene.[53] In accordance with the aforementioned observation, it was also interesting to note that the GO-EA showed more stacked layers with a relatively broad size distribution in the AFM images (**Figure 3.3**(b)). In **Figure 3.3**(c), the GO-EG nanosheets were relatively unstable under extensive centrifugation compared with other GO derivatives. According to recent studies, pristine GO is composed of functionalized graphene sheets decorated with strongly bound oxidative debris, which acts as a surfactant to stabilize aqueous GO suspensions.[54-55] These oxidative debris are strongly adhered to the surface of GO in acidic or neutral condition, however, it becomes separated under basic conditions due to the negative charge of the deprotonated debris. As a result, dispersion stability of GO-EG in water was slightly decreased. GO-SA represented a similar profile to the GO solution (**Figure 3.7**(d)). Although the highly charged SO^{3-} groups of GO-SA were expected to prevent aggregation and improve dispersion

stability in water, the repulsive force between the negative charges was too weak to overcome the centrifugation force and the interactions between the graphene sheets at high concentrations.

We then further investigated the suspension stability of functionalized GO derivatives in EG solvent. Initially, the GO nanosheets precipitated within 30 min in pure EG, which indicated highly unstable behavior (**Figure 3.7**(e)). In contrast to the previous report of Paredes et al. in which they observed a stable dispersion of GO in EG solvent for three weeks at a concentration 0.5 mg mL^{-1},[46] we found that the GO suspension eventually became unstable at higher concentrations in EG. This observation highlights the critical advantage of the current approach over other conventional techniques. In contrast, GO-EA and GO-EG, which were functionalized with EG-like molecules, demonstrated negligible changes in their transmission profiles during the measurement (**Figure 3.7**(f) and (g)). In particular, GO-EG showed virtually no change in its transmission profile, and sedimentation did not occur after 1000 min, even under excessive centrifugation cycles at high gravity force (2300 *g*). The closely packed lines implied that the GO-EG suspension possessed a superior solubility and stability in EG solvent. This result highlights the importance of establishing an intimate interface between the solvent (EG) and graphene derivatives (GO-EA and GO-EG) to retain excellent dispersion stability owing to their structural similarity. In addition, GO-SA showed better dispersion stability in EG than did GO. Due to the bulky functional group on the graphene surface, the aggregation of the nanosheets in EG solvent might be prevented by the steric hindrance between them (**Figure 3.7**(h)). Additional information about transmission profiles in water/EG mixture and sedimentation velocity are included in Supporting Information (**Figure 3.8** and **Table 3.4**).

3.2.4.4. Dispersion Stability in Other Non-Aqueous Solvents

According to recent literatures, GO itself could be dispersed well in several non-aqueous solvents including DMF and NMP, which exhibited a long-term stability for more than three weeks.[45] As a representative example of our functionalized GO, GO-EG was dispersed in both DMF and NMP (**Figure 3.9**). It was dispersed well in both media at a concentration of 1.0 mg mL^{-1}. However, upon centrifugation under high centrifugal force (4000 rpm), the GO-EG started to precipitate within 30 min, suggesting the relative unstable behavior of GO-EG in both solvents for a long period. Once again, this result clearly revealed the critical role of surface functional groups for achieving the optimum stability of dispersion in a desired solvent.

3.2.4.5. Rheological Behaviors of GO-Based Dispersions

During fabrication, a significant viscosity change was observed in GO and the functionalized

GO samples at high concentrations. Due to the friction force between graphene sheets, a high viscosity could affect the suspension stability. To clarify this effect, the viscosity of each GO suspension at a high concentration was measured to investigate its rheological properties (**Figure 3.10**). The viscosities of all GO and functionalized GO materials increased due to the high concentration. In particular, the viscosities of GO-SA and GO-EG in EG solvent were much higher than the base fluid of viscosities of approximately 39.18 and 35.00 mPa·s, respectively. On the other hand, the viscosity of GO-EA remained almost unchanged in all solvents. Because high viscosity could prevent the precipitation of nanosheets in suspension, a diluted GO suspension (0.50 mg mL^{-1}) was prepared in water/EG solvent, and both the viscosity and dispersion stability were measured (**Figure 3.10**). While the viscosity was similar to the base fluid at approximately 3.70 mPa·s, the dispersion stability improved compared with concentrated suspensions. Therefore, we concluded that suspensions of the functionalized GO diluted to within a conventional concentration range (below 1.0 mg mL^{-1}) would possess much better dispersion stabilities than the concentrated functionalized GO prepared herein.

3.2.4.6. Instability Index

Although the individual line of transmission does not correspond to the dispersion stability or sedimentation velocity, the difference in integral transmission versus time is directly related to the dispersion stability. We have extracted the instability index, a quantifiable parameter based on the transmission profiles as defined below (ISO/TR 13097:2013 Guidelines for the characterization of dispersion stability)

$$\text{Instability index} = \frac{\Delta T_i}{\Delta T_{max}} = \frac{\sum_{j=r_{min}}^{r_{max}} T_{i,j}^{diff}}{(\bar{T}_{End} - \bar{T}_1) \cdot (r_{max} - r_{min})}$$

where T^{diff} represents the difference between the first and subsequent transmission (T_i - T_1), r is the range of the sample analyzed, and j is the respective number of the position increment. The instability index is calculated from the normalization of the change in transmission with the highest transmission $\bar{T}_{end}$ achieved and is reported as a dimensionless number between 0 and 1. Zero represents no change in the transmission profile (very stable suspension), while an instability index of one indicates a completely separated suspension with very low stability.

The instability index was extracted from transmission measurements for all the GO dispersions (**Figure 3.11** and **Table 3.6**). In water, all the suspensions displayed a moderate dispersion stability of between 0.29 and 0.65. As EG was added to water (water/EG mixture), the instability index increased in the GO suspension, whereas the covalently functionalized GO dispersions all

exhibited lower values. Moreover, in pure EG solvent, the instability indices of GO and covalently modified GO dispersions were considerably different. The instability index of GO was 0.96, and the suspension was highly unstable, rapidly precipitating as soon as centrifugation was initiated. However, functionalized GO, especially GO-EA and GO-EG, showed significantly lower instability index values in EG solvent. Specifically, in EG solvent, the GO-EG and GO-EA suspensions were approximately 96 and 48 times more stable than GO. These findings show that the dispersion stability can be tailored by varying the functional groups on functionalized GO to achieve a desirable stability in a given solvent.

Table 3.1. Comparison of the Current Work with Other Relevant Literatures

Author	Materials	Analysis method	Concentration (mg mL^{-1})
Ruoff *et al.*[8]	Isocyanate functionalized GO	Optical characterization	1.0
	Solvent: DMF, NMP, DMSO, HMPA		
Tascón *et al.*[46]	GO	Optical characterization, UV/vis spectroscopy	0.5
	Solvent: Water, acetone, methanol, ethanol, 1-propanol, EG, DMSO, DMF, NMP, pyridine, THF, DCM, o-xylene, hexane		
Ruoff *et al.*[18]	rGO	Optical characterization	0.3
	Solvent: DMF, ethanol, acetone, THF, DMSO, NMP, acetonitrile, DCB, diethylether, toluene		
Chabal *et al.*[38]	Amine treated GO	Optical characterization	0.5
	Solvent: Chloroform, IPA		
Feng *et al.*[48]	Solvothermal rGO	Optical characterization	1.0
	Solvent: DMSO, EA, acetonitrile, ethanol, THF, DMF, chloroform, acetone		
Zhang *et al.*[2]	Polymer functionalized rGO	Optical characterization, Zeta potential	3.6
	Solvent: Water, methanol, ethanol, DMF, DMSO		
Wang *et al.*[19]	Octoxyphenyl functionalized GO	Optical characterization	1.8
	Solvent: DMF		
Khatri *et al.*[20]	Alkylated GO	Optical characterization	0.1
	Solvent: DMF, THF, ethanol, toluene, hexane, hexadecane		
Barteau *et al.*[17]	Alkylated GO	Optical characterization	1.0
	Solvent: DMSO, DMF, chloroform, ethanol, methanol, water, toluene, heptane, decane		
Our Work	Small molecules functionalized GO	Optical characterization,	9.0
	Solvent: Water, EG		

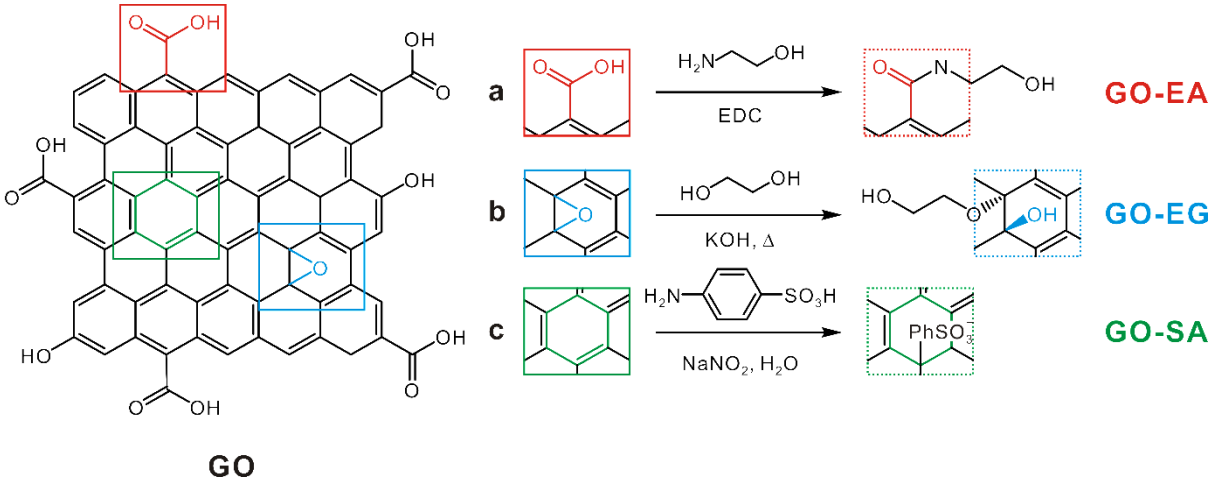

Figure 3.1. Schematic representation of the surface functionalization of GO nanosheets with (a) ethanolamine (EA), (b) ethylene glycol (EG), and (c) sulfanilic acid (SA) molecules to afford the respective functionalized GO-EA, GO-EG, and GO-SA nanosheets.

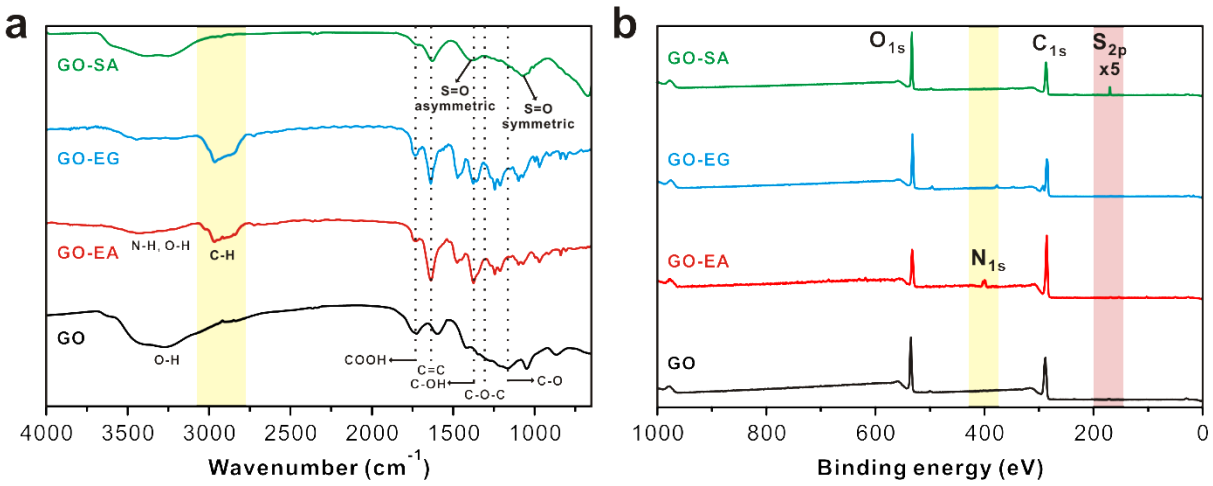

Figure 3.2. (a) FT-IR spectra and (b) XPS survey spectra of GO, GO-EA, GO-EG, and GO-SA.

Table 3.2. Relative Atomic Ratio (%) Based on XPS and Elemental Analysis Measurements.

	XPS				Elemental Analysis			
	C1s	**O1s**	**N1s**	**S2p**	**C**	**O**	**N**	**S**
GO	71.1	27.4	ND[a]	0.7[b]	48.5	45.7	ND	1.0[b]
GO-EA	73.4	18.6	6.7	ND	52.6	29.6	9.8	ND
GO-EG	69.6	26.1	ND	ND	47.7	42.0	ND	ND
GO-SA	66.7	30.9	0.6	1.0	48.2	44.5	ND	0.94

[a]Values below the detection limit of the XPS and elemental analysis are represented as not detectable (ND), [b]a trace amount of sulfur originated from the sulfuric acid in the synthesis of GO.

Table 3.3. Elemental Concentrations of Representative Metals Present in GO and Functionalized GO as Determined by ICP-OES (ppm by mass).

	Elemental Concentration (ppm)		
Compound	**Mn**	**K**	**Fe**
GO	0.020	0.88	0.029
GO-EA	0.024	0.27	0.060
GO-EG	0.078	6.8	0.83
GO-SA	0.049	1.1	0.029

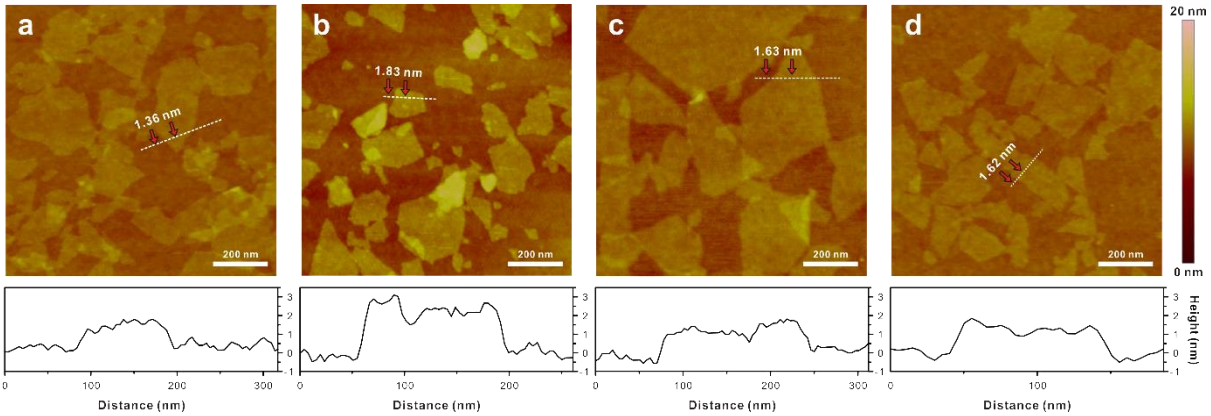

Figure 3.3. Representative AFM images of (a) GO, (b) GO-EA, (c) GO-EG, and (d) GO-SA with the corresponding line scan profiles. All GO samples were deposited on a silicon wafer from an aqueous dispersion.

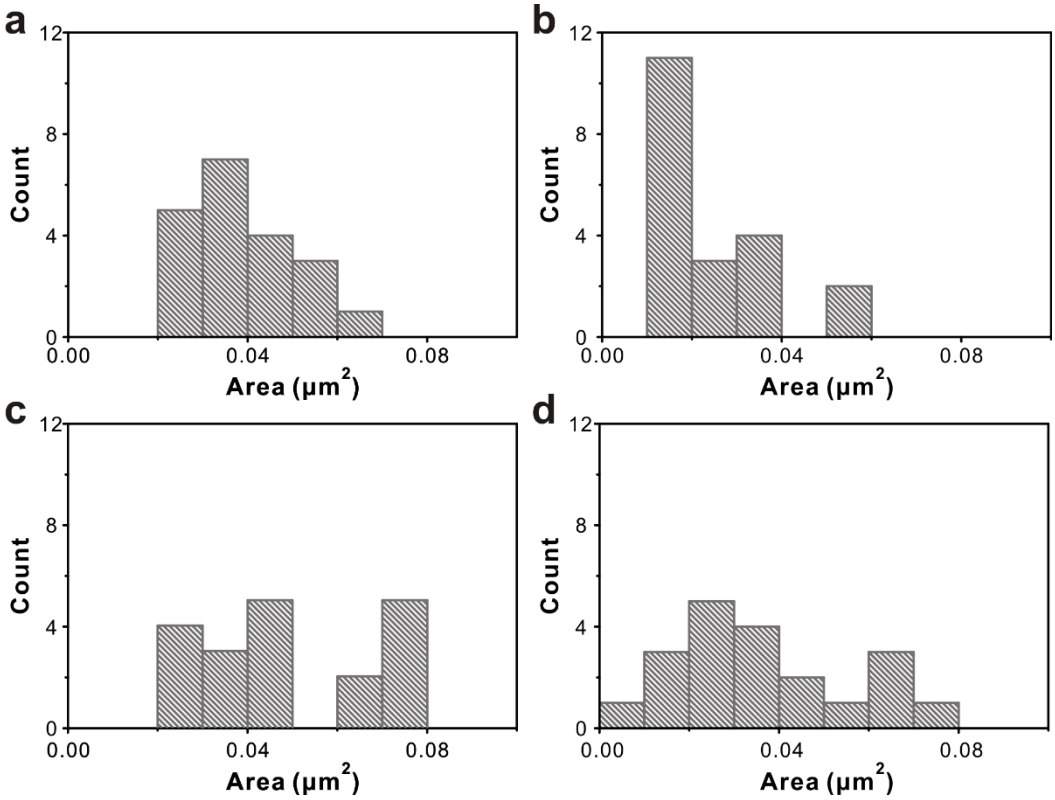

Figure 3.4. Area distribution of (a) GO, (b) GO-EA, (c) GO-EG, and (d) GO-SA measured by AFM. The area was calculated by a SemAfore 5.21 program with 20 random nanosheets.

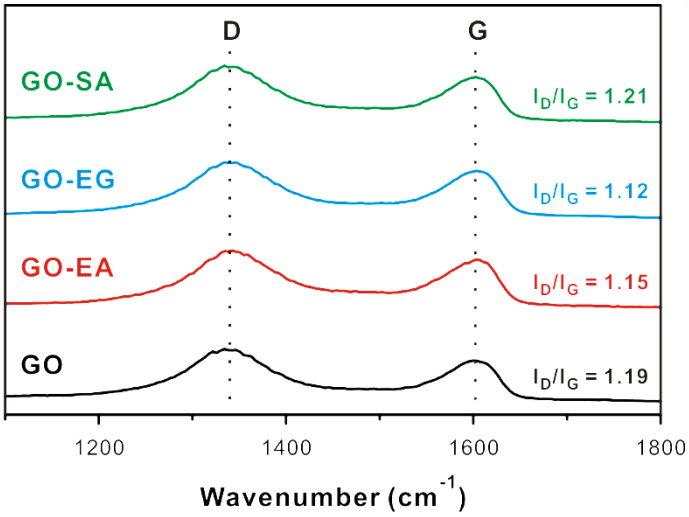

Figure 3.5. Raman spectra of GO and functionalized GO. Argon ion laser with a wavelength of 532 nm was used as an excitation source. D and G band is appeared at 1334 and 1604 cm^{-1}, respectively.

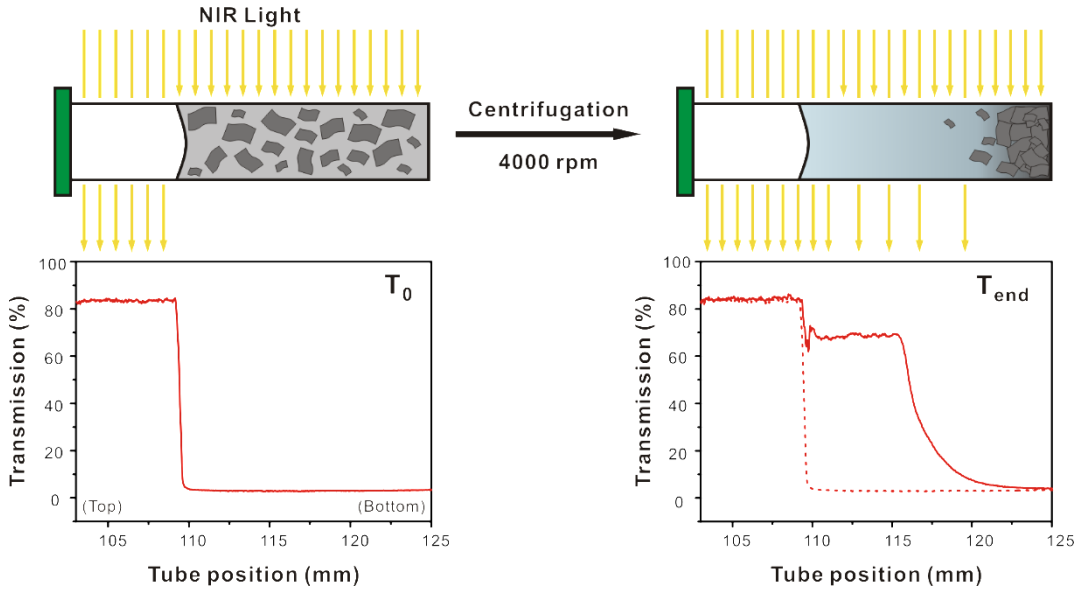

Figure 3.6. Schematic representation and the corresponding transmission profile for the analysis of the dispersion stability of covalent functionalized GO suspensions using transmission profiles under centrifugation system. The transmission of near infrared (NIR) irradiation was measured over the entire sample tube to allow spatial and temporal changes of GO dispersion during centrifugation.

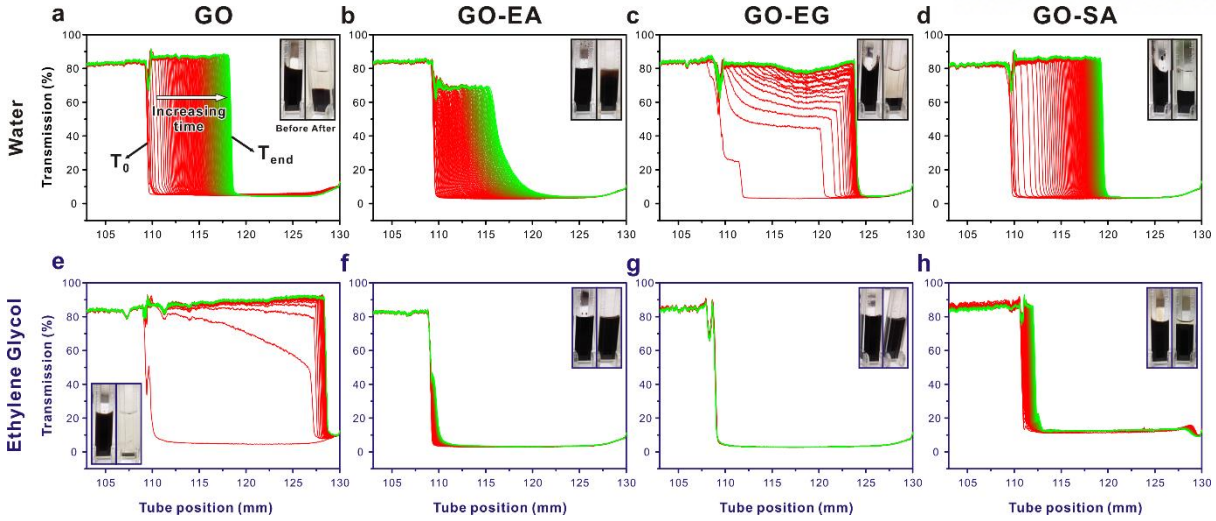

Figure 3.7. Transmission profiles of functionalized GO suspensions in different solvents: water (top panel) and ethylene glycol (bottom panel). (a, e) GO, (b, f) GO-EA, (c, g) GO-EG, and (d, h) GO-SA. The red line represents the first scan and the green line the last scan (t = 1000 min), with a regular scan reported every 10 min at a concentration of 9.0 mg mL^{-1} using a LUMiFuge instrument under 4000 rpm (2300 g) at room temperature. The inset images display the respective suspension (left) before and (right) after centrifugation.

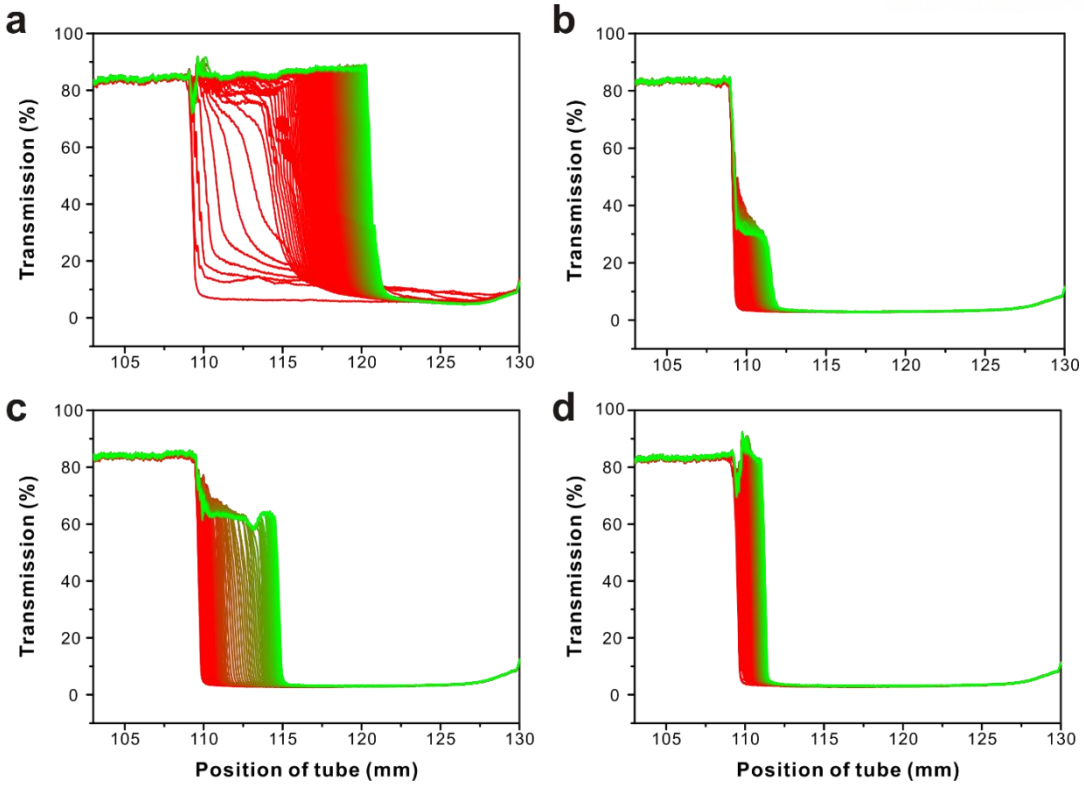

Figure 3.8. Transmission profiles of (a) GO, (b) GO-EA, (c) GO-EG and (d) GO-SA in Water/EG mixture (50 vol %). Red line represents the first scan and the green is the last scan (t = 1000 min) with a regular scan reported in every 10 min at a concentration of 9.0 mg mL^{-1} using LUMiFuge under 4000 rpm (2300 g) at room temperature.

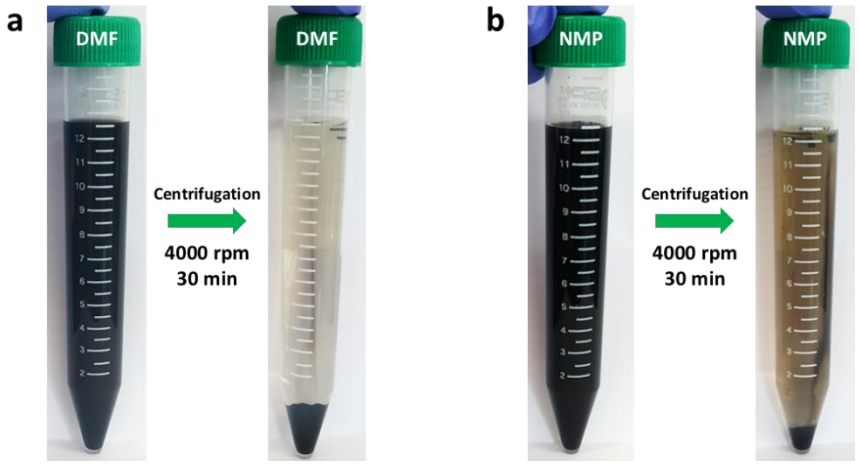

Figure 3.9. GO-EG suspension in (a) DMF and (b) NMP solvent at a concentration of 1.0 mg mL^{-1} before and after centrifugation.

Table 3.4. Sedimentation Velocity of GO-Based Materials in Different Solvents. Position of Interface against Time Allows Calculating the Sedimentation Velocity in Transmission Profiles.

Compound	Sedimentation velocity (μm/min)		
	Water	Water/EG	EG
GO	10.36	43.71	1658
GO-EA	6.807	2.056	0.092
GO-EG	39.50	4.117	~0
GO-SA	12.86	1.733	1.318

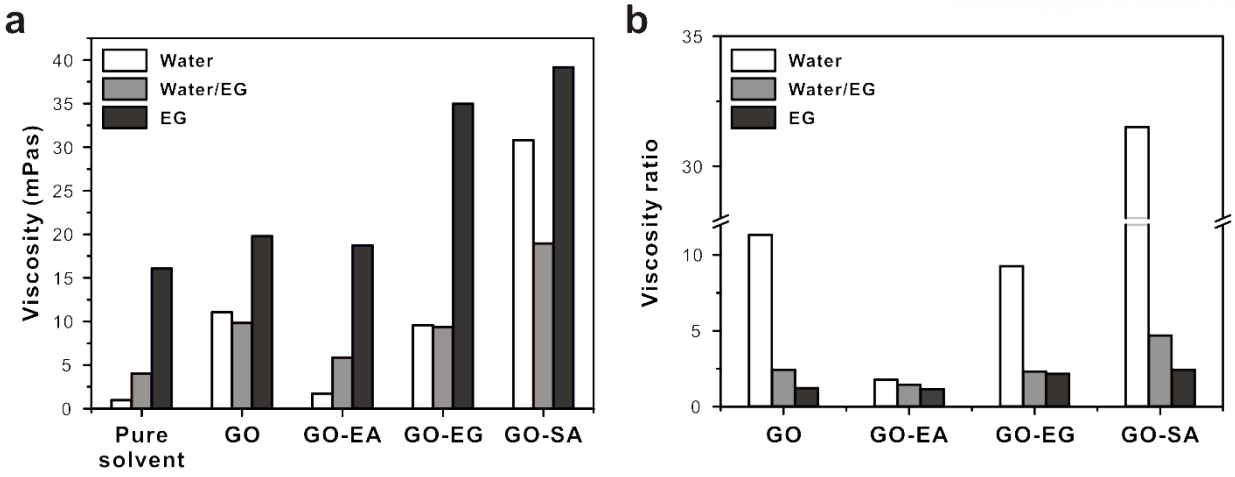

Figure 3.10. (a) Viscosities of GO and functionalized GO suspensions in water, EG/water mixture and EG solvents, and (b) relative viscosity ratio of GO-derivatives with reference to that of pure solvent. Rheological properties were measured by Haake MARS III - ORM Package at room temperature.

Table 3.5. Viscosity Values of GO and Functionalized GOs in Different Solvents.

Compound	Viscosity (mPas)		
	Water	Water/EG	EG
Pure solvent	0.98	4.03	16.10
GO	11.08	9.84	19.80
GO-EA	1.73	5.87	18.75
GO-EG	9.60	9.37	34.99
GO-SA	30.82	18.96	39.18

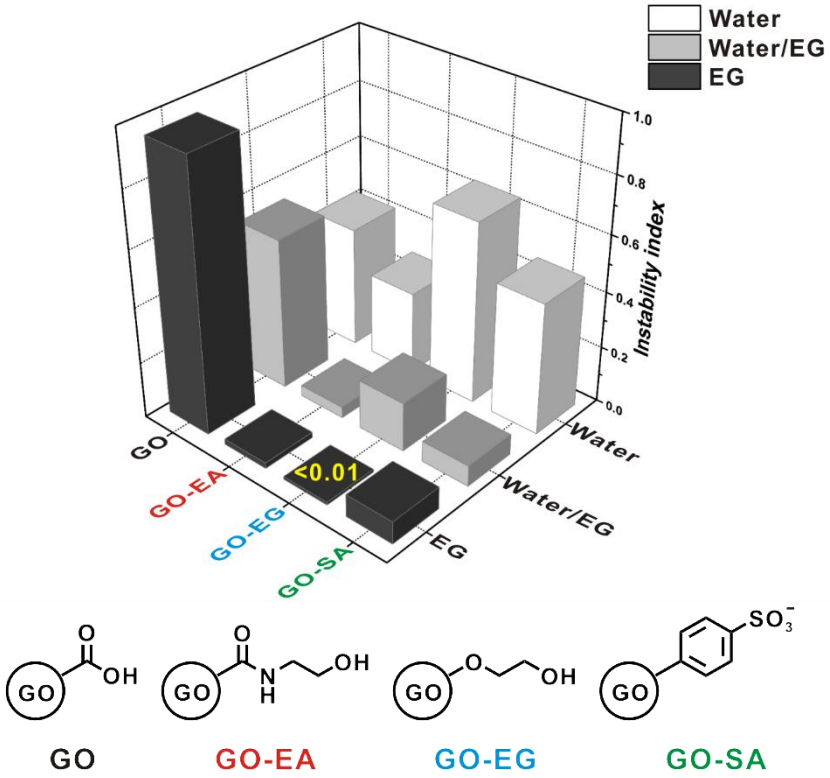

Figure 3.11. A 3D matrix of the instability index of functionalized GO in different solvents: water, water/EG (1:1), and EG with a corresponding schematic representation of the covalently functionalized GO samples. The instability index was calculated on the basis of the sedimentation transmission curves shown in Figure 3.7 and Figure 3.8.

Table 3.6. Instability Indices Calculated from the Transmission Profile.

Instability index	Water	Water/EG	EG
GO	0.430	0.539	0.958
GO-EA	0.293	0.039	0.02
GO-EG	0.648	0.175	<0.01
GO-SA	0.469	0.074	0.08

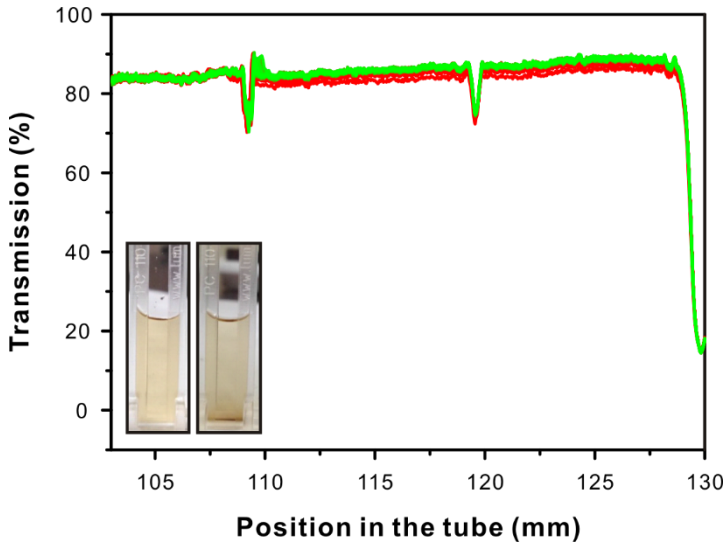

Figure 3.12. Transmission profiles of GO in water/EG mixture with diluted concentration (0.50 mg mL^{-1}). Measurement condition was identical to previous description in Figure 3.8.

3.2.5. Conclusion

In summary, we have developed a facile approach for the surface modification of GO nanosheets to enhance the dispersion stability in the organic solvent EG. FT-IR, XPS, AFM, elemental analysis, and Raman measurements confirm the successful covalent functionalization of GO-EA, GO-EG, and GO-SA without significant morphological changes of the nanosheets. As a result, the structural similarities resulted in a highly improved affinity between the functionalized GO materials and EG solvent; thus, excellent dispersion stability was maintained at high concentrations up to 9.0 mg mL^{-1}. The other meaningful aspect of this research was that the dispersion stability of GO and its derivatives could be quantified by the instability index and sedimentation velocity, which have been largely unexplored to date. Although current conclusion is applicable in GO derivative with relatively small lateral dimension, it would afford versatile opportunity to achieve a highly stable dispersion in a desired solvent, which increases the viability of the large-scale technological application of GO in organic solvents. The stable graphene based suspension in EG will provide promising ways for fabrication to develop heat transfer systems such as coolants or antifreeze applications.

3.2.6. References

(1) Chandrawati, R.; Caruso, F., Biomimetic Liposome- and Polymersome-Based Multicompartmentalized Assemblies. *Langmuir* **2012,** *28*, 13798-13807.

(2) Qi, X.; Pu, K.-Y.; Zhou, X.; Li, H.; Liu, B.; Boey, F.; Huang, W.; Zhang, H., Conjugated-Polyelectrolyte-Functionalized Reduced Graphene Oxide with Excellent Solubility and Stability in Polar Solvents. *Small* **2010,** *6*, 663-669.

(3) Geim, A. K.; Novoselov, K. S., The Rise of Graphene. *Nat. Mater.* **2007,** *6*, 183-191.

(4) Li, D.; Muller, M. B.; Gilje, S.; Kaner, R. B.; Wallace, G. G., Processable Aqueous Dispersions of Graphene Nanosheets. *Nat. Nanotechnol.* **2008,** *3*, 101-105.

(5) Sun, Y.; Wu, Q.; Shi, G., Graphene Based New Energy Materials. *Energy Environ. Sci.* **2011,** *4*, 1113-1132.

(6) Nair, R. R.; Blake, P.; Grigorenko, A. N.; Novoselov, K. S.; Booth, T. J.; Stauber, T.; Peres, N. M. R.; Geim, A. K., Fine Structure Constant Defines Visual Transparency of Graphene. *Science* **2008,** *320*, 1308-1308.

(7) Stankovich, S.; Dikin, D. A.; Piner, R. D.; Kohlhaas, K. A.; Kleinhammes, A.; Jia, Y.; Wu, Y.; Nguyen, S. T.; Ruoff, R. S., Synthesis of Graphene-Based Nanosheets Via Chemical Reduction of Exfoliated Graphite Oxide. *Carbon* **2007,** *45*, 1558-1565.

(8) Stankovich, S.; Piner, R. D.; Nguyen, S. T.; Ruoff, R. S., Synthesis and Exfoliation of Isocyanate-Treated Graphene Oxide Nanoplatelets. *Carbon* **2006,** *44*, 3342-3347.

(9) Stankovich, S.; Dikin, D. A.; Dommett, G. H. B.; Kohlhaas, K. M.; Zimney, E. J.; Stach, E. A.; Piner, R. D.; Nguyen, S. T.; Ruoff, R. S., Graphene-Based Composite Materials. *Nature* **2006,** *442*, 282-286.

(10) Zhang, K.; Mao, L.; Zhang, L. L.; On Chan, H. S.; Zhao, X. S.; Wu, J., Surfactant-Intercalated, Chemically Reduced Graphene Oxide for High Performance Supercapacitor Electrodes. *J. Mater. Chem.* **2011,** *21*, 7302-7307.

(11) Lotya, M.; Hernandez, Y.; King, P. J.; Smith, R. J.; Nicolosi, V.; Karlsson, L. S.; Blighe, F. M.; De, S.; Wang, Z.; McGovern, I. T.; Duesberg, G. S.; Coleman, J. N., Liquid Phase Production of Graphene by Exfoliation of Graphite in Surfactant/Water Solutions. *J. Am. Chem. Soc.* **2009,** *131*, 3611-3620.

(12) Stankovich, S.; Piner, R. D.; Chen, X.; Wu, N.; Nguyen, S. T.; Ruoff, R. S., Stable Aqueous Dispersions of Graphitic Nanoplatelets Via the Reduction of Exfoliated Graphite Oxide in the Presence of Poly(Sodium 4-Styrenesulfonate). *J. Mater. Chem.* **2006,** *16*, 155-158.

(13) Yangqiao, L.; Lian, G.; Jing, S.; Yan, W.; Jing, Z., Stable Nafion-Functionalized Graphene Dispersions for Transparent Conducting Films. *Nanotechnology* **2009,** *20*, 465605.

(14) Xu, Y.; Bai, H.; Lu, G.; Li, C.; Shi, G., Flexible Graphene Films Via the Filtration of Water-Soluble Noncovalent Functionalized Graphene Sheets. *J. Am. Chem. Soc.* **2008,** *130*, 5856-5857.

(15) Cai, X.; Tan, S.; Lin, M.; Xie, A.; Mai, W.; Zhang, X.; Lin, Z.; Wu, T.; Liu, Y., Synergistic Antibacterial Brilliant Blue/Reduced Graphene Oxide/Quaternary Phosphonium Salt Composite with Excellent Water Solubility and Specific Targeting Capability. *Langmuir* **2011,** *27*, 7828-7835.

(16) Zhuang, X.-D.; Chen, Y.; Liu, G.; Li, P.-P.; Zhu, C.-X.; Kang, E.-T.; Noeh, K.-G.; Zhang, B.; Zhu, J.-H.; Li, Y.-X., Conjugated-Polymer-Functionalized Graphene Oxide: Synthesis and Nonvolatile Rewritable Memory Effect. *Adv. Mater.* **2010,** *22*, 1731-1735.

(17) Tessonnier, J.-P.; Barteau, M. A., Dispersion of Alkyl-Chain-Functionalized Reduced Graphene Oxide Sheets in Nonpolar Solvents. *Langmuir* **2012,** *28*, 6691-6697.

(18) Park, S.; An, J.; Jung, I.; Piner, R. D.; An, S. J.; Li, X.; Velamakanni, A.; Ruoff, R. S., Colloidal Suspensions of Highly Reduced Graphene Oxide in a Wide Variety of Organic Solvents. *Nano Lett.* **2009,** *9*, 1593-1597.

(19) Zhong, Z.; Dai, Y.; Ma, D.; Wang, Z. Y., Facile Synthesis of Organo-Soluble Surface-Grafted All-Single-Layer Graphene Oxide as Hole-Injecting Buffer Material in Organic Light-Emitting Diodes. *J. Mater. Chem.* **2011,** *21*, 6040-6045.

(20) Choudhary, S.; Mungse, H. P.; Khatri, O. P., Dispersion of Alkylated Graphene in Organic Solvents and Its Potential for Lubrication Applications. *J. Mater. Chem.* **2012,** *22*, 21032-21039.

(21) Kole, M.; Dey, T. K., Investigation of Thermal Conductivity, Viscosity, and Electrical Conductivity of Graphene Based Nanofluids. *J. Appl. Phys.* **2013,** *113*, 084307.

(22) Eastman, J. A.; Choi, S. U. S.; Li, S.; Yu, W.; Thompson, L. J., Anomalously Increased Effective Thermal Conductivities of Ethylene Glycol-Based Nanofluids Containing Copper Nanoparticles. *Appl. Phys. Lett.* **2001,** *78*, 718-720.

(23) Jha, N.; Ramaprabhu, S., Thermal Conductivity Studies of Metal Dispersed Multiwalled Carbon Nanotubes in Water and Ethylene Glycol Based Nanofluids. *J. Appl. Phys.* **2009,** *106*, 084317.

(24) Garg, J.; Poudel, B.; Chiesa, M.; Gordon, J. B.; Ma, J. J.; Wang, J. B.; Ren, Z. F.; Kang, Y. T.; Ohtani, H.; Nanda, J.; McKinley, G. H.; Chen, G., Enhanced Thermal Conductivity and Viscosity of Copper Nanoparticles in Ethylene Glycol Nanofluid. *J. Appl. Phys.* **2008,** *103*, 074301.

(25) Hadadian, M.; Goharshadi, E. K.; Youssefi, A., Electrical Conductivity, Thermal Conductivity, and Rheological Properties of Graphene Oxide-Based Nanofluids. *J. Nanopart. Res.* **2014,** *16*, 1-17.

(26) Yu, W.; Xie, H.; Wang, X.; Wang, X., Significant Thermal Conductivity Enhancement for Nanofluids Containing Graphene Nanosheets. *Phys. Lett. A* **2011,** *375*, 1323-1328.

(27) Sen Gupta, S.; Manoj Siva, V.; Krishnan, S.; Sreeprasad, T. S.; Singh, P. K.; Pradeep, T.; Das, S. K., Thermal Conductivity Enhancement of Nanofluids Containing Graphene Nanosheets. *J. Appl. Phys.* **2011,** *110*, 084302.

(28) Si, Y.; Samulski, E. T., Synthesis of Water Soluble Graphene. *Nano Lett.* **2008,** *8*, 1679-1682.

(29) Ji, J.; Zhang, G.; Chen, H.; Wang, S.; Zhang, G.; Zhang, F.; Fan, X., Sulfonated Graphene as Water-Tolerant Solid Acid Catalyst. *Chem. Sci.* **2011,** *2*, 484-487.

(30) Beckert, F.; Rostas, A. M.; Thomann, R.; Weber, S.; Schleicher, E.; Friedrich, C.; Mülhaupt, R., Self-Initiated Free Radical Grafting of Styrene Homo- and Copolymers onto Functionalized Graphene. *Macromolecules* **2013,** *46*, 5488-5496.

(31) Hummers, W. S.; Offeman, R. E., Preparation of Graphitic Oxide. *J. Am. Chem. Soc.* **1958,** *80*, 1339-1339.

(32) Lee, D. W.; Hong, T.-K.; Kang, D.; Lee, J.; Heo, M.; Kim, J. Y.; Kim, B.-S.; Shin, H. S., Highly Controllable Transparent and Conducting Thin Films Using Layer-by-Layer Assembly of Oppositely Charged Reduced Graphene Oxides. *J. Mater. Chem.* **2011,** *21*, 3438-3442.

(33) Park, M.; Lee, T.; Kim, B.-S., Covalent Functionalization Based Heteroatom Doped Graphene Nanosheet as a Metal-Free Electrocatalyst for Oxygen Reduction Reaction. *Nanoscale* **2013,** *5*, 12255-12260.

(34) Jeon, E. K.; Seo, E.; Lee, E.; Lee, W.; Um, M.-K.; Kim, B.-S., Mussel-Inspired Green Synthesis of Silver Nanoparticles on Graphene Oxide Nanosheets for Enhanced Catalytic Applications. *Chem. Commun.* **2013,** *49*, 3392-3394.

(35) Hwang, H.; Joo, P.; Kang, M. S.; Ahn, G.; Han, J. T.; Kim, B.-S.; Cho, J. H., Highly Tunable Charge Transport in Layer-by-Layer Assembled Graphene Transistors. *ACS Nano* **2012,** *6*, 2432-2440.

(36) Englert, J. M.; Dotzer, C.; Yang, G.; Schmid, M.; Papp, C.; Gottfried, J. M.; Steinrück, H.-P.; Spiecker, E.; Hauke, F.; Hirsch, A., Covalent Bulk Functionalization of Graphene. *Nat. Chem.* **2011,** *3*, 279-286.

(37) Rice, J. E.; He, Z. M., Preparation of 4- and 10-Fluorobenzo[j]Fluoranthene Via Cyclodehydration of Acetals and Cyclopropylcarboxaldehydes. *J. Org. Chem.* **1990,** *55*, 5490-5494.

(38) Acik, M.; Lee, G.; Mattevi, C.; Pirkle, A.; Wallace, R. M.; Chhowalla, M.; Cho, K.; Chabal, Y., The Role of Oxygen During Thermal Reduction of Graphene Oxide Studied by Infrared Absorption Spectroscopy. *J. Phys. Chem. C* **2011,** *115*, 19761-19781.

(39) Krause, B.; Petzold, G.; Pegel, S.; Pötschke, P., Correlation of Carbon Nanotube Dispersability in Aqueous Surfactant Solutions and Polymers. *Carbon* **2009,** *47*, 602-612.

(40) Bagri, A.; Mattevi, C.; Acik, M.; Chabal, Y. J.; Chhowalla, M.; Shenoy, V. B., Structural Evolution During the Reduction of Chemically Derived Graphene Oxide. *Nat. Chem.* **2010,** *2*, 581-587.

(41) Zhang, F.; Jiang, H.; Li, X.; Wu, X.; Li, H., Amine-Functionalized GO as an Active and Reusable Acid–Base Bifunctional Catalyst for One-Pot Cascade Reactions. *ACS Catal.* **2014,** *4*, 394-401.

(42) Wong, C. H. A.; Sofer, Z.; Kubešová, M.; Kučera, J.; Matějková, S.; Pumera, M., Synthetic Routes Contaminate Graphene Materials with a Whole Spectrum of Unanticipated Metallic Elements. *Proc. Natl. Acad. Sci. USA* **2014,** *111*, 13774-13779.

(43) Wang, L.; Ambrosi, A.; Pumera, M., "Metal-Free" Catalytic Oxygen Reduction Reaction on Heteroatom-Doped Graphene Is Caused by Trace Metal Impurities. *Angew. Chem. Int. Ed.* **2013,** *52*,

13818-13821.

(44) Su, C.; Acik, M.; Takai, K.; Lu, J.; Hao, S.-j.; Zheng, Y.; Wu, P.; Bao, Q.; Enoki, T.; Chabal, Y. J.; Ping Loh, K., Probing the Catalytic Activity of Porous Graphene Oxide and the Origin of This Behaviour. *Nat. Commun.* **2012,** *3*, 1298.

(45) Gómez-Navarro, C.; Weitz, R. T.; Bittner, A. M.; Scolari, M.; Mews, A.; Burghard, M.; Kern, K., Electronic Transport Properties of Individual Chemically Reduced Graphene Oxide Sheets. *Nano Lett.* **2007,** *7*, 3499-3503.

(46) Paredes, J. I.; Villar-Rodil, S.; Martínez-Alonso, A.; Tascón, J. M. D., Graphene Oxide Dispersions in Organic Solvents. *Langmuir* **2008,** *24*, 10560-10564.

(47) Zhang, J.; Yang, H.; Shen, G.; Cheng, P.; Zhang, J.; Guo, S., Reduction of Graphene Oxide Vial-Ascorbic Acid. *Chem. Commun.* **2010,** *46*, 1112-1114.

(48) Chen, C.; Cai, W.; Long, M.; Zhou, B.; Wu, Y.; Wu, D.; Feng, Y., Synthesis of Visible-Light Responsive Graphene Oxide/TiO_2 Composites with P/N Heterojunction. *ACS Nano* **2010,** *4*, 6425-6432.

(49) Pegel, S.; Pötschke, P.; Petzold, G.; Alig, I.; Dudkin, S. M.; Lellinger, D., Dispersion, Agglomeration, and Network Formation of Multiwalled Carbon Nanotubes in Polycarbonate Melts. *Polymer* **2008,** *49*, 974-984.

(50) Azoubel, S.; Magdassi, S., The Formation of Carbon Nanotube Dispersions by High Pressure Homogenization and Their Rapid Characterization by Analytical Centrifuge. *Carbon* **2010,** *48*, 3346-3352.

(51) Edenharter, A.; Feicht, P.; Diar-Bakerly, B.; Beyer, G.; Breu, J., Superior Flame Retardant by Combining High Aspect Ratio Layered Double Hydroxide and Graphene Oxide. *Polymer* **2016,** *91*, 41-49.

(52) Han, J. T.; Jang, J. I.; Kim, H.; Hwang, J. Y.; Yoo, H. K.; Woo, J. S.; Choi, S.; Kim, H. Y.; Jeong, H. J.; Jeong, S. Y.; Baeg, K.-J.; Cho, K.; Lee, G.-W., Extremely Efficient Liquid Exfoliation and Dispersion of Layered Materials by Unusual Acoustic Cavitation. *Sci. Rep.* **2014,** *4*, 5133.

(53) Lee, J. U.; Lee, W.; Yi, J. W.; Yoon, S. S.; Lee, S. B.; Jung, B. M.; Kim, B. S.; Byun, J. H., Preparation of Highly Stacked Graphene Papers Via Site-Selective Functionalization of Graphene Oxide. *J. Mater. Chem. A* **2013,** *1*, 12893-12899.

(54) Rourke, J. P.; Pandey, P. A.; Moore, J. J.; Bates, M.; Kinloch, I. A.; Young, R. J.; Wilson, N. R., The Real Graphene Oxide Revealed: Stripping the Oxidative Debris from the Graphene-Like Sheets. *Angew. Chem. Int. Ed.* **2011,** *50*, 3173-3177.

(55) Thomas, H. R.; Day, S. P.; Woodruff, W. E.; Vallés, C.; Young, R. J.; Kinloch, I. A.; Morley, G. W.; Hanna, J. V.; Wilson, N. R.; Rourke, J. P., Deoxygenation of Graphene Oxide: Reduction or Cleaning? *Chem. Mater.* **2013,** *25*, 3580-3588.

3.3. Chemical Functionalization of Graphene Oxide with Long Aliphatic Chain for Lubricant Applications

3.3.1. Introduction

Reduction of friction in mechanical elements is one of the most important factors for improving energy efficiency of machine and enhancing the durability of the components. Especially, in the automobile industry, the lubricant property is the most critical issue to improve energy efficiency and reduce emission of greenhouse gasses.

Generally, layered materials such as molybdenum disulphide (MoS_2) have been utilized as commercial lubricants.[1] The unique anisotropic structure of layered materials includes strong covalent interlayer interaction, and weak can der Waals interlayer interactions, which makes them effective lubricants.[2-4] However, conventional metal-based lubricant additives have severe limitations. For example, they adsorbed on to the metal surface and accelerated corrosion of the machines. Moreover, high cost and limited resources of metal-based components make it hard to utilize as the practical applications. To overcome this limitation, we developed graphene-based lubricant additives to improve friction efficiency and utilized with the commercial engine oil. Due to the extraordinary properties of graphene, several researches have already reported for graphene-based additives to improve friction efficiency. There are three representative methods to utilize as the lubricant additives including chemically modified graphene,[1, 5-6] morphological modification of graphene,[7] and metal/graphene composites.[8] Generally, almost papers suggested that graphene-based protective layers are formed on to the steel coverage, and it decreases friction coefficient and improve wear properties. However, characterization of graphene derivatives and specific reasons for improved performance are lack to emphasize novelty of graphene-based additives. For these reasons, we tried to design new structure of GO derivatives to improve dispersion stability in oil with scientific characterizations. We anticipated graphene-based additives could not only enhance friction property of lubricant due to the layered structure of graphite, but also prevent corrosion of metal by outstanding mechanical stability of graphene.

For the effective lubricant, dispersion stability of additive in oil is crucial aspect. However, interaction of hydrophilic GO is challenging in hydrophobic commercial lubricant oils due to different cohesive energy. To improve cohesive interaction between graphene nanosheets and oil solvent, herein, we developed the synthetic method to chemically modify GO with the long aliphatic chain molecule, oleylamine (OA), with covalent functionalization (**Figure 3.13**).[9-10] Furthermore, we demonstrated how friction efficient could be tailored by varying the functional groups based on diverse GO-derivatives.

3.3.2. Experimental

3.3.2.1. Synthesis of GO-OA and TRGO-OA

At first, GO powder was dispersed in 50 mL of OA solvent (concentration 0.50 mg mL^{-1}). For the chemical functionalization of the epoxide groups of GO with OA, suspension was reacted at 100 °C for 24 h. After the reaction, the solution was centrifuged with 6000 rpm for 10 min and washed with ethanol several times. GO-OA powder was collected and dried in the oven at 60 °C for overnight. As following, thermal reduction was conducted to synthesize TRGO-OA at 200 °C under Ar atmosphere for 2 h.

3.3.2.2. Synthesis of GO-OA_CDI and TRGO-OA_CDI

Pristine GO powder was prepared in DMF solvent with 0.50 mg mL^{-1} concentration. For the chemical functionalization of the carboxylic acid groups of GO with OA, 1.0 g of carbonyldiimidazole (CDI) was added in GO suspension and mixture was reacted at 60 °C for 12 h. The product (GO-OA_CDI) was collected by centrifugation with 6000 rpm for 10 min and washed with ethanol several times. Drying and thermal reduction process to synthesize TRGO-OA_CDI was identical with TRGO-OA.

3.3.2.3. Characterization

The ζ-potential of the GO suspensions was measured using a ζ -potential analyzer (Mal-vern, Zetasizer nano-zs). FT-IR spectroscopy was used to determine the chemical structure and bonding of the GO-derivatives, and X-ray photoelectron spectroscopy (XPS, Thermo Fisher, K-alpha) was used to detect the elemental composition and the chemical bonding of the functionalized GO-derivatives.

3.3.3. Results and Discussion

The GO nanosheet was prepared by the oxidation of graphite with a modified Hummer's method, mentioned in Chapter 1.2. The oxygen-containing functional groups on the graphene surface, including hydroxyl, carboxylic acid, and epoxy groups, rendered the GO negatively charged in aqueous solution (ζ-potential of −40 mV). As the initial stage of our work, OA molecule, which has 18 carbon chains, are covalently incorporated on GO nanosheets to increase hydrophobicity of GO. We postulate that long aliphatic chain in OA molecule would improve dispersion stability in oil due to the similarity of their chemical structures. There are two different synthetic method to combine GO and OA by 1,1'-Carbonyldiimidazole (CDI) chemistry and thermal addition (**Figure 3.13**).

First, CDI-mediated surface functionalization of GO was achieved through the reaction between carboxylic acids and the amine groups of CDI, and the product is denoted as GO-OA_CDI (OA-incorporated GO with CDI chemistry). Since the carboxylic acid groups are mostly attached at the edge site, OA was predominantly located at the edge of the graphene nanosheets. Furthermore, OA-functionalized GO (GO-OA) was synthesized through the reaction between epoxy groups and amine groups of OA under heating condition. While OA molecules were incorporated at the edge site with GO-OA_CDI, OA functionalization of GO-OA was mostly occurred on the basal plane of GO because epoxy groups are mostly decorated on the surface of the graphene nanosheets. As shown in **Figure 3.14**, chemically modified GO (GO-OA_CDI and GO-OA) represents good dispersion stability in both OA solvent and lubricant oil. Since remaining oxygen functional groups could increase friction of lubricant oil, additional thermal treatment was conducted by thermal annealing process and they were denoted as TRGO-OA_CDI and TRGO-OA, respectively. By fabricating four different GO-derivatives, we demonstrate how the dispersion stability and friction properties can be tailored by varying the chemical structure of GO. In **Figure 3.15**(a), GO was totally not dispersed, and all particles were settled down in oil solvent due to the hydrophilicity of GO. In contrast, four GO-derivatives (GO-OA_CDI, GO-OA, TRGO-OA_CDI, and TRGO-OA) were dispersed well in the oil and good dispersion stability for several days, which implied that chemical modification can be tailored intrinsic properties of GO.

The successful functionalization was confirmed by FT-IR and X-ray photoelectron spectroscopy (XPS) measurements (**Figure 3.16** and **Table 3.7**). The FT-IR spectra represented that the pristine GO revealed three characteristic peaks around 3300, 1725, and 1420 cm^{-1} corresponding to the hydroxyl, carboxylic, and epoxy groups, respectively.[11-12] The functionalized GO-derivatives exhibited distinctive peaks compared with pristine GO. Two additional peaks were appeared at 2966 and 2865 cm^{-1}, indicating asymmetric and symmetric stretching modes of C-H bonding from OA molecule.[13] The intensity of oxygen functional groups was significantly reduced after the functionalization with OA, which indicated that long aliphatic chain was well introduced after chemical modification. In order to further identify the atomic composition of GO-derivatives, XPS

measurement was investigated (**Table 3.7**). Nitrogen was detected in GO-derivatives, not detectable in pristine GO, which is strong evident for covalent functionalization between carboxylic groups of GO and amine groups of OA. Moreover, the C/O ratio was greatly increased with GO-derivatives since long alkyl chain was incorporated on the surface of graphene. Based on these results, we confirmed that OA molecule was successfully introduced in the GO-OA_CDI and GO-OA. Moreover, chemical bonding was well preserved during thermal treatment to synthesize TRGO-OA_CDI, and TRGO-OA.

As following, we investigated thermogravimetric analysis (TGA) to trace the thermal properties of GO and GO-derivatives according to the temperature (**Figure 3.17**). In case of pristine GO, weight ratio was rapidly decreased around 100 °C due to evaporation of water molecules.[14-15] In contrast, there is comparatively small amount of weight loss by GO-derivatives in this temperature region, indicating that water molecules in functionalized GO-derivatives were mostly removed during chemical modification. Significant weight loss (~50%) was appeared with GO near 200 °C, because almost oxygen functional groups were detached in this range.[16] In case of GO-OA_CDI and GO-OA, weight loss around 200 °C was much lower than that of pristine GO, meaning the ratio of oxygen functional groups were lower than that of GO. Moreover, after thermal treatment, large amount of the oxygen-containing functional groups was removed, and almost no weight loss around 200 °C with TRGO-OA_CDI and TRGO-OA. The functionalized OA groups on to graphene nanosheets started to detach near 300 °C with GO-derivatives while GO had no change in weight in this region. All these measurements strongly confirmed that OA was covalently functionalized on the GO surface, and oxygen-containing functional groups were removed well by additional thermal treatment.

After that, the synthesized GO-derivatives were applied as the lubricant additives to improve friction properties in the gear oil. Tribometer was used to investigate tribological properties of the GO-based additives in commercial gear oil. Friction testing results were shown in **Figure 3.18**. Initially, commercial gear oil without the additive (lubricant) has high friction coefficient about 0.087. When GO-OA and GO-OA_CDI were added, friction coefficient was significantly decreased up to 0.013 and 0.023, respectively. Furthermore, thermally reduced graphene additives represented much improved performance with 0.0080 and 0.0010, corresponding to TRGO-OA, TRGO-OA_CDI, respectively. This result means graphene-based additives can greatly improve friction properties of commercial oil. Especially, friction coefficient of TRGO-OA_CDI was almost near to zero, which was ideal lubricant property. The combination of aggregation resistance with improving cohesive interaction between oil and GO derivatives, additional removing of oxygen-containing functional groups, and mechanical stability of graphene-based materials makes synergistic effect to improve friction efficiency.

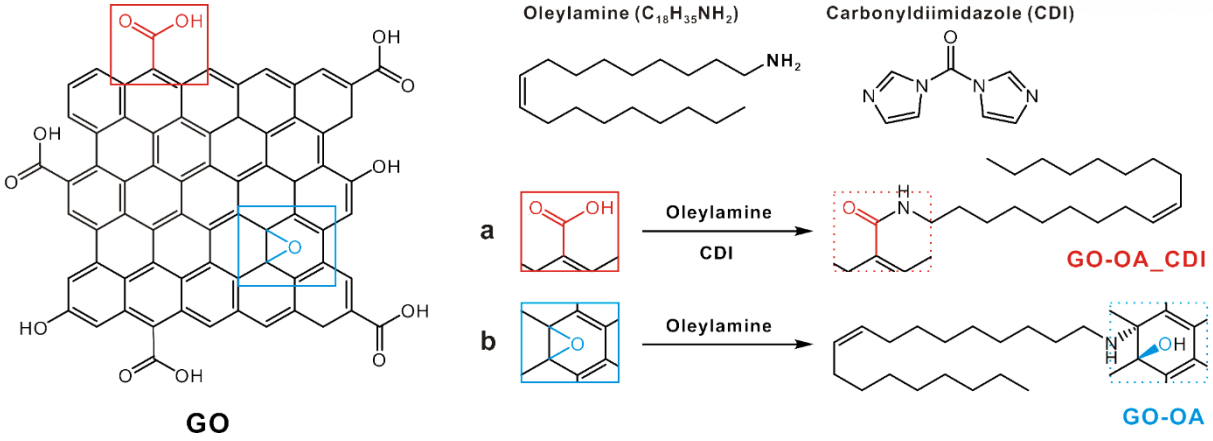

Figure 3.13. Representative scheme to synthesize oleylamine-functionalized GO by (a) CDI chemistry, and (b) thermal addition.

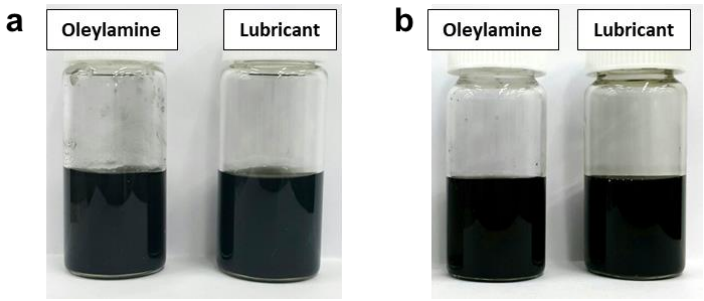

Figure 3.14. Images of (a) GO-OA_CDI, (b) GO-OA dispersions in OA solvent and lubricant oil, respectively. (Concentration: 1.0 mg mL^{-1})

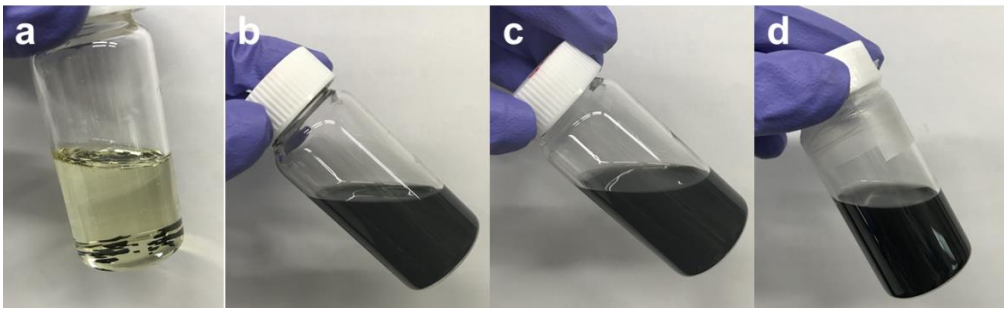

Figure 3.15. Images of (a) GO, (b) GO-OA, (c) TRGO-OA, and (d) TRGO-OA_CDI dispersions in the lubricant oil solvent. (Concentration: 1.0 mg mL^{-1})

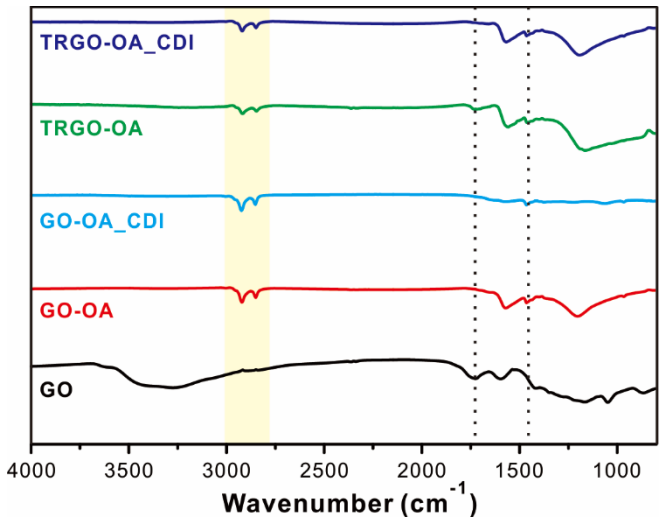

Figure 3.16. FT-IR spectra of GO, GO-OA, GO-OA_CDI, TRGO-OA, and TRGO-OA_CDI. Additional peaks at 2966 and 2865 cm^{-1} indicating asymmetric and symmetric stretching modes of C-H bonding from OA molecule

Table 3.7. Atomic Ratio (%) of GO-Derivatives Measured by XPS.

	C1s	O1s	N1s	C/O ratio
GO	71.1	27.4	0.00	2.59
GO-OA	87.0	7.37	4.33	11.8
GO-OA_CDI	85.1	12.2	2.67	8.96
TRGO-OA	92.0	3.70	3.33	24.9
GO	71.1	27.4	0.00	2.59

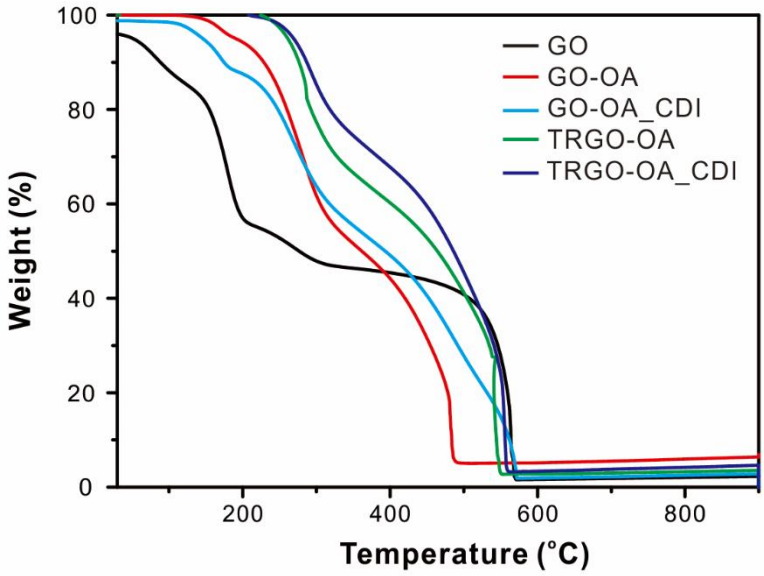

Figure 3.17. TGA measurement of GO-derivatives. Temperature was controlled from 0 to 900 °C with 10 °C min^{-1}.

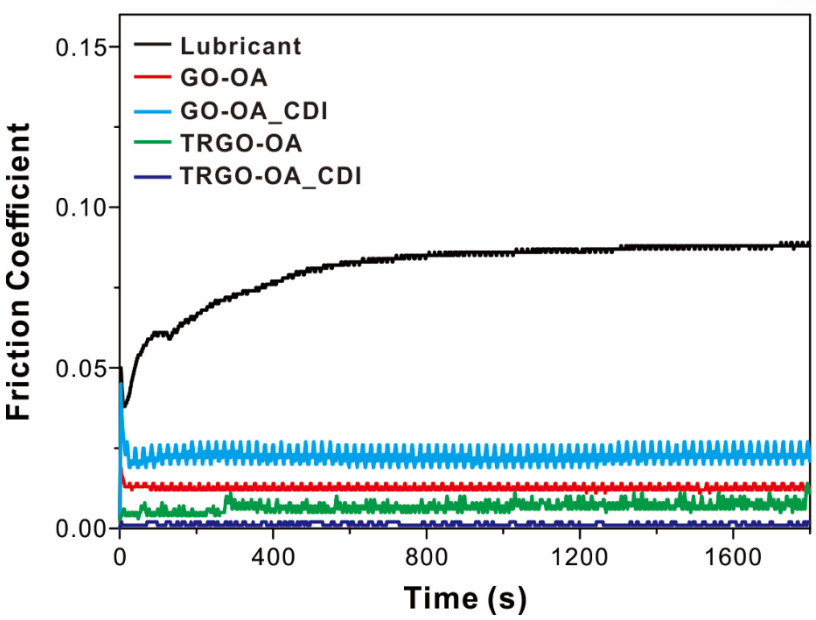

Figure 3.18. Friction coefficient of commercial lubricant oil with and without GO-based additives.

3.3.4. Conclusion

In summary, OA molecules were covalently introduced on to graphene surface to improve dispersion stability of GO-derivatives in lubricant oil. As a result, OA-functionalized GO-derivatives represented superior friction performance. Since their unique functional groups increase cohesive interactions between solvent and additives, graphene-derivatives in the lubricant oil has excellent dispersion stability and prevent the contact of two metal surfaces. Moreover, additional thermal annealing removed oxygen functional groups, which could further reduce friction between graphene nanosheets. Finally, the combination of aggregation resistance with improving cohesive interaction between oil and GO derivatives, additional removing of oxygen-containing functional groups, and mechanical stability of graphene-based materials makes synergistic effect to improve friction efficiency.

3.3.5. References

(1) Grossiord, C.; Varlot, K.; Martin, J. M.; Le Mogne, T.; Esnouf, C.; Inoue, K., MoS_2 Single Sheet Lubrication by Molybdenum Dithiocarbamate. *Tribol. Int.* **1998,** *31*, 737-743.

(2) Kinoshita, H.; Nishina, Y.; Alias, A. A.; Fujii, M., Tribological Properties of Monolayer Graphene Oxide Sheets as Water-Based Lubricant Additives. *Carbon* **2014,** *66*, 720-723.

(3) Wei, Z.; Wang, D.; Kim, S.; Kim, S.-Y.; Hu, Y.; Yakes, M. K.; Laracuente, A. R.; Dai, Z.; Marder, S. R.; Berger, C.; King, W. P.; de Heer, W. A.; Sheehan, P. E.; Riedo, E., Nanoscale Tunable Reduction of Graphene Oxide for Graphene Electronics. *Science* **2010,** *328*, 1373-1376.

(4) Fu, X.; Wang, Y.; Pan, Y.; Wang, X., Friction-Reducing, Anti-Wear and Self-Repairing Properties of Sulfonated Graphene. *J. Wuhan Univ. Technol.* **2017,** *32*, 272-277.

(5) Li, Z.; Xu, C.; Xiao, G.; Zhang, J.; Chen, Z.; Yi, M., Lubrication Performance of Graphene as Lubricant Additive in 4-N-Pentyl-4'-Cyanobiphyl Liquid Crystal (5CB) for Steel/Steel Contacts. *Materials* **2018,** *11*, 2110.

(6) Choudhary, S.; Mungse, H. P.; Khatri, O. P., Dispersion of Alkylated Graphene in Organic Solvents and Its Potential for Lubrication Applications. *J. Mater. Chem.* **2012,** *22*, 21032-21039.

(7) Dou, X.; Koltonow, A. R.; He, X.; Jang, H. D.; Wang, Q.; Chung, Y.-W.; Huang, J., Self-Dispersed Crumpled Graphene Balls in Oil for Friction and Wear Reduction. *Proc. Natl. Acad. Sci. USA* **2016,** *113*, 1528-1533.

(8) Song, H.-J.; Jia, X.-H.; Li, N.; Yang, X.-F.; Tang, H., Synthesis of A-Fe_2O_3 Nanorod/Graphene Oxide Composites and Their Tribological Properties. *J. Mater. Chem.* **2012,** *22*, 895-902.

(9) Tang, Z.; Zhang, Z.; Han, Z.; Shen, S.; Li, J.; Yang, J., One-Step Synthesis of Hydrophobic-Reduced Graphene Oxide and Its Oil/Water Separation Performance. *J. Mater. Sci.* **2016,** *51*, 8791-8798.

(10) Liu, Z.; Niu, S.; Wang, N., Oleylamine-Functionalized Graphene Oxide as an Electron Block Layer Towards High-Performance and Photostable Fullerene-Free Polymer Solar Cells. *Nanoscale* **2017,** *9*, 16293-16304.

(11) Park, M.; Song, K.; Lee, T.; Cha, J.; Lyo, I.; Kim, B.-S., Tailoring Graphene Nanosheets for Highly Improved Dispersion Stability and Quantitative Assessment in Nonaqueous Solvent. *ACS Appl. Mater. Interfaces* **2016,** *8*, 21595-21602.

(12) Bagri, A.; Mattevi, C.; Acik, M.; Chabal, Y. J.; Chhowalla, M.; Shenoy, V. B., Structural Evolution During the Reduction of Chemically Derived Graphene Oxide. *Nat. Chem.* **2010,** *2*, 581-587.

(13) Zhang, F.; Jiang, H.; Li, X.; Wu, X.; Li, H., Amine-Functionalized GO as an Active and Reusable Acid–Base Bifunctional Catalyst for One-Pot Cascade Reactions. *ACS Catal.* **2014,** *4*, 394-401.

(14) Guan, L.-Z.; Wan, Y.-J.; Gong, L.-X.; Yan, D.; Tang, L.-C.; Wu, L.-B.; Jiang, J.-X.; Lai, G.-Q., Toward Effective and Tunable Interphases in Graphene Oxide/Epoxy Composites by Grafting

Different Chain Lengths of Polyetheramine onto Graphene Oxide. *J. Mater. Chem. A* **2014,** *2*, 15058-15069.

(15) Park, S.; An, J.; Potts, J. R.; Velamakanni, A.; Murali, S.; Ruoff, R. S., Hydrazine-Reduction of Graphite- and Graphene Oxide. *Carbon* **2011,** *49*, 3019-3023.

(16) Fan, Z.; Wang, K.; Wei, T.; Yan, J.; Song, L.; Shao, B., An Environmentally Friendly and Efficient Route for the Reduction of Graphene Oxide by Aluminum Powder. *Carbon* **2010,** *48*, 1686-1689.

Chapter 4.
Bifunctional Graphene-Based Carbocatalyst for Biomass Reforming

4.1. Introduction

Demand for energy has increased rapidly, however, fossil fuels are not sufficient to satisfy this ever-increasing worldwide energy demand. Moreover, the burning of fossil fuels has caused a large increase in greenhouse gases and decomposition of the carbon cycle.[1-3] The cumulative impacts of fossil fuels have prompted the search for alternative energy sources. In this context, biomass holds promise as a feedstock for future sources of energy.[4-6] Biomass is an abundant and clean renewable energy resource for production of biofuels and value-added chemicals. Energy production from biomass has the advantage of forming smaller quantities of greenhouse gases compared with that from fossil fuels. Moreover, the carbon dioxide generated during energy production can be consumed during subsequent biomass regrowth.

Among biomass feedstocks, the two most abundant carbohydrates, glucose and fructose, are ideal candidates to replace fossil fuels and hold significant potential as future energy resources.[7] To date, many approaches have been developed to provide efficient routes to convert biomass into valuable fuels and chemicals.[8] Among the many bio-based products, furan-based compounds are rich sources of a variety of derivatives for fuel and chemical production. In particular, 5-hydroxymethylfurfural (HMF) is regarded as a key building block in the biomass conversion process. According to an evaluation by the U.S. Department of Energy, HMF is placed in the top 10 list of bio-based chemicals, due to its great potential for production of fuels and bulk chemicals.[9-11] Although HMF can be easily obtained from fructose, using a Brønsted acid at high temperature,[12-13] conversion from glucose, the dominant monomer in cellulosic biomass, remains a significant challenge.[8]

To convert glucose to HMF, strong acid catalysts are typically required for each step, thus, significant research efforts have focused on the use of metal-based catalysts.[7, 13-14] Despite their good catalytic activity, metal-based catalysts are toxic, which raises concerns for sustainability and environmental issues. Alternatively, homogeneous Brønsted and Lewis acid catalysts, such as H_2SO_4, HCl, and boric acid, have been introduced, albeit with a moderate glucose conversion performance.[15-17] In previous research by Ståhlberg and coworkers, boric acid was used as a cocatalyst to produce HMF from glucose.[17] The diol structure of boric acid formed a stable complex with the carbohydrates and promoted the isomerization of glucose. Although boric acid produced a good HMF yield without the use of a metal complex, in general, homogeneous catalysts often suffer from poor product separation, recycling, and problems with corrosion. In this context, rational strategies toward environmentally benign and effective catalysts remain an important issue.

Along this line, graphene oxide (GO) and its derivatives are promising metal-free

heterogeneous catalysts due to their unique physical and chemical properties, including an atomically thin two-dimensional structure with a high surface area, easy recyclability, and a variety of functional groups.[18-22] For example, GO contains epoxides and hydroxyl groups on the basal planes, whereas carboxylic acids and other functional groups are present at the edge sites, which can be further tailored to various functionalities.[23-24] In this context, GO and its derivatives can serve as an ideal platform for catalytic conversions.[22] Thus far, several groups have successfully demonstrated the use of GO and its derivatives as carbocatalysts for synthetic transformations such as oxidation,[18] C–H activation,[25] epoxide ring opening,[26] acid or base reactions,[27] oxidative coupling[28-29] and Friedel-Crafts alkylation.[30]

Although preceding research on the use of carbon-based catalysts to convert fructose to HMF exists,[31-33] there are few cases which use glucose or cellulose as a starting substrate, due to the challenges of the process. Recently, the Chen group utilized sulfonated graphene quantum dots as a non-metallic catalyst to convert glucose to HMF; however, it had low catalytic activity for glucose conversion and its quasi-heterogeneous structure limited its facile recycling.[34]

As a part of our interest in graphene-based catalysts, we report herein a unique strategy to produce HMF directly from glucose, catalyzed by novel bifunctional metal-free carbocatalysts based on GO nanosheets (**Figure 4.1**). Specifically, we introduce two distinct types of catalytic moiety, boronic acid, and phenylsulfonic acid, onto the GO nanosheets (BS-GO). Tailored GO-based catalysts with unique bifunctional groups demonstrated significant catalytic performance for HMF production, compared to homogeneous catalysts. Furthermore, GO derivatives were easily recycled using a simple centrifugation method, which highlights the advantage of heterogeneous catalysts. Finally, we propose a putative mechanism for the conversion of glucose to HMF based on NMR results, which suggest a unique bifunctional catalytic effect involving the boronic acid and phenylsulfonic acid groups in BS-GO. We believe that our method provides a versatile strategy for customization of GO-based catalysts to achieve high performance in a desirable synthetic reaction, through the appropriate choice of functional moieties.

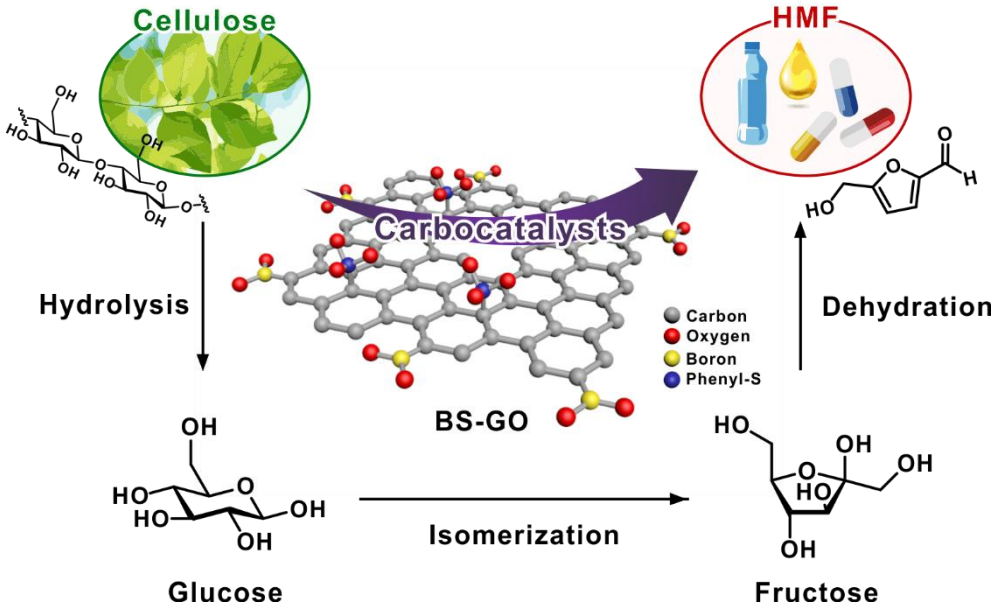

Figure 4.1. Schematic representation of the catalytic conversion of cellulose to HMF.

4.2. Experimental

4.2.1. Synthesis of the Carbocatalysts

Initially, graphite oxide powder was prepared using a modification of Hummer's method, and a brown dispersion of graphene oxide (GO) was exfoliated by sonication (conc. Of 1.0 mg mL^{-1}). To synthesize B-GO, dried GO powder (0.1 g) was mixed uniformly with boric acid (0.1 g) and thermally annealed at 800 °C, for 2 h, under an argon atmosphere.[35] Subsequently, phenylsulfonic groups were introduced via diazonium chemistry (BS-GO).[36] B-GO was dispersed under sonication (conc. 1.0 mg mL^{-1}). The aryl diazonium salt was prepared in water, from the reaction of sulfanilic acid (460 mg) and sodium nitrite (200 mg) in 100 mL of water. After 1.0 M HCl solution (7.0 mL) was added to this mixture, in an ice bath, the solution color changed from pale yellow to colorless. The dispersion was stored in the ice bath for more than 2 h and then subjected to extensive dialysis (Spectra/Por MWCO 12–14 K) for 4 days to remove any byproducts and remaining reactants. For the control experiment, S-GO was phenylsulfonated using the same method as used for BS-GO, without the boron-doping process.

4.2.2. Structural Characterization

FT-IR spectroscopy, in ATR-mode, was used to identify the chemical structures of GO-derivatives (Varian 670, wavenumber range: 650-4000 cm^{-1}). X-ray photoelectron spectroscopy (XPS, Thermo Fisher, K-alpha) was used to determine the elemental compositions and the chemical bonding of the GO-derivatives. The heteroatom-doping and structural changes were confirmed by Raman spectroscopy (LabRam Aramis). The structures and morphologies of the carbocatalysts were analyzed using SEM with EDS mapping (JEOL-7800F).

4.2.3. Investigating the Catalytic Performance

[EMIM]Cl (1.0 g) was melted at 80 °C, glucose (100 mg) and a catalyst (2.5 mg) were added. To identify the catalytic mechanism, glucose, deuterated at the C-2 position (*D*-Glucose-2-d_1), and $CrCl_2$ were added. The concentration of each product was measured by high-performance liquid chromatography (HPLC, Prominence, Shimadzu) equipped with a Shim-pack GIS C18 (5 μm, 250 mm length x 4.6 mm diameter) column and a UV detector (265 nm), using 7:3 v/v water:methanol as the mobile phase. The flow rate was constant at 1.0 mL min^{-1} and the injection volume was 5 μm. For the recycling process, the mixture was washed with water and methanol and centrifuged at 10000 rpm for 20 min.

4.3. Results and Discussion

4.3.1. Synthesis of GO-Derivatives

In the initial stage of our investigation, chemically modified GO-based carbocatalysts were synthesized from exfoliated GO nanosheets (**Figure 4.2**(a)). In brief, a GO suspension was synthesized following a modified Hummer's method.[37-38] As the boron atom was expected to provide immobilized active sites during the catalytic reaction of glucose isomerization, boron atoms were introduced onto GO nanosheets via thermal annealing of GO in the presence of boric acid (H_3BO_3). This resulted in the incorporation of boron into the graphene framework in different configurations with respect to oxygen (-BC_xO_y: -BC_2O or -BCO_2) and carbon (-BC_3) in the graphene lattice (denoted as boron-doped graphene oxide, B-GO, hereafter).[35, 39] Subsequently, the resulting B-GO was chemically functionalized by direct anchoring of sulfonic acid-containing aryl radicals. In this step, the phenylsulfonic acid moiety was grafted onto the basal plane of graphene via diazonium chemistry.[36, 40] Owing to its low pK_a value (−6.62), the phenylsulfonic acid group can provide a Brønsted acidic site in catalytic reactions.[41] Finally, boron-doped sulfonated graphene oxide (BS-GO) was prepared as a bifunctional carbocatalyst as described above. As a control, sulfonated graphene oxide (S-GO) was prepared to clarify the roles of the active sites in the carbocatalysts.

Successful chemical modification of GO was confirmed by FT-IR and X-ray photoelectron spectroscopy (XPS) analyses. The FT-IR spectra revealed that the pristine GO presented three characteristic peaks at 3200–3500, 1725, and 1315 cm^{-1}, attributable to the hydroxyl (–OH), carboxylic acid (–COOH), and epoxy (C–O–C) groups, respectively (**Figure 4.2**(b)).[42] Moreover, a characteristic peak at 1594 cm^{-1} indicated the presence of C=C bonds within the sp^2-network of graphene. Compared to that of GO, the C=C vibration peak for S-GO was slightly blue-shifted from 1594 to 1625 cm^{-1}, which indicated the partial conversion of the sp^2-graphitic lattice upon sulfonation.[43] Additional peaks appeared at 1382 and 1072 cm^{-1}, which were assigned as asymmetric and symmetric S=O stretching, confirming the presence of the sulfonic acid group.[36, 40] After introducing boron into B-GO, the overall intensity of oxygen functional groups was significantly reduced, due to the removal of oxygen containing functional groups upon annealing. The C=C vibration peaks in both B-GO and BS-GO were red-shifted from 1594 to 1558 cm^{-1}, indicating reduction of GO.[43] The boron doping was confirmed by the appearance of new peaks corresponding to B–C (1153 cm^{-1}) and B–O (~1000 cm^{-1}) in both B-GO and BS-GO.[35, 42]

The presence of boron species and phenylsulfonic acid groups was further investigated by XPS analysis (**Figure 4.2**(c)). The pristine GO showed the presence of only carbon and oxygen atoms, with a trace amount of sulfur, which originated from the sulfuric acid in the GO synthesis.[41] XPS revealed that a significant boron content (approximately 4.78 at.%) was incorporated into B-GO during the annealing process, which was absent in the pristine GO and S-GO (**Table 4.1**). In the same line, the C/O ratio of B-GO increased from 2.59 to 9.73, indicating that oxygen functional groups

were removed by the annealing process. Moreover, the amount of boron in BS-GO was almost unchanged (4.15%) during functionalization with the sulfonic acid group. The slight decrease in the C/O ratio from B-GO to BS-GO implies that the sulfonic acid group was successfully grafted onto the graphene sheets. The deconvoluted high-resolution B1s XPS spectrum elucidated the different types of boron configuration on the graphene nanosheets, which were bonded to oxygen (-BC_xO_y (-BC_2O or -BCO_2): 190.98 eV) and carbon (-BC_3: 192.68 eV) (**Figure 4.3**).[35] The content of -BC_xO_y in BS-GO was slightly decreased from 66.6% to 40.0% compared to B-GO since some of the boronic acid sites were detached upon introduction of the phenylsulfonic acid group.

In parallel, structural changes during functionalization were investigated by Raman spectroscopic analysis (**Figure 4.4**). GO presented two prominent bands, the symmetric A_{1g} mode of the D band (1346 cm^{-1}) and the E_{2g} mode of the G band (1597 cm^{-1}).[44] The D band is related to a disordered carbon lattice such as defects, edges, or an amorphous structure, while the G band corresponds to in-phase vibration of the graphitic sp^2-carbon lattice. The I_D/I_G intensity ratio for S-GO was slightly higher due to introduction of phenylsulfonic acid groups onto the sp^2-carbon lattice. Similarly, the I_D/I_G ratios of B-GO and BS-GO were higher than that of pristine GO, due to the boron doping.

Dispersion stability of GO-derivatives is a useful tool to determine chemical functionalization (**Figure 4.5**). While B-GO lost its aqueous dispersibility, due to the removal of oxygen containing functional groups in the annealing process, BS-GO presented good dispersion behavior, as the charged sulfonate groups prevented the graphene sheets from aggregating. The structures and morphologies of the carbocatalysts were analyzed using scanning electron microscopy (SEM). All the GO-based carbocatalysts clearly had crumpled and wrinkled paper-like morphologies (**Figure 4.6**). This reflects that the synthetic approach, i.e. boron doping and the diazonium reaction, did not alter the intrinsic morphology of the graphene nanosheet. Moreover, the energy-dispersive X-ray spectrometric (EDS) imaging of the BS-GO nanosheets indicated that the boron and sulfur were uniformly distributed in BS-GO nanosheets. Taken together, the above results indicate that boronic acid and phenylsulfonic acid groups had been successfully introduced into the graphene lattice.

4.3.2. Catalytic Reaction to Convert Glucose to HMF

The synthesized GO-derivatives were tested as metal-free catalysts for producing HMF from biomass. It is well known that HMF can be selectively produced from fructose or other sugars in DMSO, as DMSO itself acts as a catalyst[45-47] by promoting the formation of the furanoid form of fructose and facilitating its subsequent dehydration to HMF. As a preliminary experiment, we confirmed that the HMF yield from fructose in DMSO was high even in the absence of a catalyst (**Table 4.2** and **Table 4.3**). Moreover, all carbocatalysts exhibited much improved catalytic activity of approximately 80%, even with a short reaction time of 1 h (entries 3–10 in **Table 4.3**). Interestingly,

GO itself demonstrated an excellent performance of 88% conversion within 1 h, which originated from the Brønsted acidic sites of the carboxylic acid groups in GO nanosheet. In the same context, S-GO presented the best catalytic activity due to the presence of the Brønsted acidic sites of both phenylsulfonic acid and the carboxylic acid groups. The decreased in HMF yields over B-GO and BS-GO could originate from their structures. As shown in the XPS measurement, oxygen containing functional groups were detached during the annealing process, resulting in a decrease in Brønsted acid density (**Table 4.1**). Moreover, the diol structure of boronic acid may form a stable diboron intermediate complex with fructose, which could inhibit its dehydration to HMF (**Figure 4.7**).[17]

Based on these results, we explored the reactivity of glucose with GO-derivatives in DMSO (**Table 4.4**). Unfortunately, they showed a very low HMF yield of less than 8% even at high temperatures and long reaction times. Therefore, the solvent was changed to the sugar-solubilizing ionic liquid, 1-ethyl-3-methylimidazolium chloride ([EMIM]Cl), which has been reported to be an efficient medium for reforming biomass to HMF.[7] First, the reaction temperature and time were optimized with the BS-GO catalyst in [EMIM]Cl (**Table 4.5** and **Figure 4.8**). The maximum HMF yield was achieved at 130 °C in 3 h and the yield was improved by up to 21.0% under these conditions.

Table 4.6 lists the results for HMF yield via conversion of glucose under different reaction conditions. In general, catalytic activity was improved with an increase in the reaction temperature from 100 to 130 °C (entries 2–4 in **Table 4.6**). However, yield decreased marginally at temperatures of over 130 °C due to the formation of undesired byproducts, such as rehydration compounds and condensation products (**Table 4.6**, entry 5). Additionally, we investigated the influence of the concentration of catalyst on the catalytic performance (entries 4, 6, 9 in **Table 4.6**). Unexpectedly, the yield gradually decreased from 36.5% to 21.0% with the increase in catalyst load. A similar observation was reported for the use of a boric acid promoter for the dehydration of glucose.[17] Specifically, at high concentrations of boric acid catalyst, a stable diboron-fructose complex formed, which was responsible for inhibiting the conversion of fructose (**Figure 4.7**). Since the diboron-fructose complex is difficult to decompose into fructose, the subsequent dehydration of fructose to HMF was inhibited. This phenomenon clearly explains why the B-GO and BS-GO catalysts produced lower HMF yields from fructose than did the GO catalyst (entries 7–10 in **Table 4.3**). A more extensive screening was performed by varying the reaction time for the production of HMF from glucose over the BS-GO catalyst (entries 7–9 in **Table 4.6**). The conversion of glucose was almost complete within 1 h and the yield of HMF only increased slightly with longer reaction times. The maximum yield, of up to 36.5% was achieved within 3 h, which is a 2.4-fold improvement over the non-catalyzed reaction.

Figure 4.9 summarizes the catalytic conversion of glucose to HMF with the carbocatalysts. Although pristine GO did not enhance the conversion of glucose to HMF (entry 10 in **Table 4.6**), both

S-GO and B-GO showed improved performance (entry 11, 12 in **Table 4.6**) and BS-GO produced the best yield, of 36.5%. When boron was introduced into GO (B-GO), catalytic activity rapidly increased from 15.1 to 32.2% conversion, which implies that the boronic acid site played a vital role in this catalytic system. To confirm the contribution of the boronic acid sites in this catalytic transformation, phenylboronic acid was used as a molecular analogue of the carbocatalytic system to mimic its catalytic activity (entry 13 in **Table 4.6**). Impressively, it exhibited a 33.6% yield of HMF, which is comparable to BS-GO. All these results strongly indicate that introducing boronic acid into GO-derivatives played a critical role in converting glucose to HMF. The BS-GO catalyst, which contains both boronic and Brønsted acid sites, is more effective in producing HMF than the catalysts incorporating the individual boronic (B-GO) and Brønsted (S-GO) acid sites. The two disjunct moieties, boronic acid and phenylsulfonic acid, demonstrate a unique bifunctional effect in a single nanosheet of BS-GO catalyst, resulting in excellent catalytic performance.

4.3.3. Putative Mechanism Study from Glucose to HMF

To date, the non-stoichiometric nature of GO has presented a considerable challenge to understanding the catalytic mechanism of carbocatalysts.[48] Several groups have reported unique methods of investigating the mechanisms of a variety of reactions over GO-based carbocatalysts. As a notable example, Loh group tried to overcome this limitation by using electron spin resonance (ESR) spectroscopy to examine the origin of the catalytic active sites of GO.[49] Herein, we introduced glucose, deuterated at the C-2 position (*D*-Glucose-2-d_1, **Figure 4.10**(a)) in order to identify the carbocatalytic mechanism of HMF production from glucose. The reaction of deuterated glucose would produce different ratios of isotope-labeled products according to their reaction pathway. There are two possible pathways from glucose to HMF; the hydride transfer route and the ene–diol route. In the case of the hydride transfer route, the deuterium would be transferred, to afford fructose deuterated at the C-1 position exclusively. The subsequent dehydration to HMF would afford 50% of deuterated HMF in the final product. In contrast, in the ene–diol mechanism a ketone would form at the C2 position of glucose, which would eliminate all the deuterium. Thus, no deuterium could be incorporated in the HMF molecule.

It is well known that Cr-based catalysts and the glucose isomerase enzyme follow the hydride transfer route (**Figure 4.10**(a)). We compared the reaction mechanisms of BS-GO and $CrCl_2$ catalysts by use of deuterated glucose. In the ^{1}H NMR spectra (**Figure 4.10**(b)), the integration ratio between the C-1 and C-4 positions of HMF was approximately 0.59 (I_a/I_c) when the Cr-based catalyst was used, which implies that 41% of the HMF molecules were deuterated. The BS-GO catalyzed reaction proceeded via a different reaction mechanism compared to the Cr-based catalyst. All the deuterium was eliminated and the ratio of C-1 to C-4 was approximately 1.04 (I_a/I_c), clearly displaying that the isomerization of glucose to fructose over BS-GO proceeds via an ene–diol

intermediate, unlike that over metal-based catalysts.

Based on these results, we propose a putative mechanism for the conversion of glucose to HMF over the BS-GO catalyst (**Figure 4.11**). Selective isomerization of glucose could proceed through the formation of an ene–diol intermediate. First, the boronic acid sites would form a complex with a glucose diol (**Figure 4.11**a). An open-chain glucose-boronic acid, coordinated to the 3- and 4-positions would be generated (**Figure 4.11**b). The chelating effect of the boronic acid would stabilize the open-chain complex and the O-B-O angle would be less strained in open-chain glucose. Subsequently, the acidic conditions would protonate O1, resulting in an ene-diol intermediate (**Figure 4.11**c). Proton exchange would form the closed-ring structure (**Figure 4.11**d). Finally, BS-GO would be regenerated upon the formation of fructose. Subsequently, the Brønsted acidic phenylsulfonic acid groups (-SO_3H) would serve as catalytic active sites for the dehydration of fructose to HMF.

4.3.4. Recyclability Test

To verify the utility of BS-GO as a heterogeneous catalyst, a recycling test, up to the fifth cycle, was conducted. **Figure 4.12** shows the isolated yields of HMF for the catalytic regeneration experiment. As noted, the bifunctional BS-GO carbocatalyst presents good recyclability and can be reused after simple centrifugation and rinsing with methanol and water. Although there is a slight decrease in activity up to the 5^{th} cycle, the catalytic performance remains comparable to that of homogeneous catalysts. Moreover, the high yield was achieved with low catalyst loading, which is unprecedented in previous carbocatalyst research, which makes this study a good model for practical applications.

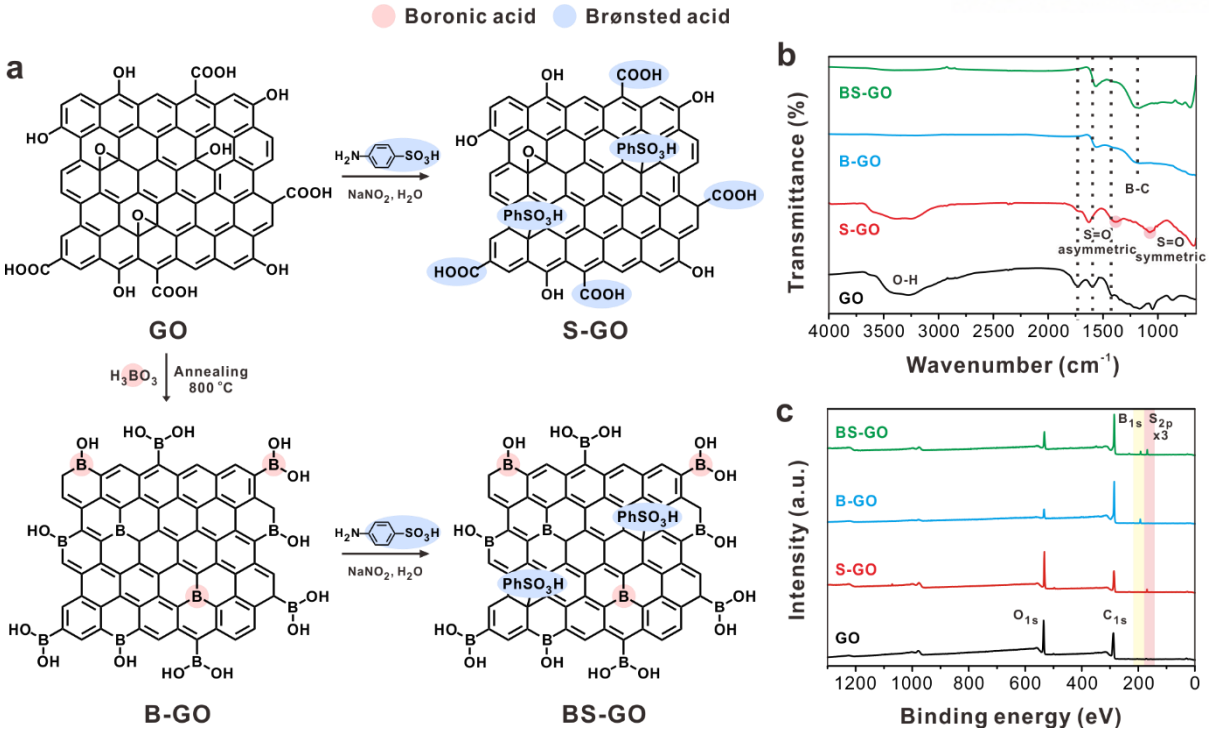

Figure 4.2. (a) Synthetic approaches to the GO-based carbocatalysts, (b) FT-IR spectra, and (c) XPS survey spectra of the GO-based carbocatalysts used in this study.

Table 4.1. Relative Atomic Compositions Based on XPS Measurements.

Catalyst	Atomic ratio measured by XPS (at.%)				
	C1s	O1s	B1s	S2p	C/O ratio
GO	71.1	27.4	ND	0.7	2.59
S-GO	66.7	30.9	ND	1.00	2.16
B-GO	84.8	8.71	4.78	ND	9.73
BS-GO	78.2	14.8	4.15	1.67	5.29

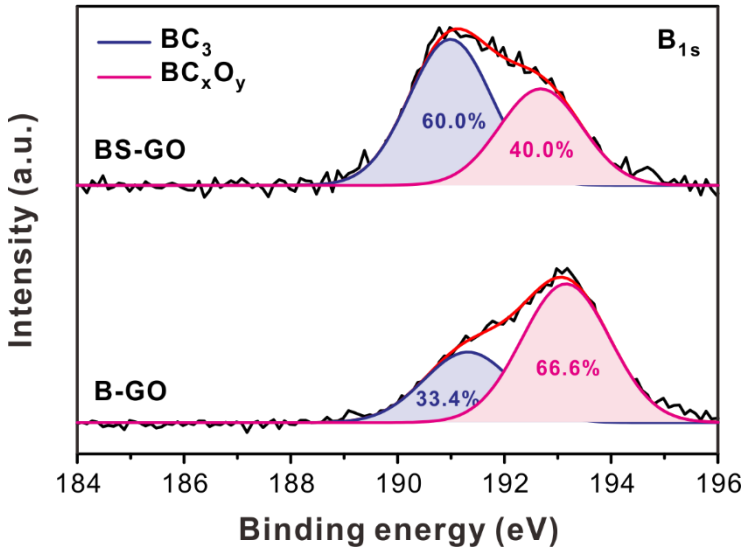

Figure 4.3. Deconvoluted high-resolution XPS B1s spectra of B-GO and BS-GO.

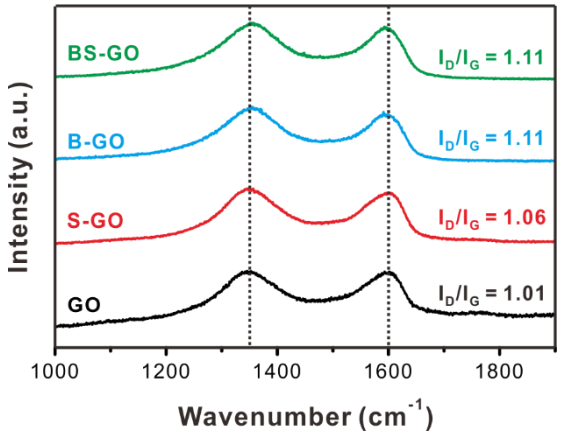

Figure 4.4. Raman spectra of GO and GO-derivatives. An argon ion laser, with a wavelength of 532 nm, was used as an excitation source. The D and G bands appear at 1346 cm^{-1} and 1600 cm^{-1}, respectively.

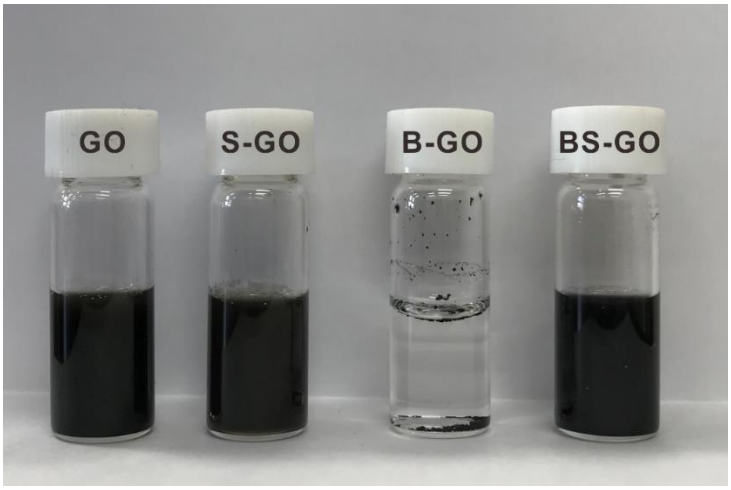

Figure 4.5. Photograph of GO-based catalysts suspension (labelled) in water (conc. of 0.5 mg mL^{-1}).

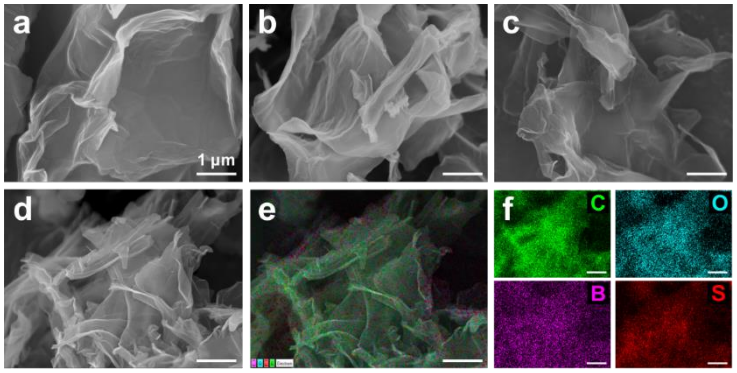

Figure 4.6. SEM images of (a) GO, (b) S-GO, (c) B-GO, and (d) BS-GO. (e, f) Corresponding EDS elemental mapping images of BS-GO. All scale bars indicate 1 μm.

Table 4.2. HMF Yields from Fructose under a Variety of Conditions.[a]

Entry	Temperature (°C)	Time (h)	Atmosphere	Pressure (MPa)	HMF yield (%)
1	130	1	N_2	0.4	0.017
2	130	2	N_2	0.4	0.056
3	130	3	N_2	0.4	0.052
4	140	1	N_2	0.4	0.019
5	140	2	N_2	0.4	0.065
6	140	3	N_2	0.4	0.109
7	150	1	N_2	0.4	0.037
8	150	2	N_2	0.4	0.262
9	140	1	N_2	0.2	3.742
10	140	2	N_2	0.2	2.550
11	140	3	N_2	0.2	7.321
12	140	4	N_2	0.2	8.078
13	140	0.5	Air	0.1	42.27
14	140	1	Air	0.1	62.12
15	140	2	Air	0.1	56.32
16	140	3	Air	0.1	57.46
17	150	1	Air	0.1	73.43
18	150	2	Air	0.1	78.91

[a]Reaction conditions: Fructose 1.0 g, DMSO 10 mL, without catalyst.

Table 4.3. HMF Yields from Fructose with the GO-Based Carbocatalysts Prepared in This Study.[a]

Entry	Catalyst	Time (h)	HMF yield (%)
1	No catalyst	1	73.4
2	No catalyst	2	78.9
3	GO	1	88.0
4	GO	2	87.9
5	S-GO	1	88.0
6	S-GO	2	89.2
7	B-GO	1	77.5
8	B-GO	2	81.7
9	BS-GO	1	81.4
10	BS-GO	2	84.3

[a]Reaction conditions: Fructose 1.0 g, catalyst 10 mg, DMSO 10 mL, at 150 °C, under an air atmosphere.

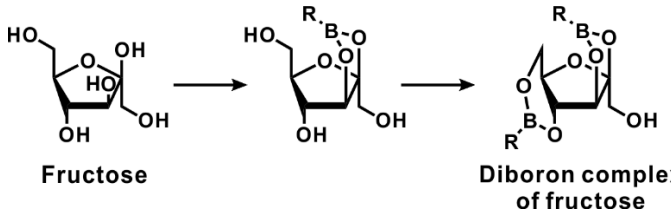

Figure 4.7. Schematic representation of diboron complex formation at high catalyst concentrations.

Table 4.4. HMF Yields from Glucose in DMSO.[a]

Entry	Catalyst	Time (h)	HMF yield (%)
1	GO	4	4.56
2	GO	8	7.32
3	GO	12	7.79
4	BS-GO	4	1.41
5	BS-GO	8	2.36
6	BS-GO	12	3.32

[a]Reaction conditions: Glucose 1.0 g, catalyst 10 mg, DMSO 10 mL, at 140 °C, under an air atmosphere.

Table 4.5. Changes in HMF Yields with Temperature and Reaction Time. (Reaction Conditions: Glucose 1.0 g, BS-GO 10 mg, EMIM[Cl] 10 mL, under an Air Atmosphere.)

	Yield (%)			
Reaction time (h)	100 ℃	120 ℃	130 ℃	140 ℃
1	5.47	16.02	19.11	18.65
2	7.97	16.98	20.50	14.54
3	7.83	18.18	21.02	12.22
4	8.75	16.68	18.87	11.22
5	8.94	15.72	15.21	8.43
6	9.68	17.18	14.80	6.36

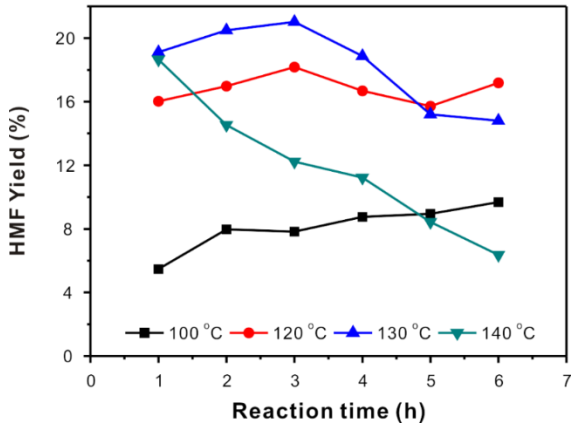

Figure 4.8. Changes in HMF yields from glucose, over BS-GO, with temperature and reaction time.

Table 4.6. HMF Yields from Glucose over the GO-Based Carbocatalysts Prepared in This Study.[a]

Entry	Catalyst	Mass (mg)	Temperature (°C)	Time (h)	HMF yield (%)
1	No catalyst	0	130	3	15.2
2	BS-GO	10	100	3	7.83
3	BS-GO	10	120	3	18.2
4	BS-GO	10	130	3	21.0
5	BS-GO	10	140	3	12.2
6	BS-GO	5.0	130	3	23.1
7	BS-GO	2.5	130	1	34.4
8	BS-GO	2.5	130	2	35.7
9	BS-GO	2.5	130	3	36.5
10	GO	2.5	130	3	15.1
11	S-GO	2.5	130	3	20.5
12	B-GO	2.5	130	3	32.2
13	Phenylboronic acid	2.5	130	3	33.6

[a]Reaction conditions: glucose 0.1 g, [EMIM]Cl 1.0 mL, under an air atmosphere.

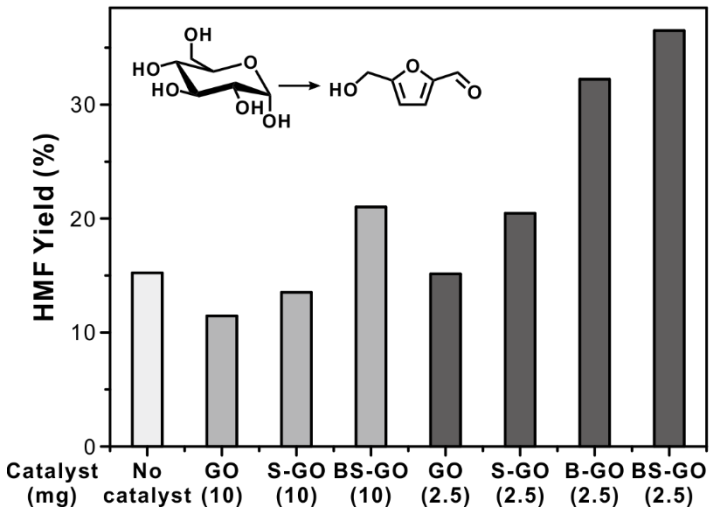

Figure 4.9. HMF yields from glucose over the carbocatalysts. Reaction conditions: glucose 0.1 g, solvent 1.0 mL, at 130 °C, under an air atmosphere.

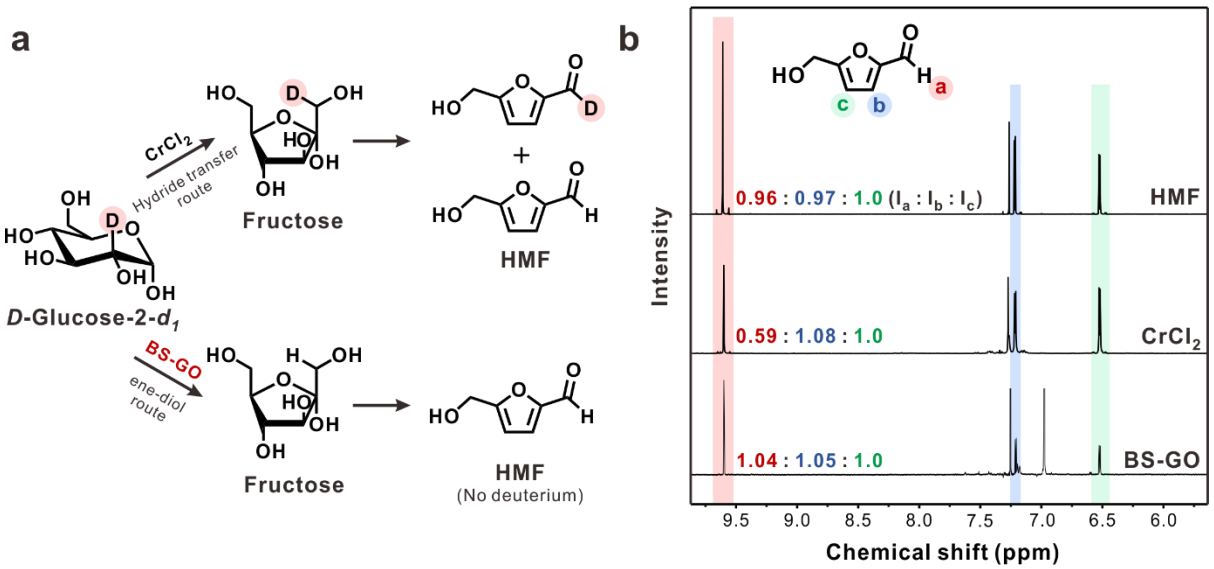

Figure 4.10. (a) Two representative reaction pathways from *D*-Glucose-2-d_1 to HMF, and (b) ^{1}H NMR spectra of standard HMF and HMF produced from deuterated glucose, using $CrCl_2$ and BS-GO catalysts. All spectra were collected in $CDCl_3$.

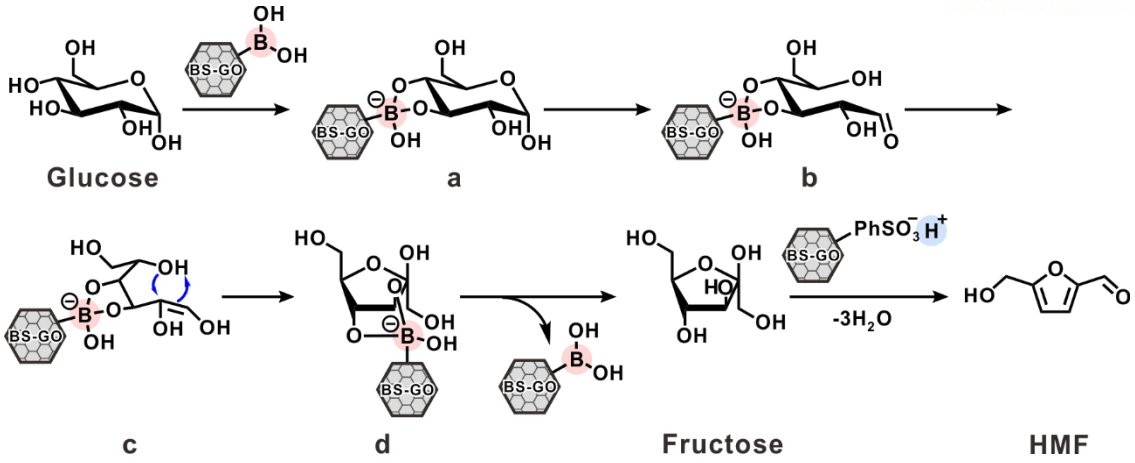

Figure 4.11. Reaction mechanism for HMF production from glucose with BS-GO as the catalyst.

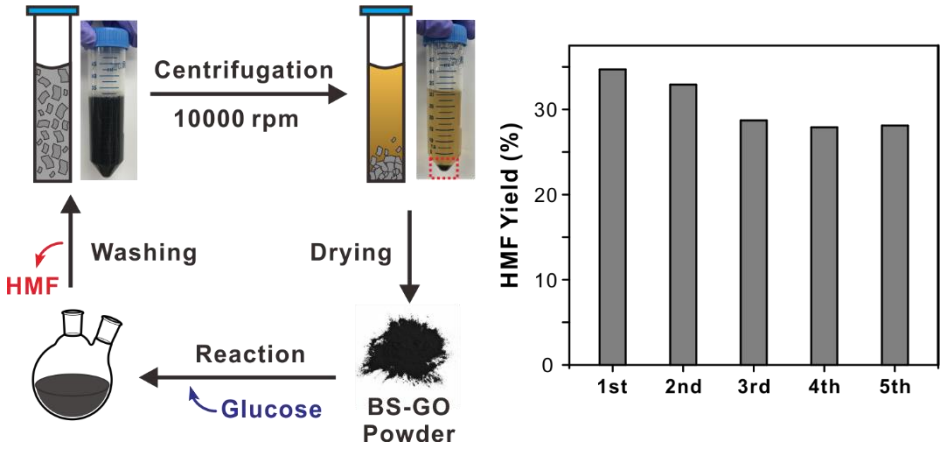

Figure 4.12. Recycling test for the production of HMF over the BS-GO catalyst. Reaction conditions: Glucose 1.0 g, solvent 10 mL, catalyst 25 mg, at 130 °C, under an air atmosphere.

4.4. Conclusion

We developed metal-free bifunctional GO-based catalysts and demonstrated that BS-GO is a highly efficient and robust carbocatalyst for the direct conversion of glucose into HMF in a one-pot reaction. Two disjunct moieties; boronic acid and phenylsulfonic acid, show a unique bifunctional effect in a single nanosheet of BS-GO catalyst, resulting in excellent catalytic performance for the production of HMF. Owing to the heterogeneous structure of BS-GO, it was easily reusable and the HMF yield was satisfactory up to the 5^{th} cycle. Furthermore, we investigated the catalytic mechanism using analogue molecules and deuterated glucose to determine the origin of the active sites. In the BS-GO catalyst, the boronic acid site plays a critical role in converting glucose to HMF. Selective isomerization of glucose proceeded through the formation of an ene–diol intermediate, and the Brønsted acid, phenylsulfonic acid, completed the reaction by dehydrating fructose to HMF. Although the catalytic performance is lower than that of metal-based and homogeneous catalysts, we anticipate that graphene-derivatives will be viable catalysts in diverse organic reactions and offer advantages in terms of sustainability, as green catalysts.

4.5. References

(1) Bailis, R.; Ezzati, M.; Kammen, D. M., Mortality and Greenhouse Gas Impacts of Biomass and Petroleum Energy Futures in Africa. *Science* **2005,** *308*, 98-103.

(2) Goldemberg, J., Ethanol for a Sustainable Energy Future. *Science* **2007,** *315*, 808-810.

(3) Caes, B. R.; Palte, M. J.; Raines, R. T., Organocatalytic Conversion of Cellulose into a Platform Chemical. *Chem. Sci.* **2013,** *4*, 196-199.

(4) Huber, G. W.; Chheda, J. N.; Barrett, C. J.; Dumesic, J. A., Production of Liquid Alkanes by Aqueous-Phase Processing of Biomass-Derived Carbohydrates. *Science* **2005,** *308*, 1446-1450.

(5) Rubin, E. M., Genomics of Cellulosic Biofuels. *Nature* **2008,** *454*, 841-845.

(6) Zhou, Y. J.; Kerkhoven, E. J.; Nielsen, J., Barriers and Opportunities in Bio-Based Production of Hydrocarbons. *Nat. Energy* **2018,** *3*, 925-935.

(7) Zhao, H.; Holladay, J. E.; Brown, H.; Zhang, Z. C., Metal Chlorides in Ionic Liquid Solvents Convert Sugars to 5-Hydroxymethylfurfural. *Science* **2007,** *316*, 1597-1600.

(8) Besson, M.; Gallezot, P.; Pinel, C., Conversion of Biomass into Chemicals over Metal Catalysts. *Chem. Rev.* **2014,** *114*, 1827-1870.

(9) van Putten, R.-J.; van der Waal, J. C.; de Jong, E.; Rasrendra, C. B.; Heeres, H. J.; de Vries, J. G., Hydroxymethylfurfural, a Versatile Platform Chemical Made from Renewable Resources. *Chem. Rev.* **2013,** *113*, 1499-1597.

(10) Bozell, J. J.; Petersen, G. R., Technology Development for the Production of Biobased Products from Biorefinery Carbohydrates—the Us Department of Energy's "Top 10" Revisited. *Green chem.* **2010,** *12*, 539-554.

(11) Werpy, T.; Petersen, G. Golden, CO (USA): **2004**.

(12) Brown, D. W.; Floyd, A. J.; Kinsman, R. G.; Roshanhyphen; Ali, Y., Dehydration Reactions of Fructose in Non-Aqueous Media. *Chem. Technol. Biotechnol.* **1982,** *32*, 920-924.

(13) Binder, J. B.; Raines, R. T., Simple Chemical Transformation of Lignocellulosic Biomass into Furans for Fuels and Chemicals. *J. Am. Chem. Soc.* **2009,** *131*, 1979-1985.

(14) Pidko, E. A.; Degirmenci, V.; van Santen, R. A.; Hensen, E. J. M., Glucose Activation by Transient Cr^{2+} Dimers. *Angew. Chem. Int. Ed.* **2010,** *49*, 2530-2534.

(15) Qi, L.; Mui, Y. F.; Lo, S. W.; Lui, M. Y.; Akien, G. R.; Horváth, I. T., Catalytic Conversion of Fructose, Glucose, and Sucrose to 5-(Hydroxymethyl)Furfural and Levulinic and Formic Acids in γ-Valerolactone as a Green Solvent. *ACS Catal.* **2014,** *4*, 1470-1477.

(16) Chidambaram, M.; Bell, A. T., A Two-Step Approach for the Catalytic Conversion of Glucose to 2,5-Dimethylfuran in Ionic Liquids. *Green chem.* **2010,** *12*, 1253-1262.

(17) Ståhlberg, T.; Rodriguez-Rodriguez, S.; Fristrup, P.; Riisager, A., Metal-Free Dehydration of Glucose to 5-(Hydroxymethyl)Furfural in Ionic Liquids with Boric Acid as a Promoter. *Chem. Eur. J.* **2011,** *17*, 1456-1464.

(18) Dreyer, D. R.; Jia, H.-P.; Bielawski, C. W., Graphene Oxide: A Convenient Carbocatalyst for Facilitating Oxidation and Hydration Reactions. *Angew. Chem. Int. Ed.* **2010,** *49*, 6813-6816.

(19) Su, C.; Loh, K. P., Carbocatalysts: Graphene Oxide and Its Derivatives. *Acc. Chem. Res.* **2013,** *46*, 2275-2285.

(20) Dreyer, D. R.; Bielawski, C. W., Carbocatalysis: Heterogeneous Carbons Finding Utility in Synthetic Chemistry. *Chem. Sci.* **2011,** *2*, 1233-1240.

(21) Navalon, S.; Dhakshinamoorthy, A.; Alvaro, M.; Garcia, H., Carbocatalysis by Graphene-Based Materials. *Chem. Rev.* **2014,** *114*, 6179-6212.

(22) Jeon, E. K.; Seo, E.; Lee, E.; Lee, W.; Um, M.-K.; Kim, B.-S., Mussel-Inspired Green Synthesis of Silver Nanoparticles on Graphene Oxide Nanosheets for Enhanced Catalytic Applications. *Chem. Commun.* **2013,** *49*, 3392-3394.

(23) Stankovich, S.; Dikin, D. A.; Piner, R. D.; Kohlhaas, K. A.; Kleinhammes, A.; Jia, Y.; Wu, Y.; Nguyen, S. T.; Ruoff, R. S., Synthesis of Graphene-Based Nanosheets Via Chemical Reduction of Exfoliated Graphite Oxide. *Carbon* **2007,** *45*, 1558-1565.

(24) Lee, T.; Jeon, E. K.; Kim, B.-S., Mussel-Inspired Nitrogen-Doped Graphene Nanosheet Supported Manganese Oxide Nanowires as Highly Efficient Electrocatalysts for Oxygen Reduction Reaction. *J. Mater. Chem. A* **2014,** *2*, 6167-6173.

(25) Gao, Y.; Tang, P.; Zhou, H.; Zhang, W.; Yang, H.; Yan, N.; Hu, G.; Mei, D.; Wang, J.; Ma, D., Graphene Oxide Catalyzed C−H Bond Activation: The Importance of Oxygen Functional Groups for Biaryl Construction. *Angew. Chem. Int. Ed.* **2016,** *55*, 3124-3128.

(26) Thomas, H. R.; Marsden, A. J.; Walker, M.; Wilson, N. R.; Rourke, J. P., Sulfur-Functionalized Graphene Oxide by Epoxide Ring-Opening. *Angew. Chem. Int. Ed.* **2014,** *53*, 7613-7618.

(27) Zhang, F.; Jiang, H.; Li, X.; Wu, X.; Li, H., Amine-Functionalized GO as an Active and Reusable Acid–Base Bifunctional Catalyst for One-Pot Cascade Reactions. *ACS Catal.* **2014,** *4*, 394-401.

(28) Shaikh, M.; Sahu, A.; Kiran Kumar, A.; Sahu, M.; Singh, S. K.; Ranganath, K. V. S., Metal-Free Carbon as a Catalyst for Oxidative Coupling: Solvent-Enhanced Poly-Coupling with Regioselectivity. *Green chem.* **2017,** *19*, 4533-4537.

(29) Su, C.; Tandiana, R.; Balapanuru, J.; Tang, W.; Pareek, K.; Nai, C. T.; Hayashi, T.; Loh, K. P., Tandem Catalysis of Amines Using Porous Graphene Oxide. *J. Am. Chem. Soc.* **2015,** *137*, 685-690.

(30) Hu, F.; Patel, M.; Luo, F.; Flach, C.; Mendelsohn, R.; Garfunkel, E.; He, H.; Szostak, M., Graphene-Catalyzed Direct Friedel–Crafts Alkylation Reactions: Mechanism, Selectivity, and Synthetic Utility. *J. Am. Chem. Soc.* **2015,** *137*, 14473-14480.

(31) Wang, H.; Kong, Q.; Wang, Y.; Deng, T.; Chen, C.; Hou, X.; Zhu, Y., Graphene Oxide Catalyzed Dehydration of Fructose into 5-Hydroxymethylfurfural with Isopropanol as Cosolvent. *ChemCatChem* **2014,** *6*, 728-732.

(32) Shaikh, M.; Singh, S. K.; Khilari, S.; Sahu, M.; Ranganath, K. V. S., Graphene Oxide as a

Sustainable Metal and Solvent Free Catalyst for Dehydration of Fructose to 5-HMF: A New and Green Protocol. *Catal. Commun.* **2018,** *106*, 64-67.

(33) Hou, Q.; Li, W.; Ju, M.; Liu, L.; Chen, Y.; Yang, Q., One-Pot Synthesis of Sulfonated Graphene Oxide for Efficient Conversion of Fructose into Hmf. *RSC Adv.* **2016,** *6*, 104016-104024.

(34) Li, K.; Chen, J.; Yan, Y.; Min, Y.; Li, H.; Xi, F.; Liu, J.; Chen, P., Quasi-Homogeneous Carbocatalysis for One-Pot Selective Conversion of Carbohydrates to 5-Hydroxymethylfurfural Using Sulfonated Graphene Quantum Dots. *Carbon* **2018,** *136*, 224-233.

(35) Sheng, Z.-H.; Gao, H.-L.; Bao, W.-J.; Wang, F.-B.; Xia, X.-H., Synthesis of Boron Doped Graphene for Oxygen Reduction Reaction in Fuel Cells. *J. Mater. Chem.* **2012,** *22*, 390-395.

(36) Ji, J.; Zhang, G.; Chen, H.; Wang, S.; Zhang, G.; Zhang, F.; Fan, X., Sulfonated Graphene as Water-Tolerant Solid Acid Catalyst. *Chem. Sci.* **2011,** *2*, 484-487.

(37) Hummers, W. S.; Offeman, R. E., Preparation of Graphitic Oxide. *J. Am. Chem. Soc.* **1958,** *80*, 1339-1339.

(38) Park, M.; Lee, T.; Kim, B.-S., Covalent Functionalization Based Heteroatom Doped Graphene Nanosheet as a Metal-Free Electrocatalyst for Oxygen Reduction Reaction. *Nanoscale* **2013,** *5*, 12255-12260.

(39) Zheng, Y.; Jiao, Y.; Ge, L.; Jaroniec, M.; Qiao, S. Z., Two-Step Boron and Nitrogen Doping in Graphene for Enhanced Synergistic Catalysis. *Angew. Chem. Int. Ed.* **2013,** *52*, 3110-3116.

(40) Si, Y.; Samulski, E. T., Synthesis of Water Soluble Graphene. *Nano Lett.* **2008,** *8*, 1679-1682.

(41) Park, M.; Song, K.; Lee, T.; Cha, J.; Lyo, I.; Kim, B.-S., Tailoring Graphene Nanosheets for Highly Improved Dispersion Stability and Quantitative Assessment in Nonaqueous Solvent. *ACS Appl. Mater. Interfaces* **2016,** *8*, 21595-21602.

(42) Acik, M.; Lee, G.; Mattevi, C.; Chhowalla, M.; Cho, K.; Chabal, Y. J., Unusual Infrared-Absorption Mechanism in Thermally Reduced Graphene Oxide. *Nat. Mater.* **2010,** *9*, 840-845.

(43) Xu, X.; Yuan, T.; Zhou, Y.; Li, Y.; Lu, J.; Tian, X.; Wang, D.; Wang, J., Facile Synthesis of Boron and Nitrogen-Doped Graphene as Efficient Electrocatalyst for the Oxygen Reduction Reaction in Alkaline Media. *Int. J. Hydrog. Energy* **2014,** *39*, 16043-16052.

(44) Kudin, K. N.; Ozbas, B.; Schniepp, H. C.; Prud'homme, R. K.; Aksay, I. A.; Car, R., Raman Spectra of Graphite Oxide and Functionalized Graphene Sheets. *Nano Lett.* **2008,** *8*, 36-41.

(45) Liu, R.; Chen, J.; Huang, X.; Chen, L.; Ma, L.; Li, X., Conversion of Fructose into 5-Hydroxymethylfurfural and Alkyl Levulinates Catalyzed by Sulfonic Acid-Functionalized Carbon Materials. *Green chem.* **2013,** *15*, 2895-2903.

(46) Lichtenthaler, F. W.; Rönninger, S., A-D-Glucopyranosyl-D-Fructoses: Distribution of Furanoid and Pyranoid Tautomers in Water, Dimethyl Sulphoxide, and Pyridine. Studies on Ketoses. Part 4. *J. Chem. Soc., Perkin Trans. 2* **1990**, 1489-1497.

(47) Román-Leshkov, Y.; Chheda, J. N.; Dumesic, J. A., Phase Modifiers Promote Efficient

Production of Hydroxymethylfurfural from Fructose. *Science* **2006,** *312*, 1933-1937.

(48) Fan, X.; Zhang, G.; Zhang, F., Multiple Roles of Graphene in Heterogeneous Catalysis. *Chem. Soc. Rev.* **2015,** *44*, 3023-3035.

(49) Su, C.; Acik, M.; Takai, K.; Lu, J.; Hao, S.-j.; Zheng, Y.; Wu, P.; Bao, Q.; Enoki, T.; Chabal, Y. J.; Ping Loh, K., Probing the Catalytic Activity of Porous Graphene Oxide and the Origin of This Behaviour. *Nat. Commun.* **2012,** *3*, 1298.

Chapter 5.
Graphene-Based Electrocatalyst

5.1. Introduction

Owing to unique structures and superior properties of GO, GO-based nanocomposites have emerged as an important material in the field of electrochemistry. For example, GO itself exhibits a moderate conductivity, and good chemical stability, and able to facilitate the direct electron transfer. In addition, the hybridization of inorganic nanomaterials can offer GO-based composites novel electrocatalytic properties. In this case, GO provides an ideal platform for the deposition of metal nanoparticles due to their various functionalities and high stability of GO nanosheets. Moreover, GO can improve catalytic stability during electrochemical reaction by preventing aggregation of active metal nanomaterials.

In Chapter 5, we introduce two different modification methods including chemical functionalization of GO and LbL assembly method to hybridize graphene-based materials with diverse metal nanoparticles.

5.1.1. Carbon-Based Electrocatalysts

Among various electrochemical system, three representative reactions, including the oxygen reduction (ORR), oxygen evolution reaction (OER), and hydrogen evolution reaction (HER), are critical for clean and renewable energy societies for fuel cells and water splitting process.[1-2] To improve performance these reactions, novel and appropriate catalysts are required for ORR in fuel cells and OER and HER for water splitting. During past few decades, tremendous efforts have been reported to develop novel metal-based nanomaterials such as platinum (Pt), palladium (Pd), and iridium (Ir) for electrochemical reactions. However, metal-based catalysts have severe limitations such as poor stability, gas poisoning effect, and environmentally toxicity. Moreover, limited resources and high cost of noble metals make hard to commercialized applications. These limitations have increased an interest about metal-free electrocatalysts, especially carbon-based materials. In 2009, Dai *et al.* discovered a new type of electrocatalysts based on heteroatom-doped carbon nanomaterials as an effective, low-cost, metal-free alternative to platinum (Pt) for ORR.[3] Since then, tremendous researches have been geared to utilize carbon-based electrocatalysts for various applications.[4-7]

5.1.2. Electro-Reforming of Biomass

Water splitting is an ideal process to produce hydrogen without any byproducts. However, it requires huge electro-energy to overcome energy barrier of anodic reaction, OER. Generally, OER needs an applied voltage more than 1.23 V to provide the thermodynamic driving force. In practice,

the electrolysis potential usually requires 1.6 and 2 V to get electrolysis current densities in the range of 1–2.0 A/cm^2.[8-9] Alternatively, several researches have been proposed to replace anodic OER to more easily oxidizable molecules such as methanol,[10] ethanol,[11-13] ammonia,[14-15] and urea,[16] which are referred as electrochemical reforming or electro-reforming. Since it has lower overpotential, therefore, hydrogen evolution is much more favorable when compared to water electrolysis. In addition, since O_2 is valueless products after electrolysis, it is more beneficial to generate value-added chemicals after the anodic reaction.

Among easily oxidizable substrates, 5-hydroxymethylfurfural (HMF) has been classified as the top biomass-derived building block chemicals to produce valuable products.[17-18] HMF has two distinct functional groups including hydroxyl and carboxylic acid group, and they can be converted into various forms with oxidation, hydrogenation, reduction, or condensation reaction. For example, 2,5-furandicarboxylic acid (FDCA), one of the products from HMF oxidation, is regarded as an important monomer to synthesize a renewable polymer, poly(ethylene furanoate) in place of petroleum-derived poly(ethylene terephthalate).[17]

5.1.3. Nanoarchitectonics

In order to satisfy the worldwide demands for efficient usage of materials and resources with proper applications, scientific efforts regarding synthesis of molecules of materials, fabrication of devices, or biological treatments have been continuously required. One of important keys for these efforts is precise control of structures and organization in nanoscale level to make efficient flows, and conversion of materials and energies.

In addition to developing new materials, a novel concept to fabricate architectures of functional materials and systems has been proposed as a nanoarchitectonics concept, which was initiated by Masakazu Aono.[18] In addition to self-assembly processes, the nanoarchitectonics includes chemical synthesis, manipulation of atom/molecules, and field-induced materials control. However, fabrication of functional architectures in three-dimensional direction is not always easy. Direction-fixed construction of functional materials such as layer-by-layer (LbL) assembly with various components is a realistic starting step to demonstrate nanoarchitectonics. LbL assembly is one of the versatile methods among nanoarchitectonics to fabricate multilayer electrodes. It is easily controlled with nano-scale level, moreover, desired functional materials can be hybridized within established films. For these reasons, LbL assembly is versatile technique to demonstrate the relationships between nanostructures of electrodes and catalytic performance.

In this thesis, we designed and fabricated diverse form of functional carbon-based materials and verified the correlation between nanoarchitectures of fabricated composites and their electrocatalytic activity.

5.1.4. References

(1) Symes, M. D.; Cronin, L., Decoupling Hydrogen and Oxygen Evolution During Electrolytic Water Splitting Using an Electron-Coupled-Proton Buffer. *Nat. Chem.* **2013,** *5*, 403-409.

(2) Joya, K. S.; Joya, Y. F.; Ocakoglu, K.; van de Krol, R., Water-Splitting Catalysis and Solar Fuel Devices: Artificial Leaves on the Move. *Angew. Chem. Int. Ed.* **2013,** *52*, 10426-10437.

(3) Gong, K.; Du, F.; Xia, Z.; Durstock, M.; Dai, L., Nitrogen-Doped Carbon Nanotube Arrays with High Electrocatalytic Activity for Oxygen Reduction. *Science* **2009,** *323*, 760-764.

(4) Liu, X.; Dai, L., Carbon-Based Metal-Free Catalysts. *Nat. Rev. Mater.* **2016,** *1*, 16064.

(5) Zheng, Y.; Jiao, Y.; Zhu, Y.; Li, L. H.; Han, Y.; Chen, Y.; Du, A.; Jaroniec, M.; Qiao, S. Z., Hydrogen Evolution by a Metal-Free Electrocatalyst. *Nat. Commun.* **2014,** *5*, 3783.

(6) Qu, L.; Liu, Y.; Baek, J.-B.; Dai, L., Nitrogen-Doped Graphene as Efficient Metal-Free Electrocatalyst for Oxygen Reduction in Fuel Cells. *ACS Nano* **2010,** *4*, 1321-1326.

(7) Wang, S.; Zhang, L.; Xia, Z.; Roy, A.; Chang, D. W.; Baek, J.-B.; Dai, L., Bcn Graphene as Efficient Metal-Free Electrocatalyst for the Oxygen Reduction Reaction. *Angew. Chem. Int. Ed.* **2012,** *51*, 4209-4212.

(8) Carmo, M.; Fritz, D. L.; Mergel, J.; Stolten, D., A Comprehensive Review on PEM Water Electrolysis. *Int. J. Hydrog. Energy* **2013,** *38*, 4901-4934.

(9) Pagliaro, M. V.; Bellini, M.; Bevilacqua, M.; Filippi, J.; Folliero, M. G.; Marchionni, A.; Miller, H. A.; Oberhauser, W.; Caporali, S.; Innocenti, M.; Vizza, F., Carbon Supported Rh Nanoparticles for the Production of Hydrogen and Chemicals by the Electroreforming of Biomass-Derived Alcohols. *RSC Adv.* **2017,** *7*, 13971-13978.

(10) Take, T.; Tsurutani, K.; Umeda, M., Hydrogen Production by Methanol–Water Solution Electrolysis. *J. Power Sources* **2007,** *164*, 9-16.

(11) Lamy, C.; Jaubert, T.; Baranton, S.; Coutanceau, C., Clean Hydrogen Generation through the Electrocatalytic Oxidation of Ethanol in a Proton Exchange Membrane Electrolysis Cell (PEMEC): Effect of the Nature and Structure of the Catalytic Anode. *J. Power Sources* **2014,** *245*, 927-936.

(12) Bambagioni, V.; Bevilacqua, M.; Bianchini, C.; Filippi, J.; Lavacchi, A.; Marchionni, A.; Vizza, F.; Shen, P. K., Self-Sustainable Production of Hydrogen, Chemicals, and Energy from Renewable Alcohols by Electrocatalysis. *ChemSusChem* **2010,** *3*, 851-855.

(13) Chen, Y. X.; Lavacchi, A.; Miller, H. A.; Bevilacqua, M.; Filippi, J.; Innocenti, M.; Marchionni, A.; Oberhauser, W.; Wang, L.; Vizza, F., Nanotechnology Makes Biomass Electrolysis More Energy Efficient Than Water Electrolysis. *Nat. Commun.* **2014,** *5*, 4036.

(14) Schalenbach, M.; Carmo, M.; Fritz, D. L.; Mergel, J.; Stolten, D., Pressurized PEM Water Electrolysis: Efficiency And Gas Crossover. *Int. J. Hydrog. Energy* **2013,** *38*, 14921-14933.

(15) Vitse, F.; Cooper, M.; Botte, G. G., On the Use of Ammonia Electrolysis for Hydrogen Production. *J. Power Sources* **2005,** *142*, 18-26.

(16) Yan, W.; Wang, D.; Botte, G. G., Electrochemical Decomposition of Urea with Ni-Based Catalysts. *Appl. Catal. B* **2012,** *127*, 221-226.

(17) van Putten, R.-J.; van der Waal, J. C.; de Jong, E.; Rasrendra, C. B.; Heeres, H. J.; de Vries, J. G., Hydroxymethylfurfural, a Versatile Platform Chemical Made from Renewable Resources. *Chem. Rev.* **2013,** *113*, 1499-1597.

(18) Bozell, J. J.; Petersen, G. R., Technology Development for the Production of Biobased Products from Biorefinery Carbohydrates—the Us Department of Energy's "Top 10" Revisited. *Green chem.* **2010,** *12*, 539-554.

5.2. Covalent Functionalization Based Heteroatom Doped Graphene Nanosheet for Oxygen Reduction Reaction

5.2.1. Abstract

Oxygen reduction reaction (ORR) is an important reaction in energy conversion systems such as fuel cells and metal-air batteries. Carbon nanomaterials doped with heteroatoms are highly attractive materials for use as electrocatalysts by virtue of their excellent electrocatalytic activity, high conductivity, and large surface area. This study reports the synthesis of highly efficient electrocatalysts based on heteroatom-doped graphene nanosheets prepared through covalent functionalization using various small organic molecules and a subsequent thermal treatment. A series of nitrogen-doped reduced graphene oxide (NRGO*n*) nanosheets exhibited varying degrees and configurations of nitrogen atoms within the graphitic framework depending on the type of precursors used. On the basis of the rotating disk electrode (RDE) and rotating ring-disk electrode (RRDE) experiments, NRGO3, with a high degree of pyridinic-N content, displayed the desired one-step, quasi-four-electron transfer pathway during ORR, similar to commercial Pt/C. We also demonstrated the potential of covalent functionalization of sulfur and boron-doped graphene nanosheets.

---

[*] Chapter 5.2 is reproduced in part with permission from Park, M.; Lee, T.; Kim, B.-S., *Nanoscale* **2013,** *5*, 12255-12260. Copyright 2013 The Royal Society of Chemistry.

5.2.2. Introduction

Due to the rising energy demands and limited resources of fossil fuels, fuel cells have considerably attracted with their remarkable energy density and environmental benignity.[1-5] Despite their promising advantages, it is still desirable to improve performance and develop cost-effective electrocatalysts for a key reaction in fuel cells, the oxygen reduction reaction (ORR). As a result, electrocatalysts for ORR play an important role in converting oxygen as an energy source and thus determining electrochemical performance of the devices.[3, 6] Traditionally, platinum (Pt) and its alloys have been utilized as ORR catalysts owing to their excellent catalytic efficiency, low overpotential, and high current density.[7-9] However, they have still suffered from multiple limiting factors, regarding poor stability, intermediate tolerance, and anode crossover. Moreover, high cost and limited reserves of Pt make hard to use in large-scale applications.[10-14] Therefore, recent efforts have been geared toward developing alternative electrocatalysts based on non-precious metals or metal-free carbon-based nanomaterials. Among them, graphene, a single layer of two-dimensional aromatic carbon lattice, represents outstanding chemical, electrical, and mechanical properties, which are favorable in the harsh ORR environment.[15-17]

Recently, heteroatom-incorporated graphene including nitrogen (N), boron (B), sulfur (S), and phosphorus (P) has exhibited excellent electrocatalytic performance toward ORR.[18-22] This heteroatom doping not only enhances the electrical properties of graphene, but also effectively affords the active site on to the surface of graphene with a charge polarization effect.[23] In general, N-doped graphene is commonly prepared by several methods such as chemical vapor deposition and thermal annealing in the presence of nitrogen-containing precursors such as small molecules (melamine, pyridine), or polymers, and nitrogen-plasma treatments of graphene.[13, 24-30] Although these approaches successfully introduce nitrogen atoms within the graphene lattice, they require toxic chemical precursors, are unable to control the degree of doping and type of nitrogen functionality, or are limited to doping of nitrogen atoms only.

Herein, we propose a unique design of heteroatom-doped graphene nanosheets prepared by the covalent functionalization of diverse small molecules with a subsequent annealing process. The covalent functionalization chemistry is based on the N-ethyl-N'-(3-dimethyl aminopropyl) carbodiimide methiodide (EDC)-mediated reaction between the carboxylic acid groups of graphene oxide (GO) nanosheets and the excess amine moiety in the small molecules.[31-32] The prepared heteroatom-doped graphene nanosheets represented good electrocatalytic activity toward ORR through an efficient one-step, four-electron pathway similar to commercial Pt/C catalysts; this could be attributed to the charge polarization of the carbon network induced by heteroatoms. As a proof of concept, we employed five different types of amines which have different amine densities for preparing N-doped reduced graphene oxide (NGO*n*, *n* = number of amine groups) nanosheets (**Figure 5.1**). We demonstrate how the electrochemical performance can be controlled by varying the degree

and configurations of the nitrogen dopant. In addition, our approach could be successfully extended toward the introduction of other heteroatoms such as B and S into the graphene nanosheet.

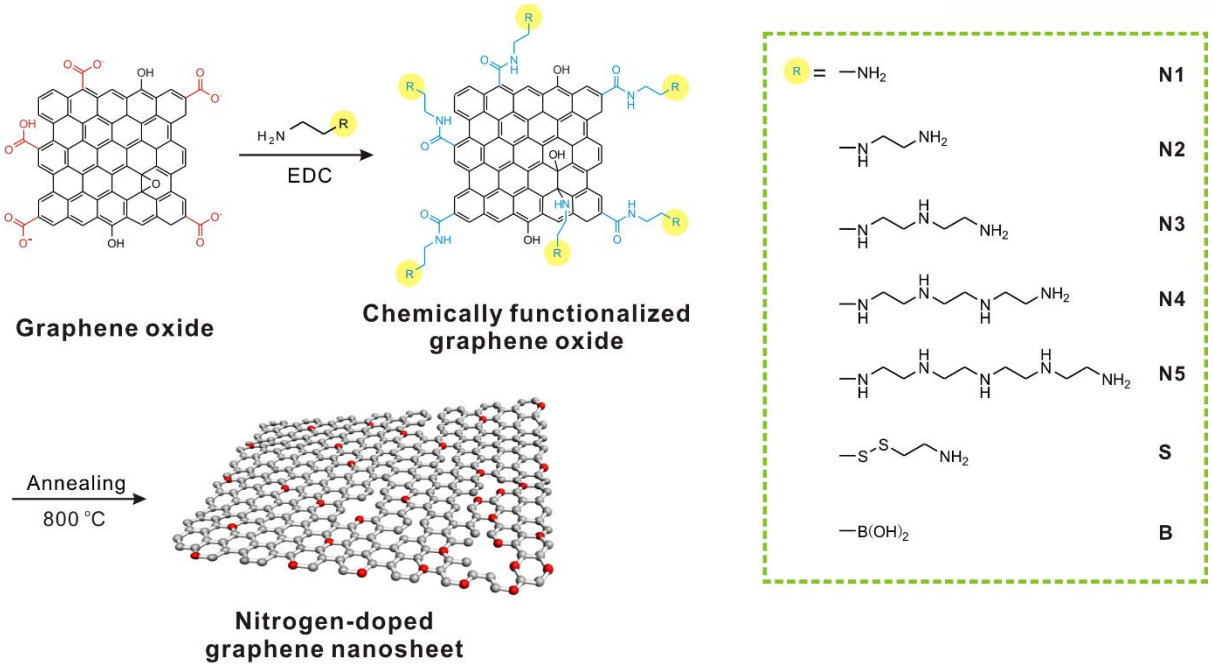

Figure 5.1. Schematic representation of the chemical functionalization of graphene nanosheets with various molecules.

5.2.3 Experimental

5.2.3.1. Preparation of Graphene Oxide (GO) Suspension and Covalent Surface Modification

Initially, graphite oxide powder was prepared from graphite powder (Aldrich, <20 μm) by the modified Hummers method and exfoliated to give a brown dispersion of graphene oxide (GO) under ultrasonication (typical conc. of 0.50 mg mL^{-1}). For the surface functionalization, 50 mL of the GO suspension was reacted with 4 mL of various amines (ethylene diamine, diethylene triamine, triethylene tetramine, tetraethylene pentamine, and pentaethylene hexamine) in the presence of 0.50 g of N-ethyl-N'-(3-dimethyl aminopropyl)carbodiimide methiodide (EDC) for 12 h at room temperature, followed by an extensive dialysis (SpectraPore MWCO 12 – 14K) for 3 days to remove any byproducts and excess reactants. These suspensions were denoted by amine-functionalized graphene oxide (NGO*n*).

5.2.3.2. Preparation of Nitrogen-Doped Graphene Oxide (NRGO) and Thermally Reduced Graphene Oxide (TRGO)

The NGO*n* suspensions were freeze dried to remove water and annealed at 800 °C for 1 h under Ar atmosphere to afford nitrogen-doped graphene oxide (NRGO*n*) powder. Thermally reduced graphene oxide (TRGO) was prepared by annealing GO powder under identical conditions.

5.2.3.3. Preparation of Catalyst Ink for the Rotating Disk Electrode

Each NRGO*n* powder was first dispersed in a solvent mixture (water: Nafion = 9:1 v/v) at a concentration of 1.0 mg mL^{-1} with a brief sonication for 40 min to obtain homogeneous dispersions. Then 5 μL of each suspension was dropped on a 3 mm diameter glassy carbon electrode embedded in Teflon as a working electrode. Finally, ink was dried in the vacuum condition for 10 min forming a thin film on the glassy carbon electrode.

5.2.3.4. Rotating Disk Electrode (RDE) Experiment

For the electrocatalytic evaluation of NRGO*n*, we performed the rotating disk electrode (RDE) at room temperature by linear sweep voltammograms (LSVs). An as-prepared glassy carbon electrode was used as a working electrode, Pt was used as a counter electrode and saturated calomel electrode (SCE) was used as a reference electrode. RDE measurements were carried out in a 0.1 M KOH electrolyte in the potential range from 0 V to -0.8 V at a scan rate of 10 mV s^{-1} and measured at 900, 1600, 2500, and 3200 rpm. Oxygen was purged into the electrolyte to make an O_2-saturated solution. The Koutecky-Levich (K-L) equation was used to calculate the number of electrons transferred with RDE data.

5.2.3.5. Rotating Ring-Disk Electrode (RRDE) Experiment

The RRDE experiments were measured with a 10 mV s^{-1} scan rate from 0 V to -0.8 V and the oxidation potential of ring-disk was set to 0.2 V. Electron transfer number (*n*) and peroxide yield (%) was calculated by the following equations:

$$HO_2^-(\%) = 200\frac{\frac{I_r}{N}}{I_d + \frac{I_r}{N}} \quad (1)$$

$$n = 4\frac{I_d}{I_d + \frac{I_r}{N}} \quad (2)$$

where I_r and I_d are the ring current, and the disk current, respectively.

5.2.3.6. Characterizations

UV/vis spectroscopy (Shimadzu UV-1800) and the ζ-potential of colloidal suspensions were measured using a zeta potential analyzer (Malvern, Zetasizer nano-zs). The surface morphology of the GO and NGO was examined using an atomic force microscope (AFM, Dimension D3100, Veeco), and we used a silicon wafer as a substrate to obtain AFM image of NGO3 graphene nanosheets before thermal annealing. X-ray photoelectron spectroscopy (XPS, Thermo Fisher, K-alpha) was used to detect elemental composition and the chemical state of the NRGO suspensions. Electrochemical performance for ORR was performed with the rotating disk electrode (RDE) and rotating ring-disk electrode (RRDE; ALS Co., Ltd).

5.2.4. Results and Discussion

As a first step, the GO suspension was prepared by the modified Hummers method starting from a graphite powder.[33] Following sonication step to exfoliate graphite oxide to graphene oxide, the oxygen-containing functional groups are introduced on the surface of the graphene nanosheet, such as carboxylic acids and alcohol groups. They rendered the GO suspension negatively charged over a wide range of pH conditions (ζ-potential of -40 mV). As a model system, we used five different amine molecules as follows: ethylene diamine, diethylene triamine, triethylene tetramine, tetraethylene pentamine, and pentaethylene hexamine (**Figure 5.1**). In order to introduce these various amine molecules, we employed the EDC-mediated functionalization of graphene nanosheets through the reaction between carboxylic acids and amine molecules. It should be noted that we could not prevent the direct ring opening reaction of epoxides, which were present on the basal plane of GO nanosheets, with excess amine groups; nonetheless, this functionalization route also contributed to the successful introduction of amine moieties on the GO nanosheet.[31-32]

The successful functionalization of various amine molecules afforded a series of positively charged GO with varying numbers of amine groups (NGO1–NGO5). They exhibited good colloidal stability for several months without any aggregations. To verify suspension stability and amine-incorporation, zeta-potential measurements clearly demonstrated the successful surface functionalization of GO, whose surface charge reversed from negative (-40 mV at neutral conditions) to positive upon functionalization with amine moieties that ranged from 41.7–52.0 mV at pH 2, 41.4–47.0 mV at pH 7, and 30.4–38.1 mV at pH 11 from NGO1 to NGO5 (**Figure 5.3**(b)). It is interesting that the zeta-potential values of all samples decreased with an increase of pH. It means there are weakly charged amine moieties on to the NGO nanosheets and their charge densities are highly dependent on the external pH conditions. Moreover, we noticed that the color of the GO suspension changed to a dark brown after functionalizing with amine moieties.[34-35] It implies GO was slightly reduced by coupling with amine molecules.

Atomic force microscopy (AFM) images in **Figure 5.4** and **Figure 5.5** demonstrated that the prepared GO nanosheets were mainly composed of a monolayer of graphene nanosheets with an average thickness of 0.90 ± 0.03 nm and a lateral dimension of 1.01 ± 0.19 μm. One of the representative example, the NGO3 showed that the graphene nanosheets possessed a higher average thickness of 1.26 ± 0.04 nm without noticeable changes in the lateral dimension of graphene nanosheets of 1.01 ± 0.46 μm.[36-37] This observation reflects the presence of long-chain triethylene tetramine on both sides of the GO nanosheets after functionalization. In addition, it highlights the mild nature of this synthetic condition that does not alter the intrinsic properties related to the dimensions of the graphene nanosheet.

The prepared NGO*n* catalysts were thermally annealed at 800 °C for 1 h under Ar atmosphere. The resulting products were defined as N-doped reduced GO nanosheets (NRGO*n*)

according to the respective amine precursors. Herein, we propose that the degree of nitrogen content in the precursor affects the degree of doped-nitrogen and its configuration in the NRGO*n*. The thermal annealing caused atomic rearrangement leading to a highly ordered graphitic structure and the simultaneous incorporation of nitrogen atoms from the functionalized amine groups into the graphene lattice.[38] The successful incorporation and the nature of N-doping on the graphene nanosheets were verified by X-ray photoelectron spectroscopy (XPS) (**Figure 5.6**). From the XPS survey spectra, we found a distinct nitrogen peak in all NRGO*n* samples, which was absent in the GO nanosheets annealed under identical conditions (i.e. thermally reduced GO (TRGO)). The deconvoluted high-resolution N1s XPS spectra further elucidated four different types of nitrogen configurations on the graphene nanosheets corresponding to pyridinic-N (N-6, 398.1 eV), pyrrolic-N (N-5, 399.8 eV), graphitic-N (N-Q, 401.2 eV) and N-oxide (N-O, 403.1 eV) from NRGO*n* (**Table 5.1**). In accordance with the nitrogen content in the initial amine precursors, the amount of doped nitrogen was gradually increased from NRGO1 (0.72%) to NRGO5 (4.3%). It is worth mentioning that the relative fractions of N-configurations were different depending on the amine precursors used (**Table 5.2**). According to previous researches, it has been known that pyridinic-N is the most efficient bonding structure among nitrogen configurations to improve ORR activity in graphene. In our study, NRGO3 has the most abundant pyridinic-N functionality despite its relatively lower N-content.

To explore the electrocatalytic activity during the ORR process of NRGO*n* catalysts, we investigated the rotating disk electrode (RDE) voltammograms in an O_2-saturated 0.10 M KOH aqueous solution (**Figure 5.7** and **Figure 5.8**). As a control experiment, undoped TRGO was employed to verify the importance of N-doping for an efficient ORR. **Figure 5.7**(a) indicates a series of linear sweep voltammograms at a constant rotating rate of 2500 rpm and quantitative evaluation in terms of the onset potential and kinetic limiting current density based on the RDE measurements. The electron transfer number (*n*) of each catalyst was also calculated during the ORR process from the RDE results based on the Koutecky-Levich (K–L) equation.[39-40] All NRGO*n* catalysts displayed considerably enhanced electrocatalytic activity for ORR rather than undoped TRGO, which showed a dominant two-step, two-electron ORR pathway. Among all NRGO*n* catalysts, NRGO3 represented the best catalytic performance for ORR with the most positive onset potential at -0.15 V (*vs.* SCE) and the highest limiting current density of -4.55 mA cm^{-2}. Moreover, the electron transfer number of NRGO3 determined from the K-L plot reached 3.63, indicating an efficient four-electron ORR pathway similar to that of commercial Pt/C catalysts.[41-42] The pyridinic-N sites have been widely recognized as catalytic active sites for ORR because delocalization of the π-electrons from pyridinic-N.[43] XPS measurements provided additional support to the theory that highly catalytic carbon materials usually retain a large amount of pyridinic-N.[20, 44] Thus, it is proposed that the enhanced catalytic activity of NRGO3 originates from the higher fraction of pyridinic-N rather than the absolute amount of N-doping of the graphene nanosheets (i.e., 43.2% of NRGO3 *vs* 32.0% of NRGO4 *vs* 38.9%

of NRGO5).

To further identify the ORR activity with the optimized NRGO3 catalyst in comparison with those of undoped TRGO and commercial Pt/C catalysts, rotating ring-disk electrode (RRDE) measurements were carried out to monitor the formation of hydrogen peroxide species (HO_2^-) during the ORR process (**Figure 5.7**(c) and (d)). The RRDE measurements showed that NRGO3 exhibited a higher disk current (oxygen reduction) and a smaller ring current (peroxide oxidation) than the undoped TRGO catalyst. The calculated electron transfer number (*n*) was around 3.45 and peroxide yield was around 28% from -0.3 to -0.8 V, while TRGO showed that the electron number (*n*) was around 3.12 and peroxide yield was about 44% at the identical potential range. This result is consistent with that obtained from the K-L plot based on the RDE measurements, suggesting the NRGO3 catalyst can undergo a one-step, direct four-electron ORR pathway with a relatively low yield of the peroxide intermediate. Although the catalytic performance of NRGO3 is still inferior to that of commercial Pt/C, the former displayed a significantly enhanced durability. The chronoamperometric (CA) of NRGO3 was conducted at a constant reduction potential of -0.3 V to confirm the stability. After 10000 s, the CA responses of NRGO3 showed a slow attenuation with high current retention of 73%, which is much higher value than that of commercial Pt/C with 60% (**Figure 5.9**).

Moreover, we confirmed that our approach could be extendable toward the other heteroatoms such as boron and sulfur into the graphene nanosheet.[13, 45-46] As a molecular precursor of each doping atom, we employed 4-aminophenylboronic acid as a boron source and cystamine as a sulfur source. Interestingly, each heteroatom was successfully introduced within the graphene lattice together with the nitrogen dopant, as we employed an identical chemical functionalization process on the graphene nanosheets. High-resolution XPS shows that each heteroatom (B, S, and N) is found to be in different configurations (**Figure 5.10**).

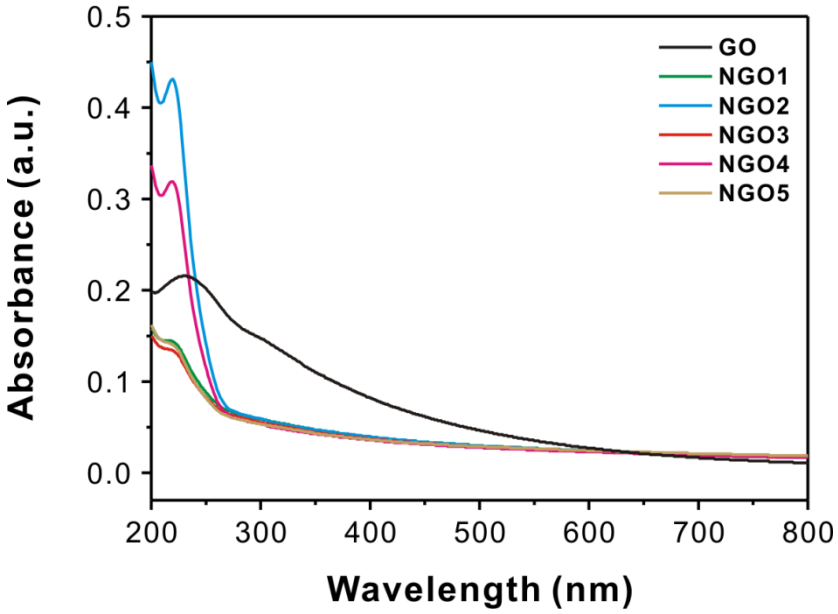

Figure 5.2. UV-vis absorbance spectra for GO suspension and NGO*n* derivatives. Concentration of suspensions is 0.5 μg mL^{-1}.

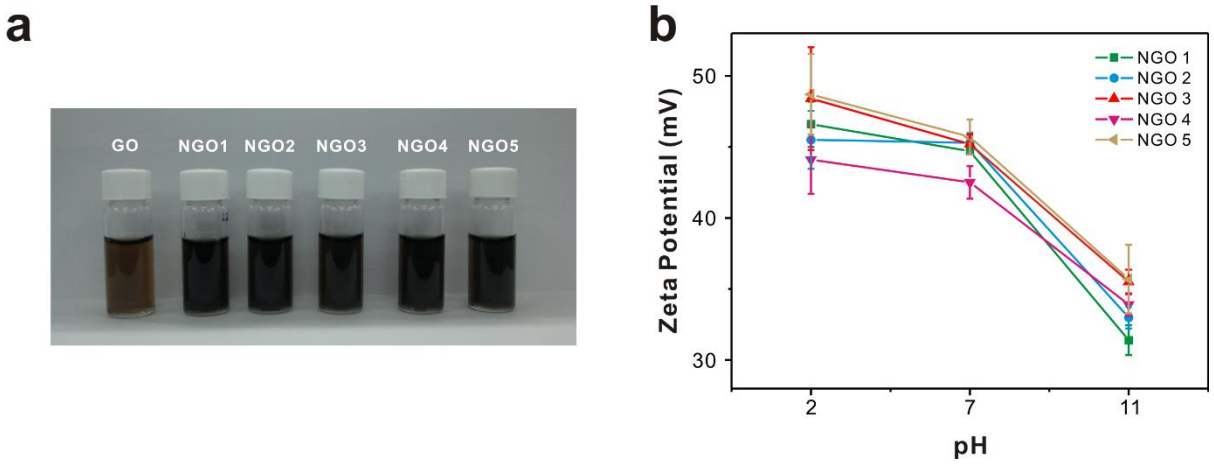

Figure 5.3. (a) Photographs of each suspension prepared in this study (conc. 0.50 mg mL^{-1}). (b) Zeta-potential for functionalized NGO*n* derivatives as a function of pH.

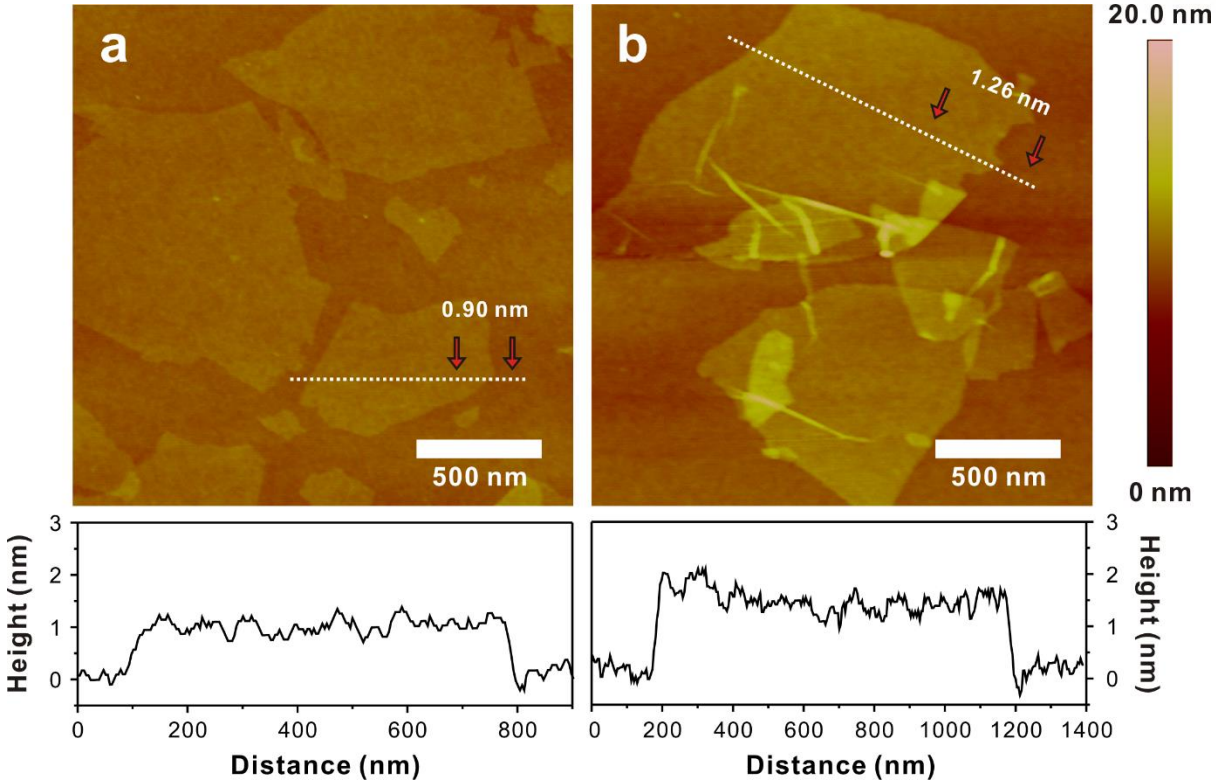

Figure 5.4. Representative height-mode AFM images of (a) GO and (b) NGO3 with the corresponding line scan profiles.

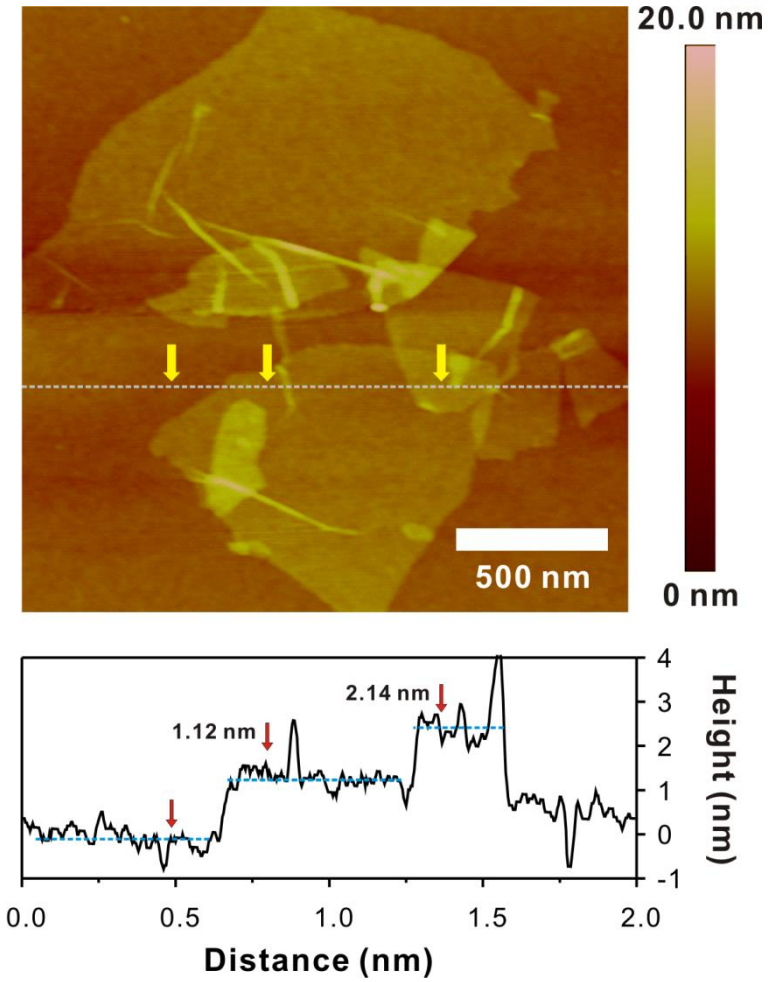

Figure 5.5. Representative height-mode AFM images of NGO3 with the corresponding line scan profiles. The height of monolayer and bilayer is about 1.12 nm and 2.14 nm, respectively.

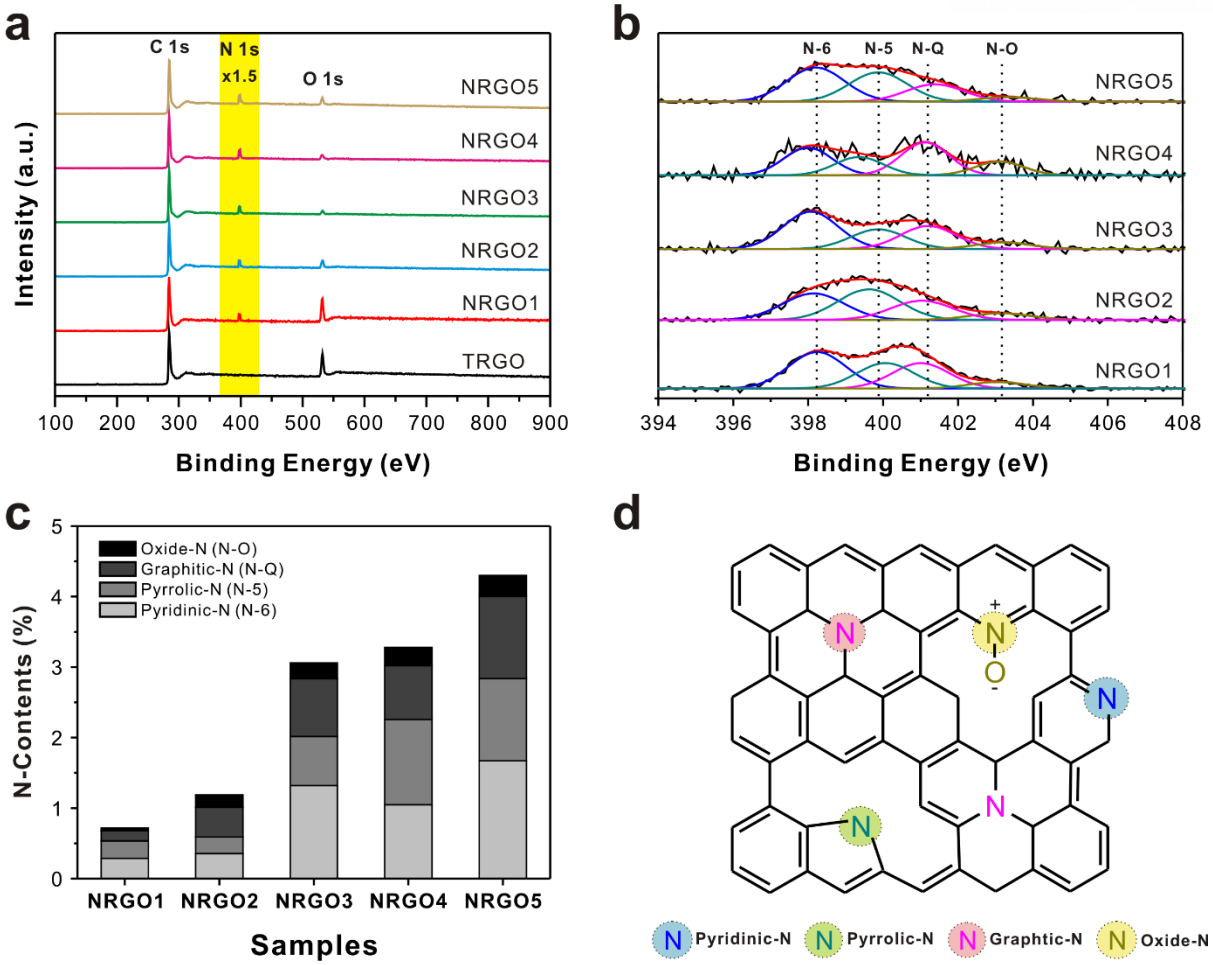

Figure 5.6. XPS survey spectra for various samples in this study. (b) Deconvoluted high-resolution XPS N1s spectra of all NRGO*n*. (c) Total N contents of NRGO*n*. (d) Schematic representation of nitrogen bonding configurations in N-doped graphene nanosheets.

Table 5.1 Relative Ratio (%) of Atomic Compositions by XPS Measurement.

	C	O	N
TRGO	84.99	15.01	ND
NRGO1	84.17	15.11	0.72
NRGO2	90.48	8.32	1.19
NRGO3	93.77	3.17	3.06
NRGO4	91.75	4.98	3.28
NRGO5	89.47	6.22	4.3

Table 5.2. Relative Ratio (%) of Nitrogen Configurations in NRGO*n* by Deconvoluted High-Resolution XPS N1s Spectra. Number in Parenthesis Represents the Binding Energy in eV.

	Pyridinic-N	Pyrrolic-N	Graphitic-N	Oxide-N
NRGO1	39.99 (398.21)	34.42 (399.87)	20.42 (401.39)	5.17 (403.04)
NRGO2	29.87 (398.00)	19.72 (399.35)	35.55 (401.12)	14.86 (403.11)
NRGO3	43.22 (398.07)	22.70 (399.87)	26.65 (401.20)	7.44 (403.21)
NRGO4	31.98 (398.15)	36.90 (399.62)	23.21 (401.03)	7.90 (403.12)
NRGO5	38.91 (398.24)	27.12 (400.07)	27.06 (401.00)	6.91 (403.05)

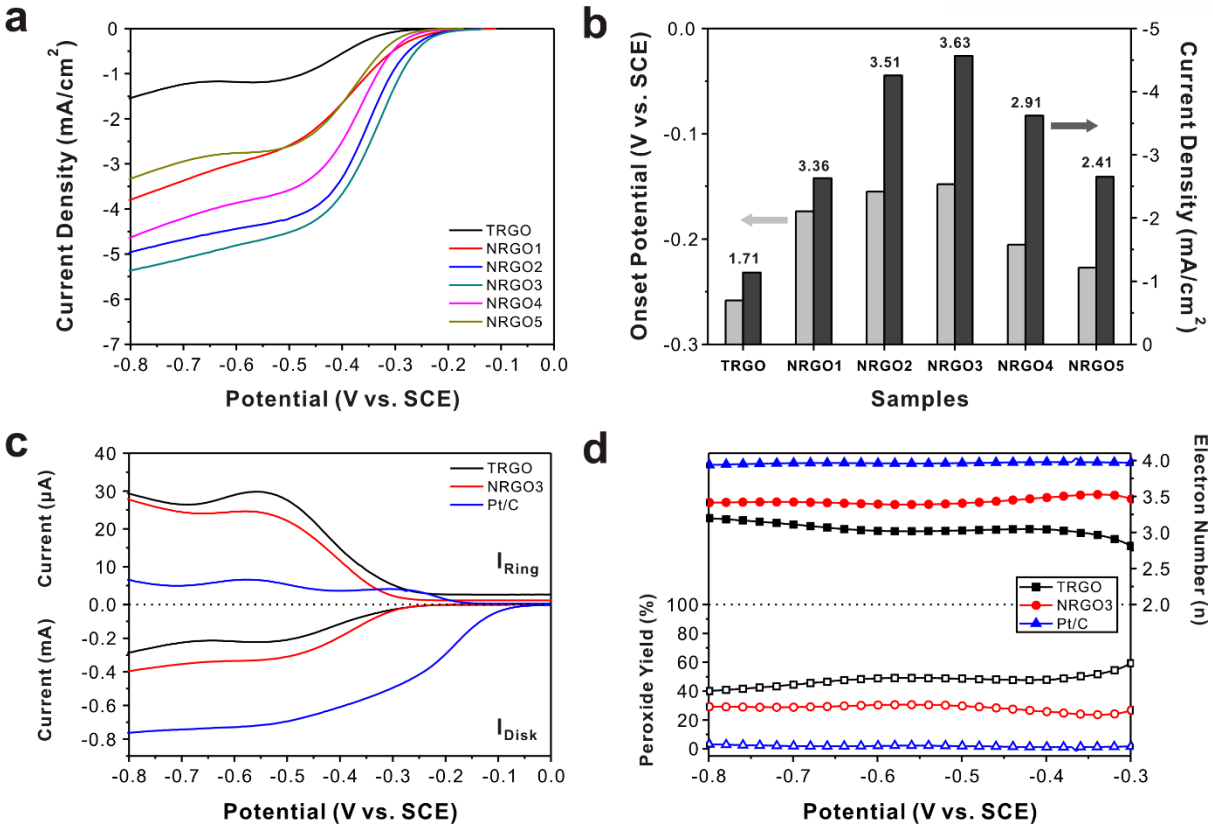

Figure 5.7. (a) Linear sweep voltammograms (LSVs) of all NRGO*n* electrocatalysts prepared in the study, including that of a control set of TRGO. RDE tests were acquired at a rotation rate of 2500 rpm and a scan rate of 10 mV s^{-1} in O_2-saturated 0.10 M KOH electrolyte solution. (b) Comparison of the onset potential (white bar) and limiting current density (black bar) of each catalyst as determined by RDE experiments. Electron transfer number (*n*) based on the Koutecky-Levich equation is located on the top of the bar graph. The onset potential and limiting current were measured at -0.02 mA cm^{-2} and -0.50 V (*vs*. SCE), respectively. (c) LSVs of RRDE experiments of TRGO, NRGO3, and commercial 20 wt% Pt/C catalysts in an O_2-saturated 0.10 M KOH aqueous solution at 3200 rpm. (d) The plot of the peroxide yields (%) and the electron transfer number (*n*) of electrocatalysts.

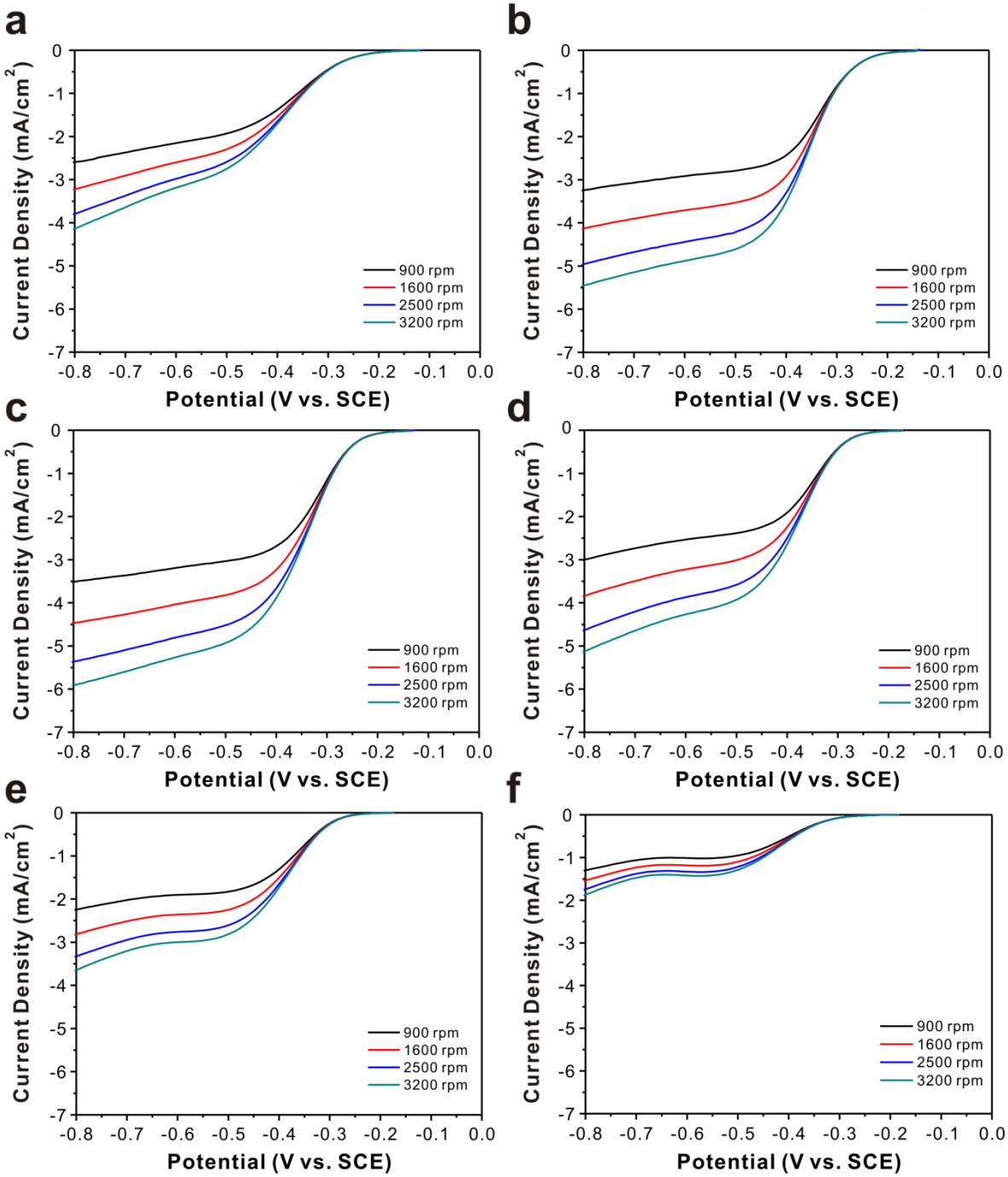

Figure 5.8. RDE measurements at 10 mV s^{-1} scan rate in O_2-saturated 0.5 M KOH electrolyte. (a) Linear Sweep Voltammograms for (a) NRGO1, (b) NRGO2, (c) NRGO3, (d) NRGO4, (e) NRGO5, and (f) TRGO at 2500 rpm.

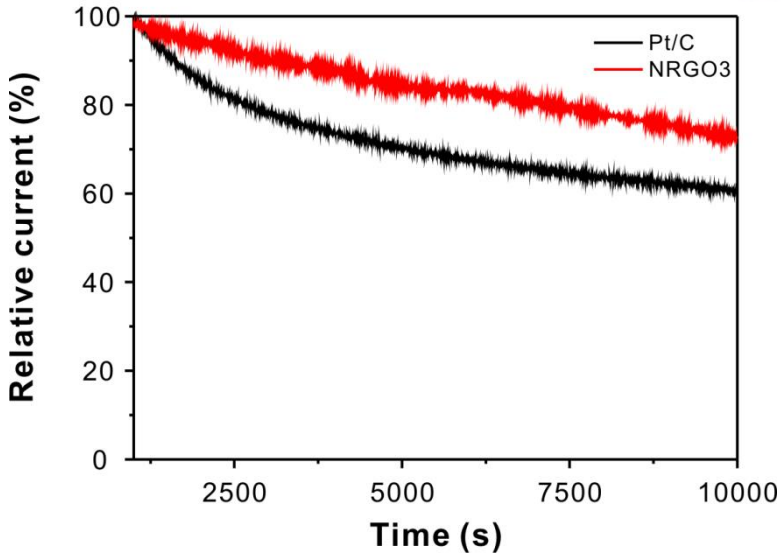

Figure 5.9. The chronoamperometric durability response for 10000 s with Pt/C and NRGO3. NRGO3 exhibited a slow attenuation with high current retention of 73%, which is higher than that of Pt/C in the O_2-saturated 0.1 M KOH solution at -0.25 V (*vs.* SCE) with 1600 rpm.

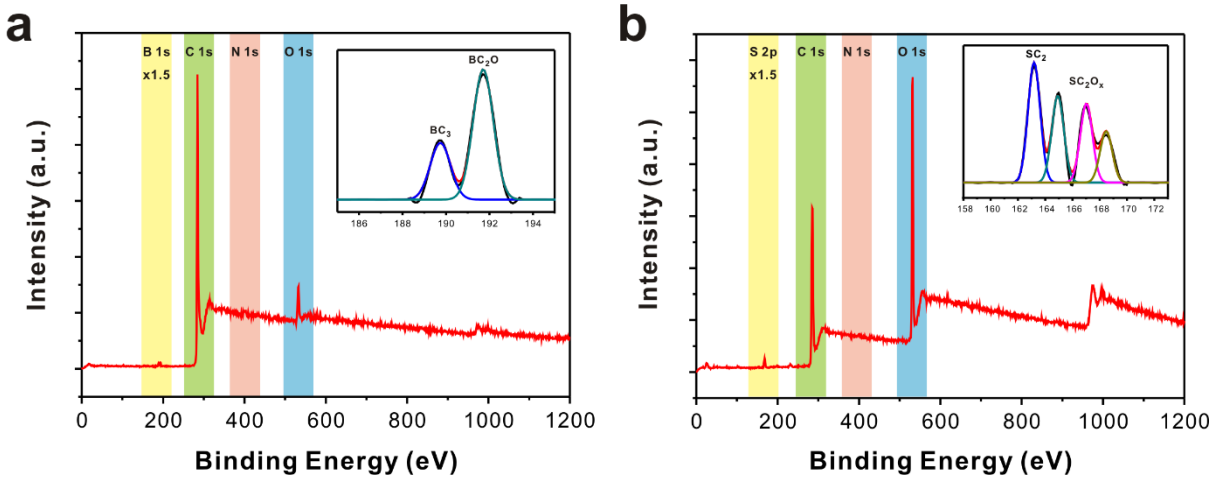

Figure 5.10. XPS survey spectra of (a) B-doped and (b) S-doped graphene nanosheets with corresponding deconvoluted high-resolution B1s and S2p spectra in the inset, respectively.

5.2.5. Conclusion

In summary, we develop a simple and facile approach for chemical functionalization toward heteroatom-doped graphene nanosheets with small organic molecules as the electrocatalysts for the oxygen reduction reaction. The prepared heteroatom-doped graphene nanosheet exhibited a good electrocatalytic activity rather than undoped counterpart (TRGO) through an efficient one-step, four-electron pathway comparable to commercial Pt/C catalyst. Due to the charge polarization of the carbon network induced by the doped heteroatoms, oxygen molecules can be easily interacted with heteroatom-doped graphene nanosheets. Although NRGO*n* catalysts represent lower catalytic activity than that of commercial Pt/C, it is worth noting that we fabricate metal-free carbon-based nanomaterials. Moreover, this approach has also been successfully extendable to other heteroatoms such as boron and sulfur on the graphene nanosheets. By taking advantage of the facile synthesis process, we anticipate that this covalent functionalization would afford other routes for the controlled introduction of heteroatoms on the graphene nanosheets for various applications.

5.2.6. References

(1) Tarascon, J. M.; Armand, M., Issues and Challenges Facing Rechargeable Lithium Batteries. *Nature* **2001,** *414*, 359-367.

(2) Girishkumar, G.; McCloskey, B.; Luntz, A. C.; Swanson, S.; Wilcke, W., Lithium−Air Battery: Promise and Challenges. *J. Phys. Chem. Lett.* **2010,** *1*, 2193-2203.

(3) Steele, B. C. H.; Heinzel, A., Materials for Fuel-Cell Technologies. *Nature* **2001,** *414*, 345-352.

(4) Park, S.; Vohs, J. M.; Gorte, R. J., Direct Oxidation of Hydrocarbons in a Solid-Oxide Fuel Cell. *Nature* **2000,** *404*, 265-267.

(5) Winter, M.; Brodd, R. J., What Are Batteries, Fuel Cells, and Supercapacitors? *Chem. Rev.* **2004,** *104*, 4245-4270.

(6) Heersche, H. B.; Jarillo-Herrero, P.; Oostinga, J. B.; Vandersypen, L. M. K.; Morpurgo, A. F., Bipolar Supercurrent in Graphene. *Nature* **2007,** *446*, 56-59.

(7) Toda, T.; Igarashi, H.; Uchida, H.; Watanabe, M., Enhancement of the Electroreduction of Oxygen on Pt Alloys with Fe, Ni, and Co. *J. Electrochem. Soc.* **1999,** *146*, 3750-3756.

(8) Paulus, U. A.; Wokaun, A.; Scherer, G. G.; Schmidt, T. J.; Stamenkovic, V.; Markovic, N. M.; Ross, P. N., Oxygen Reduction on High Surface Area Pt-Based Alloy Catalysts in Comparison to Well Defined Smooth Bulk Alloy Electrodes. *Electrochim. Acta* **2002,** *47*, 3787-3798.

(9) Stamenkovic, V. R.; Fowler, B.; Mun, B. S.; Wang, G.; Ross, P. N.; Lucas, C. A.; Marković, N. M., Improved Oxygen Reduction Activity on $Pt_3Ni(111)$ Via Increased Surface Site Availability. *Science* **2007,** *315*, 493-497.

(10) Yu, X.; Ye, S., Recent Advances in Activity and Durability Enhancement of Pt/C Catalytic Cathode in PEMFC: Part II: Degradation Mechanism and Durability Enhancement of Carbon Supported Platinum Catalyst. *J. Power Sources* **2007,** *172*, 145-154.

(11) Peng, Z.; Yang, H., Synthesis and Oxygen Reduction Electrocatalytic Property of Pt-on-Pd Bimetallic Heteronanostructures. *J. Am. Chem. Soc.* **2009,** *131*, 7542-7543.

(12) de Bruijn, F. A.; Dam, V. A. T.; Janssen, G. J. M., Review: Durability and Degradation Issues of PEM Fuel Cell Components. *Fuel Cells* **2008,** *8*, 3-22.

(13) Lai, L.; Potts, J. R.; Zhan, D.; Wang, L.; Poh, C. K.; Tang, C.; Gong, H.; Shen, Z.; Lin, J.; Ruoff, R. S., Exploration of the Active Center Structure of Nitrogen-Doped Graphene-Based Catalysts for Oxygen Reduction Reaction. *Energy Environ. Sci.* **2012,** *5*, 7936-7942.

(14) Jin, Z.; Nie, H.; Yang, Z.; Zhang, J.; Liu, Z.; Xu, X.; Huang, S., Metal-Free Selenium Doped Carbon Nanotube/Graphene Networks as a Synergistically Improved Cathode Catalyst for Oxygen Reduction Reaction. *Nanoscale* **2012,** *4*, 6455-6460.

(15) Geim, A. K.; Novoselov, K. S., The Rise of Graphene. *Nat. Mater.* **2007,** *6*, 183-191.

(16) Novoselov, K. S.; Geim, A. K.; Morozov, S. V.; Jiang, D.; Katsnelson, M. I.; Grigorieva, I. V.; Dubonos, S. V.; Firsov, A. A., Two-Dimensional Gas of Massless Dirac Fermions in Graphene. *Nature*

2005, *438*, 197-200.

(17) Castro Neto, A. H.; Guinea, F.; Peres, N. M. R.; Novoselov, K. S.; Geim, A. K., The Electronic Properties of Graphene. *Rev. Mod. Phys.* **2009,** *81*, 109-162.

(18) Qu, L.; Liu, Y.; Baek, J.-B.; Dai, L., Nitrogen-Doped Graphene as Efficient Metal-Free Electrocatalyst for Oxygen Reduction in Fuel Cells. *ACS Nano* **2010,** *4*, 1321-1326.

(19) Yu, D.; Wei, L.; Jiang, W.; Wang, H.; Sun, B.; Zhang, Q.; Goh, K.; Si, R.; Chen, Y., Nitrogen Doped Holey Graphene as an Efficient Metal-Free Multifunctional Electrochemical Catalyst for Hydrazine Oxidation and Oxygen Reduction. *Nanoscale* **2013,** *5*, 3457-3464.

(20) Yang, S.; Feng, X.; Wang, X.; Müllen, K., Graphene-Based Carbon Nitride Nanosheets as Efficient Metal-Free Electrocatalysts for Oxygen Reduction Reactions. *Angew. Chem. Int. Ed.* **2011,** *50*, 5339-5343.

(21) Yang, S.; Zhi, L.; Tang, K.; Feng, X.; Maier, J.; Müllen, K., Efficient Synthesis of Heteroatom (N or S)-Doped Graphene Based on Ultrathin Graphene Oxide-Porous Silica Sheets for Oxygen Reduction Reactions. *Adv. Func. Mater.* **2012,** *22*, 3634-3640.

(22) Liu, Z.-W.; Peng, F.; Wang, H.-J.; Yu, H.; Zheng, W.-X.; Yang, J., Phosphorus-Doped Graphite Layers with High Electrocatalytic Activity for the O_2 Reduction in an Alkaline Medium. *Angew. Chem. Int. Ed.* **2011,** *50*, 3257-3261.

(23) Zhang, L.; Xia, Z., Mechanisms of Oxygen Reduction Reaction on Nitrogen-Doped Graphene for Fuel Cells. *J. Phys. Chem. C* **2011,** *115*, 11170-11176.

(24) Wei, D.; Liu, Y.; Wang, Y.; Zhang, H.; Huang, L.; Yu, G., Synthesis of N-Doped Graphene by Chemical Vapor Deposition and Its Electrical Properties. *Nano Lett.* **2009,** *9*, 1752-1758.

(25) Wang, X.; Li, X.; Zhang, L.; Yoon, Y.; Weber, P. K.; Wang, H.; Guo, J.; Dai, H., N-Doping of Graphene through Electrothermal Reactions with Ammonia. *Science* **2009,** *324*, 768-771.

(26) Sheng, Z.-H.; Shao, L.; Chen, J.-J.; Bao, W.-J.; Wang, F.-B.; Xia, X.-H., Catalyst-Free Synthesis of Nitrogen-Doped Graphene Via Thermal Annealing Graphite Oxide with Melamine and Its Excellent Electrocatalysis. *ACS Nano* **2011,** *5*, 4350-4358.

(27) Wang, Y.; Shao, Y.; Matson, D. W.; Li, J.; Lin, Y., Nitrogen-Doped Graphene and Its Application in Electrochemical Biosensing. *ACS Nano* **2010,** *4*, 1790-1798.

(28) Yan, Z.; Peng, Z.; Sun, Z.; Yao, J.; Zhu, Y.; Liu, Z.; Ajayan, P. M.; Tour, J. M., Growth of Bilayer Graphene on Insulating Substrates. *ACS Nano* **2011,** *5*, 8187-8192.

(29) Li, X.; Wang, H.; Robinson, J. T.; Sanchez, H.; Diankov, G.; Dai, H., Simultaneous Nitrogen Doping and Reduction of Graphene Oxide. *J. Am. Chem. Soc.* **2009,** *131*, 15939-15944.

(30) Lin, Y.-C.; Lin, C.-Y.; Chiu, P.-W., Controllable Graphene N-Doping with Ammonia Plasma. *Appl. Phys. Lett.* **2010,** *96*, 133110.

(31) Hwang, H.; Joo, P.; Kang, M. S.; Ahn, G.; Han, J. T.; Kim, B.-S.; Cho, J. H., Highly Tunable Charge Transport in Layer-by-Layer Assembled Graphene Transistors. *ACS Nano* **2012,** *6*, 2432-2440.

(32) Lee, D. W.; Hong, T.-K.; Kang, D.; Lee, J.; Heo, M.; Kim, J. Y.; Kim, B.-S.; Shin, H. S., Highly Controllable Transparent and Conducting Thin Films Using Layer-by-Layer Assembly of Oppositely Charged Reduced Graphene Oxides. *J. Mater. Chem.* **2011,** *21*, 3438-3442.

(33) Hummers, W. S.; Offeman, R. E., Preparation of Graphitic Oxide. *J. Am. Chem. Soc.* **1958,** *80*, 1339-1339.

(34) Stankovich, S.; Dikin, D. A.; Piner, R. D.; Kohlhaas, K. A.; Kleinhammes, A.; Jia, Y.; Wu, Y.; Nguyen, S. T.; Ruoff, R. S., Synthesis of Graphene-Based Nanosheets Via Chemical Reduction of Exfoliated Graphite Oxide. *Carbon* **2007,** *45*, 1558-1565.

(35) Stankovich, S.; Piner, R. D.; Chen, X.; Wu, N.; Nguyen, S. T.; Ruoff, R. S., Stable Aqueous Dispersions of Graphitic Nanoplatelets Via the Reduction of Exfoliated Graphite Oxide in the Presence of Poly(Sodium 4-styrenesulfonate). *J. Mater. Chem.* **2006,** *16*, 155-158.

(36) Eda, G.; Fanchini, G.; Chhowalla, M., Large-Area Ultrathin Films of Reduced Graphene Oxide as a Transparent and Flexible Electronic Material. *Nat. Nano* **2008,** *3*, 270-274.

(37) Zhou, X.; Huang, X.; Qi, X.; Wu, S.; Xue, C.; Boey, F. Y. C.; Yan, Q.; Chen, P.; Zhang, H., In Situ Synthesis of Metal Nanoparticles on Single-Layer Graphene Oxide and Reduced Graphene Oxide Surfaces. *J. Phys. Chem. C* **2009,** *113*, 10842-10846.

(38) Zhong, M.; Kim, E. K.; McGann, J. P.; Chun, S.-E.; Whitacre, J. F.; Jaroniec, M.; Matyjaszewski, K.; Kowalewski, T., Electrochemically Active Nitrogen-Enriched Nanocarbons with Well-Defined Morphology Synthesized by Pyrolysis of Self-Assembled Block Copolymer. *J. Am. Chem. Soc.* **2012,** *134*, 14846-14857.

(39) Koutecký, J.; Levich, V., The Application of the Rotating Disc Electrode to Studies of Kinetic and Catalytic Processes. *Zh. Fiz. Khim* **1958,** *32*, 1565-1575.

(40) Hu, C.; Xiao, Y.; Zhao, Y.; Chen, N.; Zhang, Z.; Cao, M.; Qu, L., Highly Nitrogen-Doped Carbon Capsules: Scalable Preparation and High-Performance Applications in Fuel Cells and Lithium Ion Batteries. *Nanoscale* **2013,** *5*, 2726-2733.

(41) Lee, K.; Zhang, L.; Lui, H.; Hui, R.; Shi, Z.; Zhang, J., Oxygen Reduction Reaction (ORR) Catalyzed by Carbon-Supported Cobalt Polypyrrole (Co-PPy/C) Electrocatalysts. *Electrochim. Acta* **2009,** *54*, 4704-4711.

(42) Geng, D.; Chen, Y.; Chen, Y.; Li, Y.; Li, R.; Sun, X.; Ye, S.; Knights, S., High Oxygen-Reduction Activity and Durability of Nitrogen-Doped Graphene. *Energy Environ. Sci.* **2011,** *4*, 760-764.

(43) Rao, C. V.; Cabrera, C. R.; Ishikawa, Y., In Search of the Active Site in Nitrogen-Doped Carbon Nanotube Electrodes for the Oxygen Reduction Reaction. *J. Phys. Chem. Lett.* **2010,** *1*, 2622-2627.

(44) Lee, K. R.; Lee, K. U.; Lee, J. W.; Ahn, B. T.; Woo, S. I., Electrochemical Oxygen Reduction on Nitrogen Doped Graphene Sheets in Acid Media. *Electrochem. Commun.* **2010,** *12*, 1052-1055.

(45) Yang, Z.; Yao, Z.; Li, G.; Fang, G.; Nie, H.; Liu, Z.; Zhou, X.; Chen, X. a.; Huang, S., Sulfur-Doped Graphene as an Efficient Metal-Free Cathode Catalyst for Oxygen Reduction. *ACS Nano* **2011,**

6, 205-211.

(46) Wu, Z.-S.; Ren, W.; Xu, L.; Li, F.; Cheng, H.-M., Doped Graphene Sheets as Anode Materials with Superhigh Rate and Large Capacity for Lithium Ion Batteries. *ACS Nano* **2011,** *5*, 5463-5471.

5.3. Architecture-Performance Relationship in Graphene-Based Multilayer Electrodes for Biomass Reforming and H_2 Production

5.3.1. Abstract

Water electrocatalytic splitting is considered as an ideal process to generate hydrogen without any byproducts. However, in the process of water splitting reaction, high overpotential is required to overcome high energy barrier by slow kinetics of oxygen evolution reaction (OER). Herein, we choose 5-hydroxymethylfurfural (HMF) oxidation reaction to replace OER in water splitting reaction, which is much thermodynamically favored reaction. Toward that end, we fabricate layer-by-layer (LbL) assembled three-dimensional (3D) hybrid electrocatalytic electrodes toward simultaneous HMF conversion and hydrogen evolution reaction (HER) to unravel the effect of electrocatalytic activity depending on their nanoarchitecture. Nanosized graphene oxide (nGO) is used as a negatively charged building block for LbL assembly to immobilize two electroactive components, positively charged Au and Pd nanoparticles (NPs). We highlight how the internal architecture of LbL multilayer electrodes can be precisely controlled and affect their electrocatalytic performance by the nanoarchitecture of the electrode including the thickness and the position of each metal NP within 3D multilayer films. Even with the identical composition of constituent NPs, they represent a highly tunable electrocatalytic performance depending on the reaction kinetics as well as diffusion-controlled process by sequential oxidation reactions of HMF and HER. Furthermore, bifunctional two-electrode electrolyzer coupled on both anodic HMF oxidation and cathodic HER, which was optimized LbL-assembled films for each reaction, could further represent outstanding electrocatalytic activity.

5.3.2. Introduction

The critical concerns of global energy demand and climate change issues have motivated considerable efforts to develop alternative energy.[1-2] As a green energy carrier, hydrogen is anticipated to play a significant role in a future sustainable energy. However, most of hydrogen is conventionally produced through the Ni-catalyzed conversion of CH_4 to H_2, in which inevitably producing greenhouse gases such as CO and CO_2.[3] Therefore, water splitting is considered as an ideal process to generate hydrogen without any byproducts.[4-5] However, in the process of water splitting reaction, high overpotential is required to overcome the high energy barrier. Generally, the overall reaction kinetics is limited by the anodic oxygen evolution reaction (OER) due to the sluggish four-electron transfer reaction in water oxidation, comparing to the cathodic hydrogen evolution reaction (HER). OER requires an applied voltage of at least 1.23 V to provide the thermodynamic driving force. Because of the practical overpotentials associated with the reaction kinetics, a substantially larger voltage, typically in the operating voltage of 1.8 to 2.0 V is generally required.[6-7] Thus, the production cost is not competitive with the commercial production from natural gas due to the high overpotential encountered in water electrolysis. Furthermore, the co-existence of H_2 and O_2 gases, which might lead to the formation of explosive H_2/O_2 mixture, requires additional gas separation systems.[8]

Alternatively, recent efforts are geared to replace anodic OER to more easily oxidizable molecules such as methanol, ethanol, ammonia, and urea, which are referred as electrochemical reforming.[9-13] There are several requirements to replace OER in water splitting reaction. First, it should occur with a faster kinetics than that of OER or with more favorable energetics when coupled to HER. Second, the product of replaced reaction would yield a high value chemical than oxygen. Third, the reacting substrate must demonstrate a high solubility in aqueous solution in order to enable concurrent H_2 production.

Since these requirements highlight the need to find a new substrate, we choose 5-hydroxymethylfurfural (HMF) oxidation reaction to replace OER. HMF has been classified as the top biomass-derived building block chemicals to produce valuable products; for example, 2,5-furandicarboxylic acid (FDCA), one of the products from HMF oxidation, is regarded as an important monomer to synthesize a renewable polymer, poly(ethylene furanoate) in place of petroleum-derived poly(ethylene terephthalate).[1, 14-15] Although there are several ways to selectively oxidize HMF to FDCA through organic chemical reactions, they often require harsh reaction environment such as high temperature (>100 °C) under high-pressure O_2 (0.3‑2.4 MPa).[16-19] Therefore, it would be highly desirable to develop efficient methods that use mild conditions and novel catalysts to produce FDCA.

Electrocatalytic HMF oxidation has received attention as a promising sustainable strategy because it can be performed under ambient conditions without involving any toxic chemicals.[19-21] For example, Li group has reported Au/Pd alloy nanoparticles (NPs) to oxidize HMF to FDCA.[22] The Au/Pd alloy NPs demonstrated the better electrocatalytic performance than that of individual NPs for

producing FDCA. A more recent study by Sun and coworkers integrated HMF oxidation and H_2 generation from water splitting with excellent catalytic performance of Ni-based catalysts.[23-26] Although they represented an outstanding activity, these previous researches have only focused on developing new materials to enhance the electrocatalytic performance and thus far the structure of the electrode has not been a subject of intensive investigation. In order to further advance the translation of outstanding individual material properties within a platform of the electrode, it is highly desirable to deduce the architecture-performance relationships in the electrode. Moreover, in-depth mechanistic analysis can further shed a light on the design of functional electrodes with optimum performance.

In this regard, we propose to construct tailorable three-dimensional (3D) hybrid multilayer electrode fabricated by layer-by-layer (LbL) assembly toward simultaneous HMF conversion and H_2 production. Furthermore, we unravel the relations between electrocatalytic activity and nanoarchitectures of bimetallic electrodes by controlling sequence of metal NPs (**Figure 5.11**).

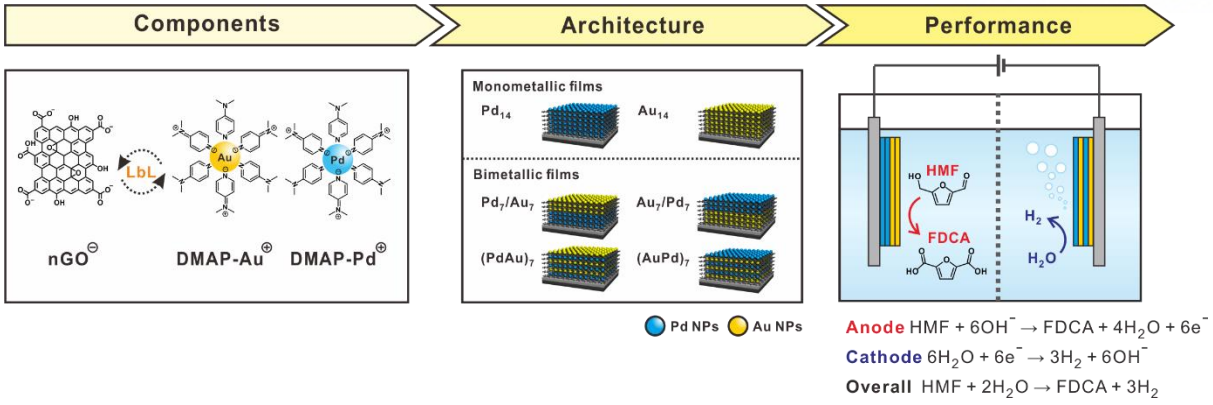

Figure 5.11. Schematic representation of LbL-assembled hybrid 3D multilayer thin film electrodes toward bifunctional biomass reforming and H_2 production

5.3.3. Experimental

5.3.3.1. Preparation of Nano Sized GO (nGO)

nGO was synthesized from graphite nanofibers (Catalytic Materials, United States) according to a previously reported method.[27] Graphite oxide was synthesized by the modified Hummers method and exfoliated to obtain a brown dispersion of nGO under ultrasonication at a concentration of 0.50 mg mL^{-1}.

5.3.3.2. Preparation of Au and Pd NPs

The 4-(dimethylamino)pyridine (DMAP)-stabilized Au and Pd NPs were prepared via spontaneous phase transfer from an organic solvent, using a previously reported method.[28]

5.3.3.3. LbL Assembly of Hybrid Electrode Films

An ITO-coated glass substrate was cleaned via sonication in deionized (DI) water, acetone, and ethanol for 10 min. Si and quartz substrates were cleaned with a piranha solution to remove organic contamination, followed by treatment with (3-aminopropyl)triethoxysilane to introduce a positively charged hydrophilic surface. These substrates were first dipped into a negatively charged nGO solution (0.50 mg mL^{-1}) with a pH of 4 for 10 min. They were then dipped into DI water for 1 min three times to remove loosely bound nGO. Subsequently, the substrates were dipped into a positively charged DMAP-coated Au or Pd NP suspension with a pH of 11 for 10 min and washed with DI water three times for 1 min, yielding a 1-BL film of $(nGO/Au)_1$ or $(nGO/Pd)_1$, respectively. The foregoing procedures were repeated to obtain the desired number of BLs (n). Multicomponent assembly was conducted using the identical procedure with both Au and Pd NP suspensions. All the as-assembled multilayer films were subjected to thermal reduction at 150 °C for 12 h in an oven before the electrochemical analysis.

5.3.3.4. Electrochemical Analysis

Electrochemical experiments were performed using a standard three-electrode cell configuration (Bio-Logic Science Instruments, VSP). A Pt wire was used as a counter electrode, and Hg/HgO was used as a reference electrode. The working electrode was a multilayer thin film assembled on ITO-coated glass. LSV and cyclic voltammetry were performed between –0.6 and 0.6 V *vs.* Hg/HgO in a 1.0 M KOH solution with a 10 mM HMF solution at 25 °C at a scan rate of 20 mV s^{-1}. The current density was calculated by dividing with the geometric area (cm^2) of the as-prepared LbL-assembled electrodes. The values of the potential were converted from *vs.* Hg/HgO to *vs.* RHE as follows: Hg/HgO + 0.924 V = RHE. Electrochemical impedance spectroscopy measurements were performed in the frequency range of 100 kHz to 100 mHz under an alternating-current stimulus.

5.3.3.5. Characterizations

The absorbance of the thin films was characterized by using UV/vis spectroscopy (UV-2550, Shimadzu). The thickness of the as-prepared samples on Si substrates was measured using a surface profiler (DektakXT Stylus Profiler, Bruker). The surface morphology of the samples was investigated using atomic force microscopy (AFM, NX-10, Park Systems) in a noncontact mode. The size and morphology of the prepared NPs were measured by transmission electron microscopy (TEM, JEM-2100, JEOL). The cross-sectional TEM samples were prepared using a focused ion-beam (FIB) technique (Crossbeam 540, ZEISS), and cross-sectional images were obtained by high-resolution transmission electron microscopy (HR-TEM), high-angle annular dark field scanning transmission electron microscopy (HAADF-STEM), and energy dispersive X-ray spectroscopy (EDXS) (JEM-F200, JEOL). The active mass of each material adsorbed onto the film surface was analyzed by a quartz crystal microbalance (QCM, QCM200, Stanford Research Systems).[29] The intermediates during the reaction were investigated by high performance liquid chromatography (HPLC, (Shimadzu Prominence). To study the oxidation products of HMF, 0.2 mL of electrolyte was collected every 30 min during chronoamperometry at 0.82 V (*vs.* RHE) and then analyzed by HPLC at room temperature. The products, including HMF, HFCA, FFCA, and FDCA, were separated using a C18 column (200 × 4.6 mm^2). The furan compounds were detected using a UV detector at 265 nm. The mobile phase was composed of water and methanol, with a ratio of 90:10, and the flow rate was set as 1.0 mL/min. Each concentration of products was quantified by a calibration curve with standard samples.

5.3.4. Results and Discussion

Initially, highly stable aqueous suspensions of nGO and metal NPs were synthesized to fabricate 3D LbL-assembled electrocatalytic electrodes via electrostatic interactions. In accordance with our previous study on diffusion-controlled multilayer electrodes employing nGO, we prepared a negatively charged nGO suspension via exfoliation from a graphite nanofiber precursor.[30] In parallel, positively charged Au and Pd NP suspensions were prepared via the spontaneous phase transfer of an organic solvent into an aqueous phase using 4-(dimethylamino)pyridine (DMAP), to exclude the effect of electrochemical charge-transfer kinetics caused by using different capping layers on the surface of the metal NPs. The average diameters of the Au and Pd NPs were determined to be 5.8 nm and 3.4 nm, respectively, by transmission electron microscopy (TEM, **Figure 5.12**).

Using these stable suspensions of positively charged Au and Pd NPs as electroactive species and the negatively charged nGO suspension as a catalytic support, we fabricated monometallic electrodes via LbL assembly onto indium tin oxide (ITO) substrates consisting of nGO and either Au or Pd NPs to obtain a thin-film electrode of $(nGO^{-}/Au^{+})_n$ or $(nGO^{-}/Pd^{+}/)_n$ (n = number of bilayers (BLs)). Furthermore, bimetallic hybrid electrodes composed of both Au and Pd NPs were assembled with various structures, including substrate/$(nGO^{-}/Au^{+})_n$/$(nGO^{-}/Pd^{+}/)_n$, substrate/$(nGO^{-}/Pd^{+}/)_n$/$(nGO^{-}/Au^{+})_n$, and substrate/$(nGO^{-}/Au^{+}/nGO^{-}/Pd^{+})_m$ (m = number of tetralayers (TLs)). Hereafter, for simplicity, the monometallic thin-film electrodes are denoted as Au_n and Pd_n, and the bimetallic thin-film electrodes are denoted as Au_n/Pd_n, Pd_n/Au_n, and $(AuPd)_n$.

The successful linear growth of each multilayer electrode was monitored by the gradual increase of absorbance upon increasing the number of layers in UV/vis spectra (**Figure 5.13**(a)-(d)). The thickness of each multilayer film also exhibited a linear growth with an average BL thickness of 13.3 nm and 18.8 nm for a single BL of the Au_n and Pd_n multilayers, respectively, and 29.8 nm for a single TL of the $(AuPd)_n$ electrode (**Figure 5.13**(e)). To monitor the sequential adsorption behavior of the components, such as nGO, Au NPs, and Pd NPs, in the $(AuPd)_n$ multilayer electrodes, a quartz-crystal microbalance (QCM) was used to perform measurements with respect to the number of deposition steps (**Figure 5.13**(f)). The average mass of each layer within a single TL was determined to be 0.21 μg cm^{-2}, 6.35 μg cm^{-2}, and 1.03 μg cm^{-2} for nGO, Au NPs, and Pd NPs, respectively.

Using seven BLs of each metal NP electrode as a representative example, which exhibited the optimal electrocatalytic activity, the internal architecture of the multilayer film electrodes was controlled with various structures, such as a fully alternating $(AuPd)_7$ electrode and opposite structures of Au_7/Pd_7 and Pd_7/Au_7 multilayer electrodes. The nanoarchitectures of the fabricated thin film electrode were examined via cross-sectional transmission electron microscopy (TEM) (**Figure 5.14**) and atomic force microscopy (AFM) (**Figure 5.15**). The multilayer electrodes with different architectures were clearly observed with the aid of the contrast difference in elemental mapping between the Au and Pd NPs (**Figure 5.14**). According to the AFM images for the surface analysis, the

root-mean-squared surface roughness (R_{rms}) values (averaged over 25 × 25 μm^2) for the Pd_7/Au_7, Au_7/Pd_7, and $(AuPd)_7$ multilayer film electrodes were determined to be 80.9, 58.2, and 40.7 nm, respectively. This tendency is in accordance with a previous study where large Au NPs were deposited on a surface, yielding a surface roughness significantly higher than that for smaller Pd NPs.[29]

Initially, we investigated the electrocatalytic oxidation of HMF for each electrode to identify the architecture–performance relationships for the electrocatalytic reaction. Because the OER was the major reaction competing with HMF oxidation, water oxidation in the absence of HMF was first investigated using one of the bimetallic Pd_7/Au_7 electrodes, which had the optimal performance for HMF oxidation (**Figure 5.16**). Without HMF, the linear sweep voltammetry (LSV) curve showed an anodic current onset at 1.53 V (*vs.* reversible hydrogen electrode (RHE)), resulting from the OER. In contrast, the anodic onset potential was approximately 0.34 V (*vs.* RHE) in the presence of 10 mM HMF, indicating that the oxidation of HMF was significantly favored over water oxidation.

To evaluate the electrocatalytic activity with respect to the thickness of the electrodes, we measured the LSV curves according to the number of BLs for Au_n and Pd_n electrodes (**Figure 5.17**(a) and (b)). In our previous studies, the performance of LbL-assembled multilayer electrodes was highly dependent on the number of layers (i.e., thickness), which is related to the concentration of electrocatalytically active NPs.[29, 31-33] However, the electrocatalytic performance began to decrease after a critical thickness was reached, due to the limitation of the mass transfer of the active reagents into the electrodes. As shown in **Figure 5.17**(d), for both the Au_n and Pd_n monometallic electrodes, the current density for HMF oxidation gradually increased with the increasing thickness, up to 14 BLs. With a further increase in the thickness, the electrocatalytic activity decreased significantly due to the limited mass transfer of HMF into the 3D electrode, which was closely related to the layered 2D structure of GO nanosheets within the multilayer electrodes. Interestingly, the current density of the Au_n electrodes was higher than that of the Pd_n electrodes (**Figure 5.17**(c)), whereas the Pd_n electrodes exhibited a significantly lower peak potential (0.77 V *vs*. RHE) than the Au_n electrodes (1.2 V *vs*. RHE). For these reasons, we expected that the bimetallic system combining Au and Pd NPs would improve the electrocatalytic performance, reducing the onset potential as well as increasing the anodic current for HMF oxidation.

On the basis of the optimized catalytic activity of the monometallic system at 14 BLs achieved through a fine balance between the HMF oxidation and electron-transfer process, four different bimetallic systems with 7 BLs of each metal NP (a total of 14 BLs, i.e., the optimal number) were fabricated with Au and Pd NPs: Au_7/Pd_7, Pd_7/Au_7, $(AuPd)_7$, and $(PdAu)_7$. All the assembled electrodes were investigated to identify the architecture–performance relationship toward HMF oxidation. As indicated by the LSV measurements (**Figure 5.18**), all bimetallic film electrodes exhibited significantly improved electrocatalytic activity, with an increased peak current density and a low peak potential, in comparison with the monometallic Au_{14} and Pd_{14} electrodes. Among them, the

fully alternating $(Pd/Au)_7$ bimetallic electrode exhibited the highest current density of 3.24 mA cm^{-2}, which was a 225% improvement in comparison with that of the monometallic Pd_{14} electrode. The Pd_7/Au_7 bimetallic electrode had the lowest peak potential (0.76 V *vs.* RHE), clearly suggesting that there was a synergistic effect for HMF oxidation within the heterogeneous bimetallic 3D multilayer electrodes.

Encouraged by the improved electrocatalytic behavior of the bimetallic Au and Pd NPs toward HMF oxidation, we then examined the relationship between the architecture of the multilayer electrodes and the electrochemical behavior in further detail. Generally, there are two possible pathways in the HMF oxidation reaction to produce FDCA through various reaction intermediates of different oxidation levels (**Figure 5.19**(a)).[17, 34-35] To investigate the mechanisms of HMF oxidation for the Au-Pd bimetallic system, chronoamperometric (CA) tests were performed at a constant potential of 0.82 V (*vs.* RHE), which corresponds to the peak potential of HMF oxidation. During the electrocatalytic oxidation, the concentration of HMF and its corresponding oxidation products with various LbL-assembled electrodes were monitored by high-performance liquid chromatography (HPLC) (**Figure 5.19**(b) and (c), and **Figure 5.20**(b)). Among them, 5-(hydroxymethyl)furan-2-carboxylic acid (HFCA) appeared as a major intermediate, whereas 2,5-furandicarbaldehyde (FDA) was not observed in the overall reaction (**Figure 5.20**(b)). This observation indicates that the oxidation of the aldehyde group was more favorable than that of the alcohol group of HMF in our system.

For both the mono- and bimetallic electrodes, the conversion of HMF occurred rapidly in the early stage (within 30 min), except only for the monometallic Pd_{14} electrode, which exhibited a significantly low HMF conversion of 4.92% after 30 min (**Figure 5.21**). It is also of note that the monometallic Au_{14} electrode displayed a poor yield of the final product 2,5-furandicarboxylic acid (FDCA) (3.22%), albeit with a high yield of HFCA (23.6%) from HMF (**Figure 5.21**), indicating that the Au NPs were more effective than Pd NPs for the oxidation of HMF to HFCA. In contrast, the HMF conversion of the Pd NPs was significantly slower but resulted in more highly oxidized products, i.e., FDCA. Thus, the conversion efficiency from HFCA to FDCA for Pd_{14} was 53.2%, which was much higher than that of Au_{14} (12.0%), in addition to the significantly reduced HFCA yield for all the Pd-supported Au bimetallic electrodes. These results indicate that the conversion of HFCA was more favorable for the Pd NPs than for the Au NPs.

After the slow rate-limiting steps for pure Au and Pd monometallic electrodes were identified, conclusions could be drawn regarding the benefit of Au-Pd bimetallic electrodes for FDCA production. Combining both Au and Pd NPs led to more facile aldehyde oxidation at a low potential with an enhanced alcohol oxidation activity in comparison with individual single components. Indeed, the bimetallic system exhibited an FDCA yield more than two-fold higher than that of the monometallic electrodes. More interestingly, even with the identical composition of NPs, the

electrocatalytic activity was tunable according to the location of the NPs within the multilayer electrodes, which could be related to the stepwise reaction pathway involved in the HMF oxidation. For instance, although the $(AuPd)_7$ and Pd_7/Au_7 electrodes exhibited similar FDCA yields, there was a significant difference in electrochemical activity between the electrodes with opposite layering sequences, i.e., Au_7/Pd_7 (Pd layer atop Au layer) and Pd_7/Au_7 (Au layer atop Pd layer) (**Figure 5.22**(b) and (c)). The current density of the Pd_7/Au_7 electrode (3.09 mA cm^{-2}) was significantly higher than that of the Au_7/Pd_7 electrode (2.53 mA cm^{-2}). Furthermore, the Pd_7/Au_7 electrode exhibited a higher yield of both FDCA (16.4%) and HFCA (10.1%) in comparison with the Au_7/Pd_7 electrode.

Because Au NPs favored the conversion of HMF into HFCA, HMF is rapidly oxidized to HFCA when Au NPs are located at the outer layer (**Figure 5.22**(a)). Indeed, both the Au_{14} and Pd_7/Au_7 electrodes exhibited a high concentration of HFCA (**Figure 5.22**(c)). Subsequently, the generated HFCA served as a reactant on Pd NPs to facilitate afford the conversion toward the final product, i.e., FDCA. The Au NPs supplied an additional reactant, i.e., HFCA, to the surface of the Pd NPs and increased the concentration, resulting in enhanced mass transfer for the 3D multilayer electrodes. Therefore, when Au NPs were located at the outer layer, as in the case of the Pd_7/Au_7 electrode, the current density was high owing to the enhanced mass transfer into inner-layer Pd NPs for the effective oxidation toward FDCA.

To verify this interpretation, we investigated the electrocatalytic oxidation of the intermediate HFCA compound using Pd_7/Au_7 and Au_7/Pd_7 electrodes (**Figure 5.23**). In contrast to the case of HMF oxidation, the Au_7/Pd_7 electrode exhibited a higher FDCA yield (17.5%) and current density (2.17 mA cm^{-2}) than the Pd_7/Au_7 electrode (13.0% and 1.55 mA cm^{-2}, respectively). Thus, when Pd NPs existed at the outer layer (Au_7/Pd_7 electrode), the electrocatalytic performance for converting HFCA was high, because Pd NPs could rapidly oxidize HFCA to FDCA. These differences in the electrocatalytic performance and product distribution clearly demonstrate that the reaction pathway of HMF oxidation is highly dependent on the types of catalysts and the architecture of bimetallic electrodes, which is difficult to observe in other conventional electrode manufacturing techniques.

For successful coupling of the full cell system with simultaneous FDCA and H_2 production, the LbL-assembled multilayer electrodes require good HER performance in the presence of HMF. Here, the electrocatalytic activity for the HER was investigated for the synthesized multilayer electrodes in the absence and presence of 10 mM HMF (**Figure 5.24**). There was no significant change in the LSV curve, indicating that the cathodic H_2 evolution was not influenced by the presence of HMF. The electrocatalytic activity for the HER in the HMF solution was then investigated for LbL-assembled multilayer electrodes (**Figure 5.25**). When the Au and Pd NPs were assembled together, the HER activity was significantly improved, with a lower onset potential and a higher current density, compared with the case of the monometallic electrodes. Among the electrodes, the fully alternating

$(AuPd)_7$ electrode exhibited the best performance, with the highest current density (-8.62 mA cm^{-2}) at -0.4 V (*vs.* RHE) and the lowest onset potential (-0.10 V *vs.* RHE) at -0.2 mA cm^{-2}. The Au_7/Pd_7 electrode required a significantly higher overpotential of 0.18 V (*vs.* RHE) and had a lower current density (5.55 mA cm^{-2}), whereas the Pd_7/Au_7 electrode exhibited similar HER catalytic performance to $(AuPd)_7$, which is similar to the tendency of the electrocatalytic performance for HMF oxidation.

To correlate the nanoarchitecture and performance of the multilayer electrodes with the mechanisms for the HER, the electrochemical kinetics for the HER was investigated using the Tafel slopes of the LbL-assembled electrodes. As described in the section related to the HMF oxidation reaction, the HER activity strongly depends on the architecture of the multilayer electrodes. For example, both monometallic electrodes—Au_{14} and Pd_{14}—exhibited a low HER activity, with a high Tafel slope of 288 and 174 mV dec^{-1}, respectively, in the Tafel region of -0.06 to -0.33 V (**Figure 5.26**). In contrast, the bimetallic $(AuPd)_7$ and Pd_7/Au_7 electrodes exhibited significantly improved kinetics, with a lower Tafel slope of 105–109 mV dec^{-1}, which is comparable to the values reported for other catalysts.[36-37]

It is widely known that in the first step of the HER, a water molecule receives an electron and generates an adsorbed H atom (H_{ads}) as an intermediate (Volmer reaction) on the surface of the catalysts.[38-39] In the second step, the electron is transferred to the H_{ads}, and generated H_2 molecules are then released on the catalyst surface via a Tafel or Heyrovsky reaction. Therefore, the optimal Gibbs free energy for H_{ad} between the adsorption and desorption of hydrogen in the volcano plots ($\Delta G_{Had} \approx 0$) is necessary to develop highly efficient HER electrocatalysts.

According to the volcano plots for the HER, which are correlated to the binding energy of H_{ads}, Pd has a small energy barrier with negative ΔG_{Had} for the adsorption of protons.[39-43] On the other hand, Au, which has a high ΔG_{Had} for H_{ad} ($\Delta G_{Had} > 0$) can participate more easily in the desorption process. Therefore, the diffusion coefficient of H_{ads} atoms on Au is approximately 1.47×10^{-3} cm^2 s^{-1},[44] which is significantly higher than that on a Pd surface (1.30×10^{-7} cm^2 s^{-1}).[45] According to these distinctive features of relatively adsorption-like Pd and desorption-like Au, H_{ads} was more favorable to form on the surface of Pd layers in our Au-Pd bimetallic multilayer electrodes. The hydrogen coverage on the restricted Pd surface increases rapidly, and the excessive H_{ads} atoms begin to spill over from hydrogen-rich Pd to the nearby hydrogen-poor Au NP layers, freeing Pd sites that can be filled by newly H_{ads}. Thus, in addition to the possible desorption of hydrogen on the Pd surface, the chemical desorption of spilled over hydrogen can occur on the adjacent Pd-Au and/or Au-Au layers within the multilayer electrodes. Consequently, the electrocatalytic HER activity of the bimetallic electrodes is significantly improved in comparison with that of the monometallic electrodes, because the excessive H_{ads} produced on the Pd layers quickly spills over to the neighboring Au and then undergoes fast desorption (**Figure 5.27**). According to the previous researches, the effect of hydrogen spillover in heterogeneous catalysts has been reported for diverse alloy systems.[43-44, 46-49] In concert

with our results, by employing both experimental and theoretical approaches, Sykes et al. demonstrated a similar spillover phenomenon of H_2 onto Au-supported Pd clusters.[49]

For these reasons, a large number of contact layers between Au and Pd NPs in the fully alternating $(AuPd)_7$ multilayer electrode yielded a low R_{ct} of 135 Ω (**Figure 5.28**), which eventually resulted in better performance in comparison with the other bimetallic electrodes, i.e., Pd_7/Au_7 and Au_7/Pd_7. In the case of the same number of contact layers between Au and Pd layers, e.g., Au_7/Pd_7 and Pd_7/Au_7, Pd NPs located at the inner layer (Pd_7/Au_7) may be more beneficial not only for forming a high concentration profile of H_{ads} within the Nernst diffusion layer at the bottom end of the catalytic electrodes underneath, but also for facilitating the HER kinetics, with a low R_{ct} value of 190 Ω (compared with 1397 Ω for the Au_7Pd_7 electrode).

According to our investigation of the nanoarchitecture-related electrocatalytic performance, we fabricated the full-cell system exclusively with LbL-assembled electrodes. The system was optimized for the respective half-cell reactions. Because the full-cell system requires a higher energy than the half-cell system, the overall catalytic performance differed considerably depending on the architecture of the multilayer film electrodes. As depicted in **Figure 5.29**(a), the Pd_7/Au_7 electrode was optimized to produce FDCA, whereas the fully alternating $(AuPd)_7$ electrode was the best architecture for the HER. Indeed, when we combined Pd_7/Au_7 as the anode and $(AuPd)_7$ as the cathode, the full-cell electrocatalytic performance was maximized, with the highest current density of 4.54 mA cm^{-2} among all the assembled combinations of the electrodes (**Figure 5.29**(b)).

These results confirmed that a rational strategy for controlling the architecture is essential for controlling the electrocatalytic activity. This fine control is particularly important in the case of cascade or tandem reactions, because the deposition sequence of active NPs is critical, as each type of NP has different kinetics and a different energy barrier for the chemical reactions. As demonstrated in this study, HMF oxidation requires several oxidative processes to produce FDCA. While Au NPs are more favorable for converting HMF into the intermediate HFCA, Pd NPs can rapidly convert HFCA into the final product FDCA. In the case of the HER, an architecture with adjacent Pd and Au (fully alternating $(AuPd)_7$ electrode) is highly desirable for the rapid spillover of adsorbed hydrogen from the Pd NPs to the Au NPs.

Furthermore, we examined the applicability of the LbL-assembled film electrodes as photoelectrocatalytic electrodes to employ solar energy and reduce the external voltage necessary for HMF oxidation (**Figure 5.30**). The Pd_7/Au_7 electrode, which exhibited the optimized catalytic performance, served as the photoanode, and Pt mesh was used as the counter electrode. Surprisingly, the Pd_7/Au_7 electrode exhibited a photoelectrocatalytic activity without any treatment and additional photoelectrode under sunlight irradiation, which can be attributed to plasmon-induced hot carriers.[50-52] With irradiation, the onset potential decreased from 0.19 to 0.07 V (*vs.* RHE), accompanied by a significant increase in the current density, suggesting the potential of the prepared multilayer thin

electrode for photoelectrocatalytic reactions. The correlation of the nanoarchitecture of the multilayer electrodes with respect to their activity for the photoelectrocatalytic reactions will be the subject of our on-going effort.

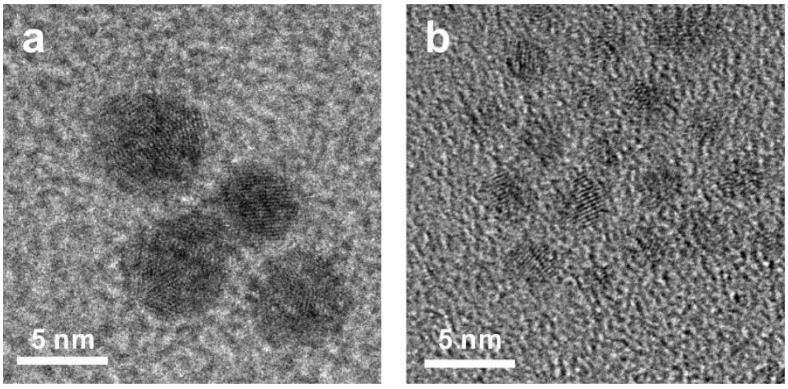

Figure 5.12. TEM image of (a) DMAP-Au NPs suspension and (b) DMAP-Pd NPs suspension.

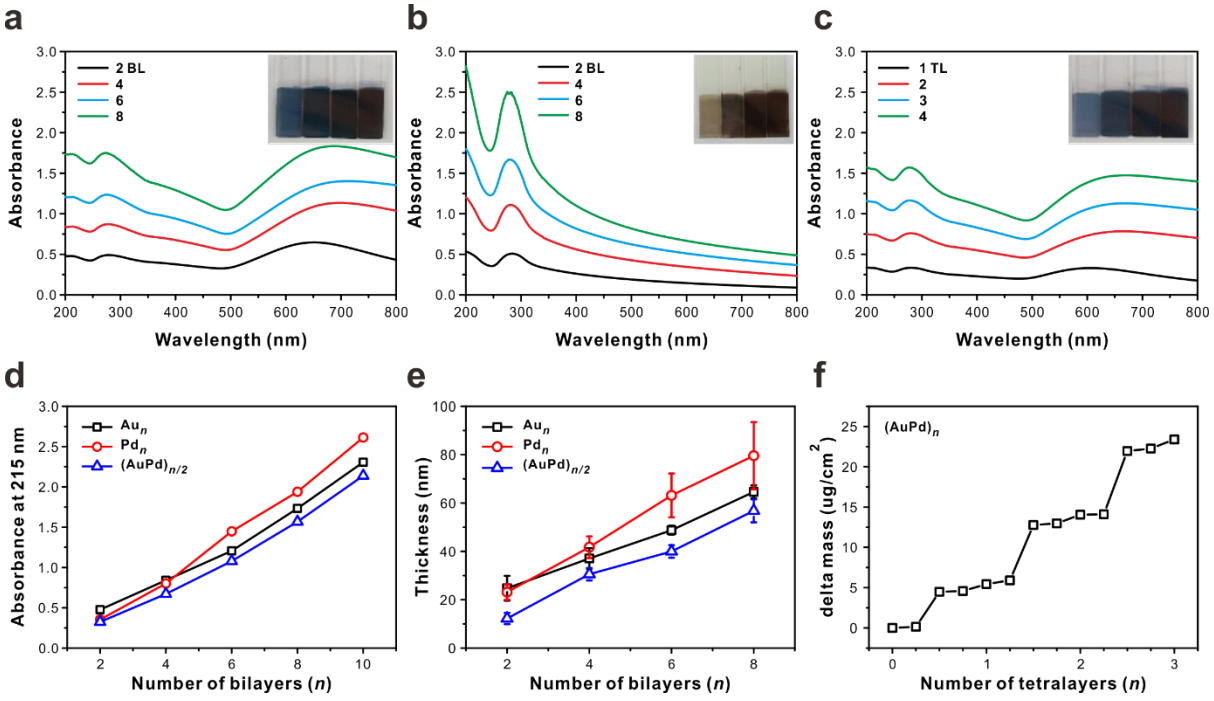

Figure 5.13. UV/vis absorbance spectra of representative (a) Au_n, (b) Pd_n, and (c) $(AuPd)_n$ multilayer thin films. The inset image shows the samples prepared with the corresponding number of bilayers (BLs, n). (d) UV/vis absorbance maxima at 215 nm for each multilayer electrode, (e) film thickness measured by surface profiler, and (f) quartz crystal microbalance (QCM) analysis of the $(AuPd)_n$ electrodes as a function of the number of BLs (n).

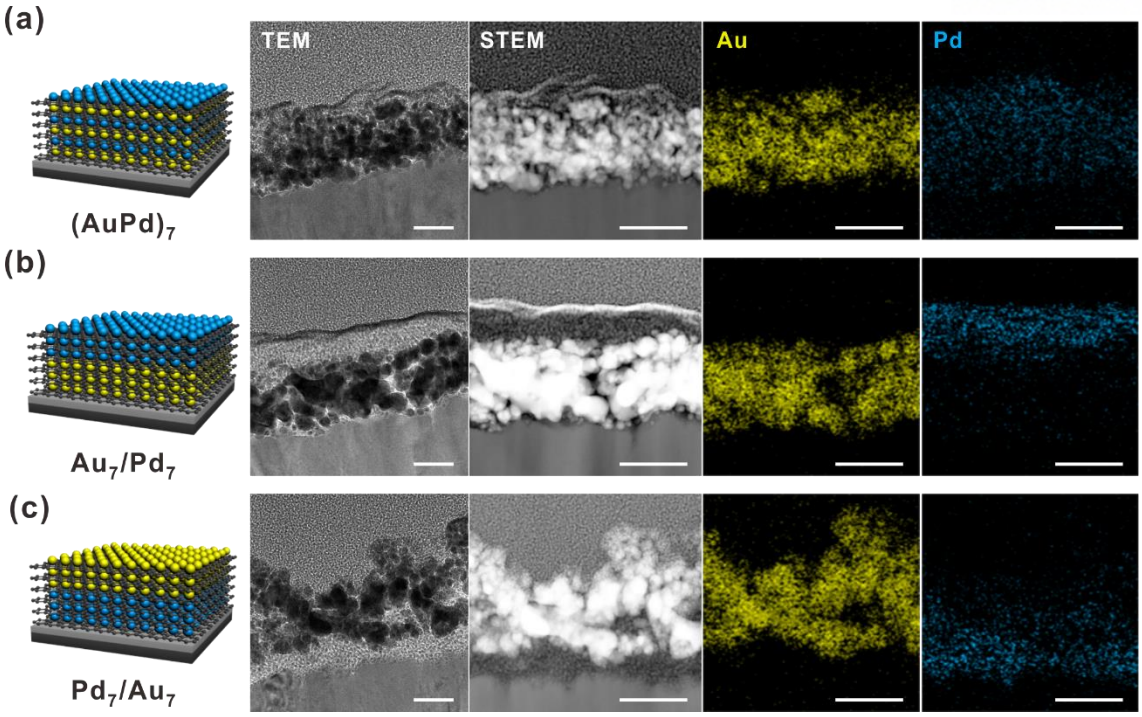

Figure 5.14. Architecture controlled multilayer thin film electrodes. Representative cross-sectional TEM, STEM and EDS mapping images of (a) $(AuPd)_7$, (b) Au_7/Pd_7 and (c) Pd_7/Au_7 multilayer thin film electrodes assembled on an ITO-coated substrate. (Scale bar: 50 nm)

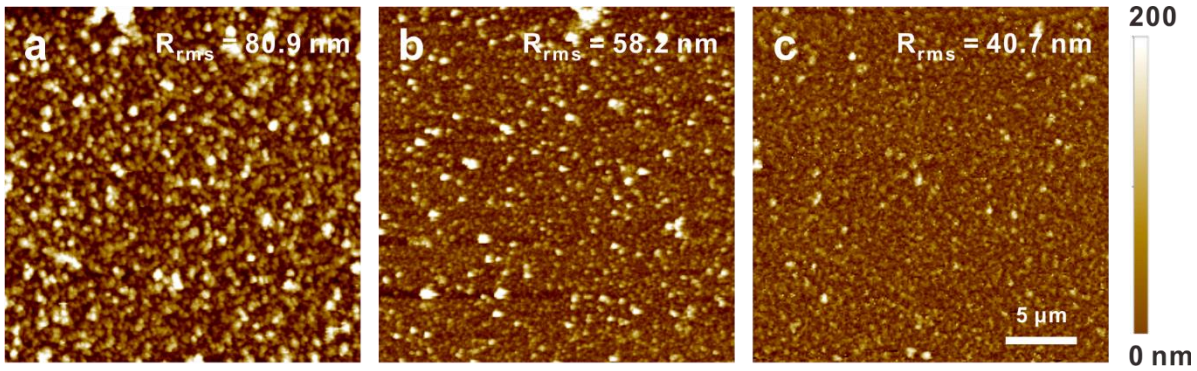

Figure 5.15. Representative AFM images of (a) Pd_7/Au_7, (b) Au_7/Pd_7, and (c) $(AuPd)_7$ multilayer thin film electrodes. R_{rms} values of the AFM images are averaged over a 5 × 5 μm^2 area.

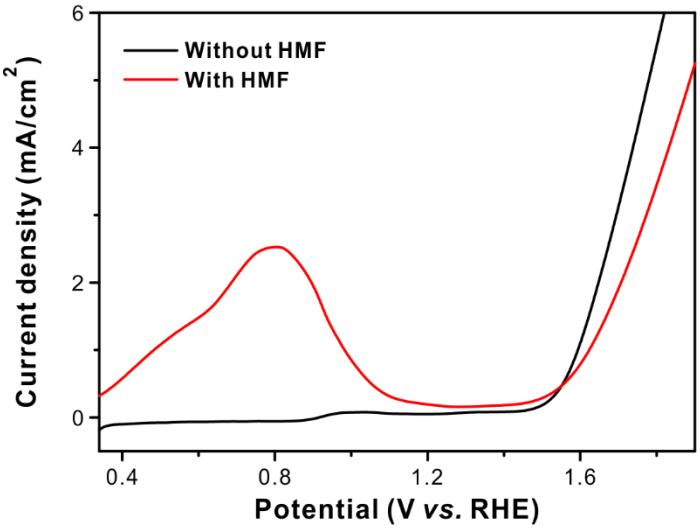

Figure 5.16. LSV curves of the Pd_7/Au_7 multilayer film at a scan rate of 2.0 mV s^{-1} in 1.0 M KOH with and without 10 mM HMF.

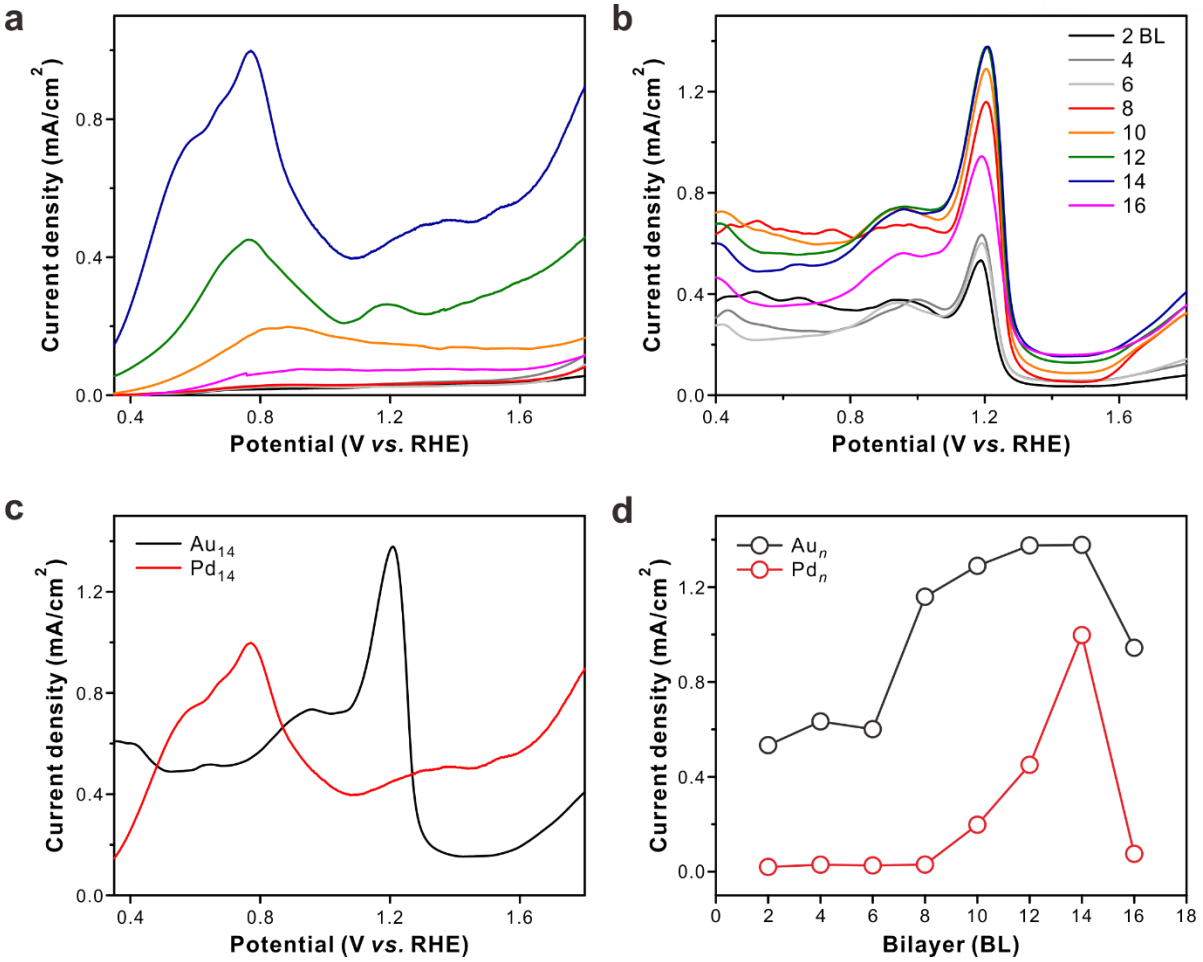

Figure 5.17. LSV curves of (a) Pd_n and (b) Au_n multilayer films electrodes according to the number of BLs, and (c) LSV curves of Au_{14} and Pd_{14} multilayer films, and (d) Comparison of the electrochemical performance toward the HMF oxidation as a function of the number of BLs. All LSVs were recorded in 1.0 M KOH with 10 mM HMF at a scan rate of 2.0 mV s^{-1}.

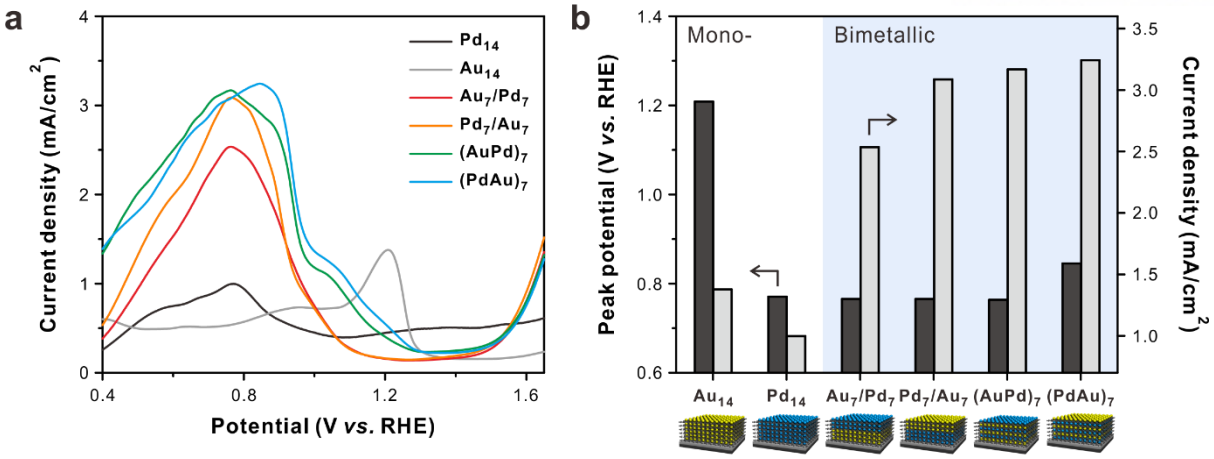

Figure 5.18. Electrocatalytic activity for HMF oxidation reaction of all film electrodes prepared in the study. (a) Linear sweep voltammograms (LSVs) measured at a scan rate of 2 mV s^{-1} with 10 mM HMF in 1.0 M KOH electrolyte and (b) comparison of the peak potential (black) and current density at the peak potential (gray) of each film electrode with corresponding architecture.

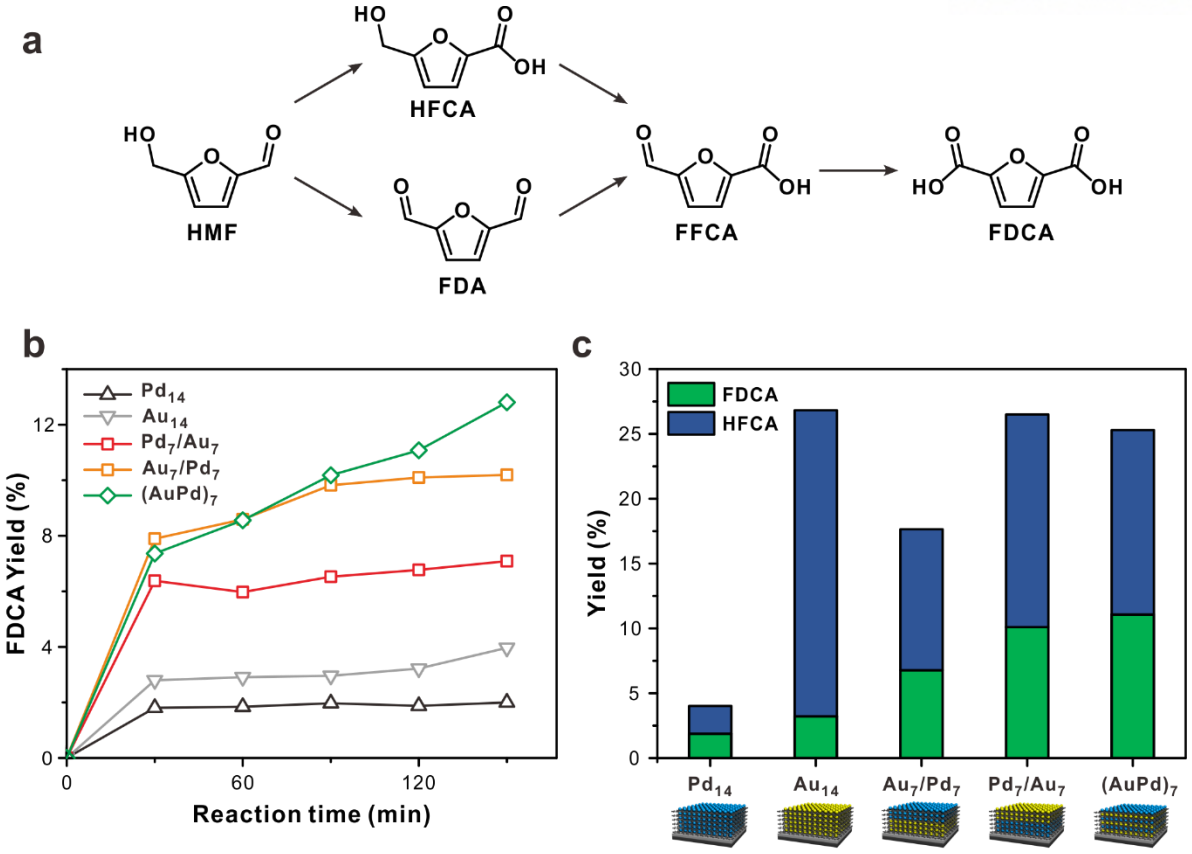

Figure 5.19. (a) Schematic reaction pathways for the sequential oxidation of HMF to FDCA through various reaction intermediates. (b) Yield of the final product FDCA from each electrode during the electrochemical oxidation, and (c) comparison of relative concentration ratio between HFCA and FDCA from different type of electrodes at 120 min. Reaction condition: 10 mL of 5 mM HMF in 1.0 M KOH; anode potential 0.82 V *vs.* RHE.

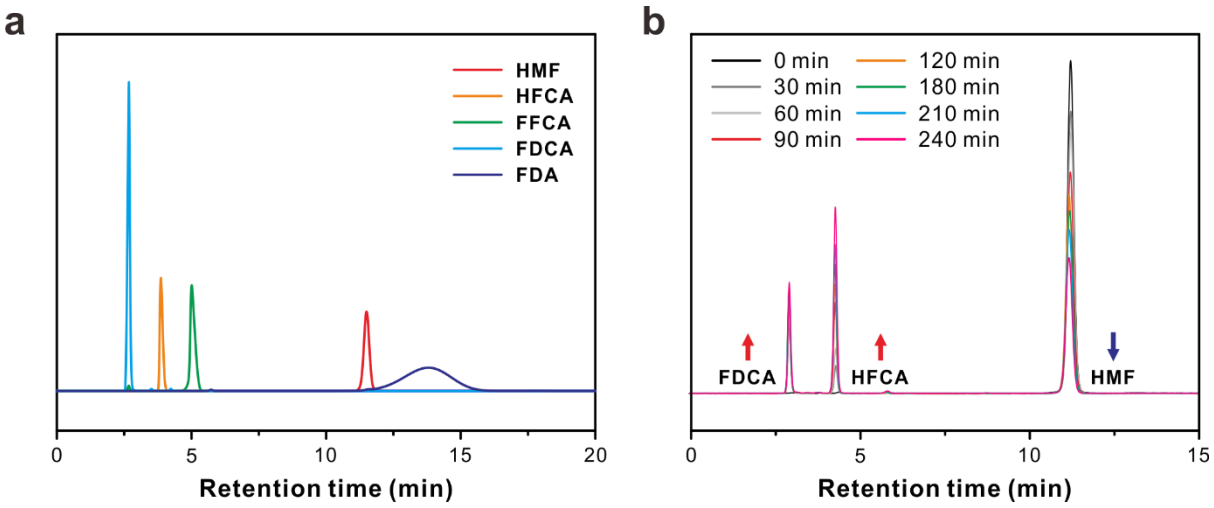

Figure 5.20. (a) Chromatograms for standard 5-(hydroxymethyl)furfural (HMF), 5-hydroxymethyl-2-furancarboxylic acid (HFCA), 5-formyl-2-furancarboxylic acid (FFCA), 2,5-Furandicarboxylic acid (FDCA), and 2,5-furandicarboxaldehyde (FDA) intermediates formed during the HMF oxidation measured via HPLC. (b) Representative HPLC traces of HMF oxidation catalyzed by Pd_7/Au_7 multilayer electrode at 0.82 V *vs.* RHE in 10 mL of 5 mM HMF in 1.0 M KOH.

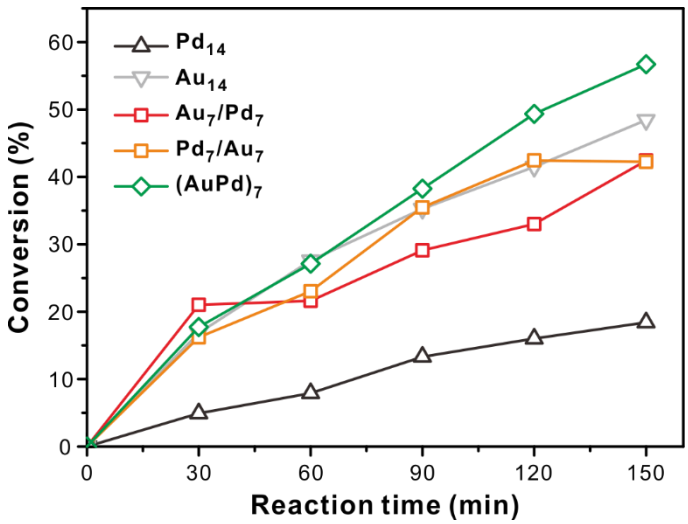

Figure 5.21. Conversion of HMF during the electrochemical oxidation according to the reaction time. Reaction condition: 10 mL of 5 mM HMF in 1.0 M KOH; anode potential 0.82 V *vs.* RHE.

Table 5.3. Conversion of HMF and Yield of FDCA from Different Type of Electrodes at 120 min. Reaction Condition: 10 mL of 5 mM HMF in 1.0 M KOH; Anode Potential 0.82 V *vs.* RHE

	Pd_{14}	Au_{14}	Au_7/Pd_7	Pd_7/Au_7	$(AuPd)_7$
Conversion of HMF (%)	16.0	41.5	33.0	42.4	49.3
Yield of FDCA (%)	1.87	3.22	6.77	10.1	11.1

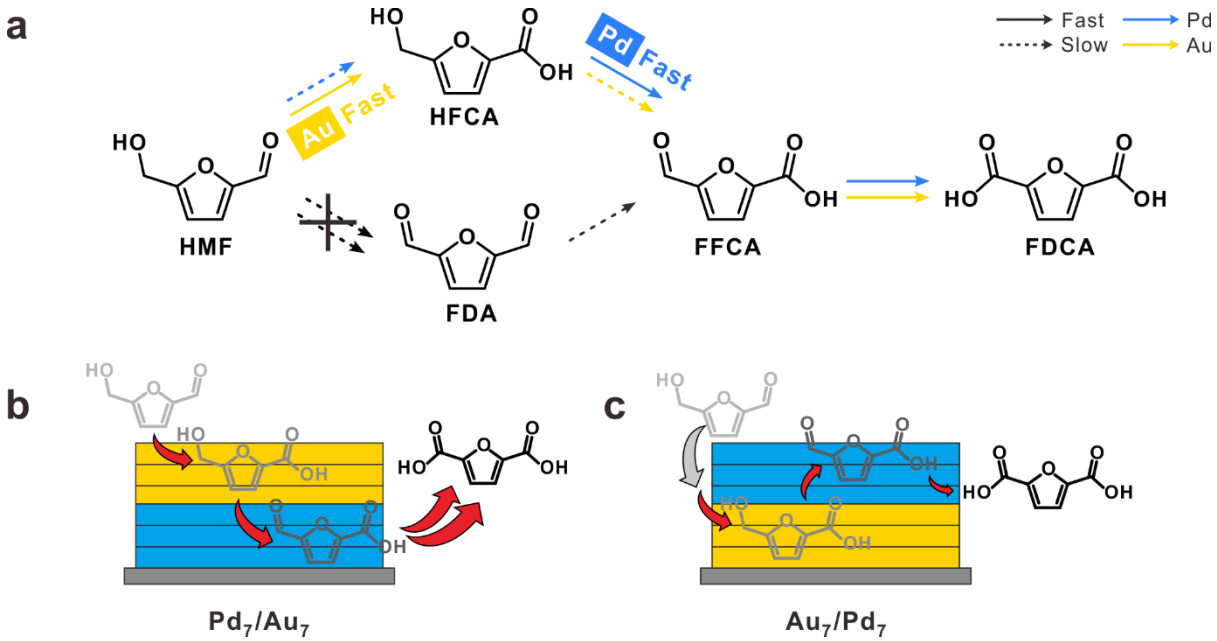

Figure 5.22. (a) Schematic reaction pathways for the sequential oxidation of HMF on Pd and Au NPs. Putative reaction mechanism with (b) Pd_7/Au_7 and (c) Au_7/Pd_7 multilayer electrodes to convert HMF to FDCA.

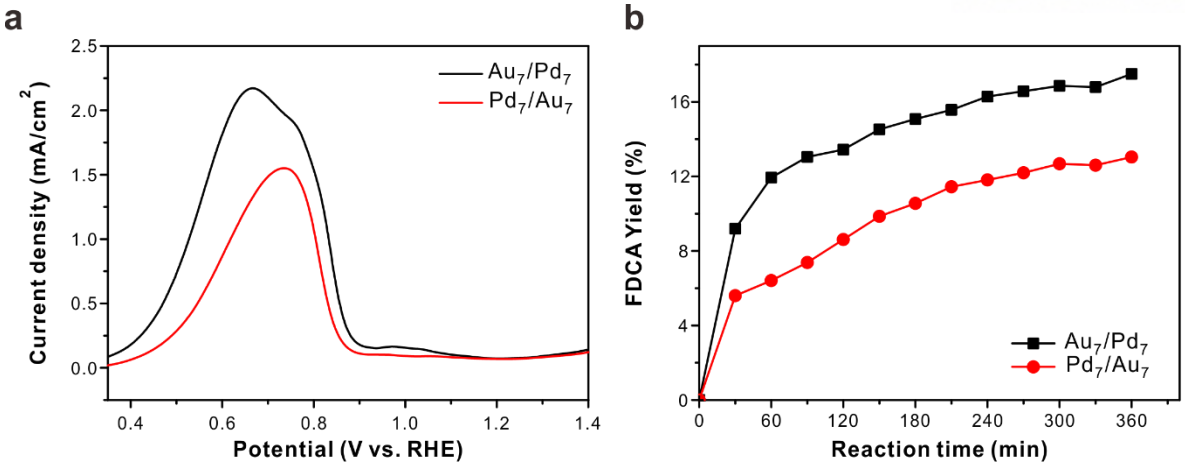

Figure 5.23. (a) LSV curves with Au_7/Pd_7 and Pd_7/Au_7 multilayer electrodes to convert HFCA to FDCA, and (b) FDCA yield from HFCA measured by HPLC. All LSVs were recorded in 1.0 M KOH with 10 mM HFCA at a scan rate of 2.0 mV s^{-1}.

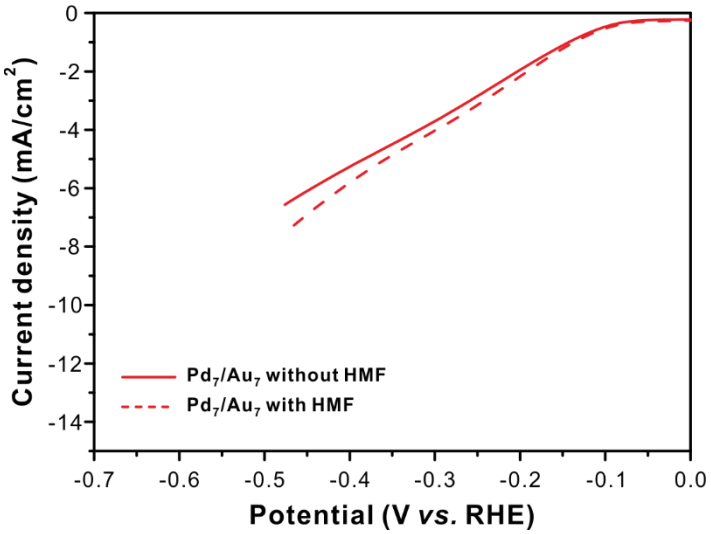

Figure 5.24. LSV curves for the Pd_7/Au_7 electrode in 1.0 M KOH with and without 10 mM HMF at a scan rate of 2.0 mV s^{-1}.

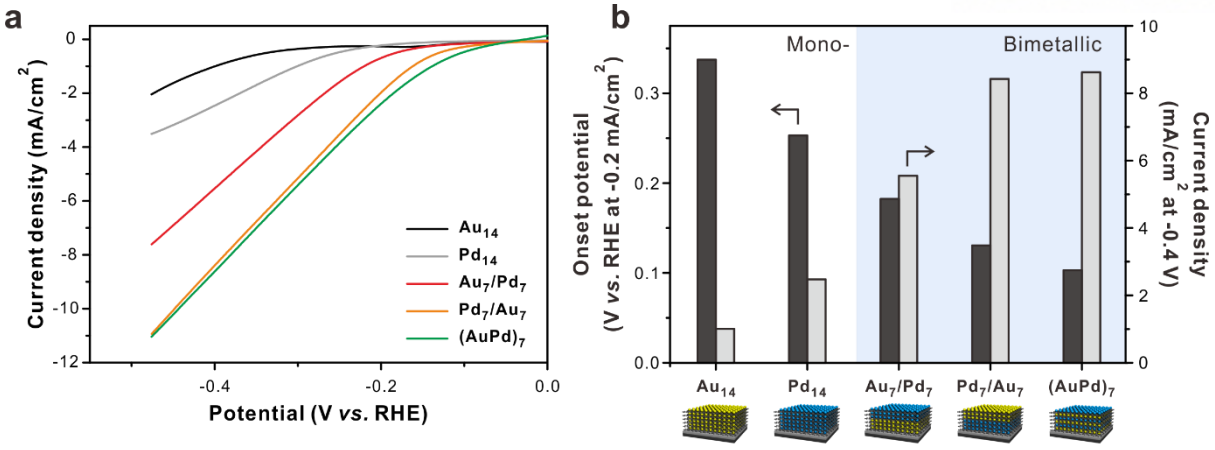

Figure 5.25. Electrocatalytic activity for HER. (a) Linear sweep voltammograms (LSVs) of all electrodes prepared in the study at a scan rate of 2 mV s^{-1} with 10 mM HMF in 1.0 M KOH electrolyte, and (b) comparison of the onset potential (black bar) with current density at -0.2 mA cm^{-2} and current density at -0.4 V *vs.* RHE (gray bar) of each electrode.

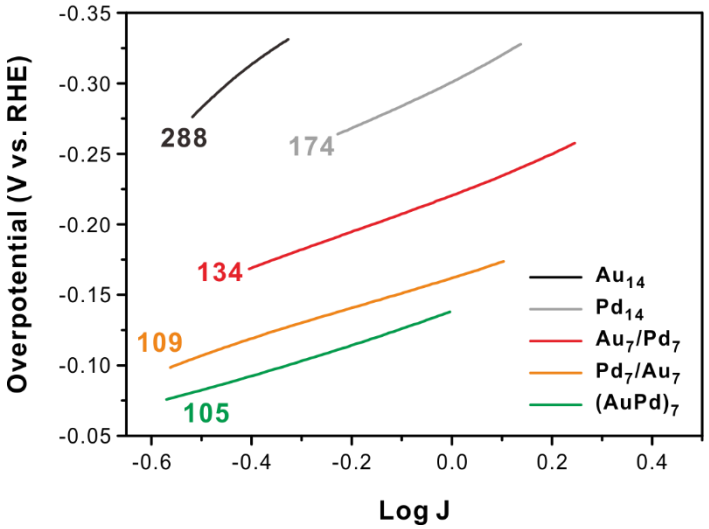

Figure 5.26. The corresponding Tafel plot of HER in Figure 5.25(a). Inset numbers represent the slope of each plots.

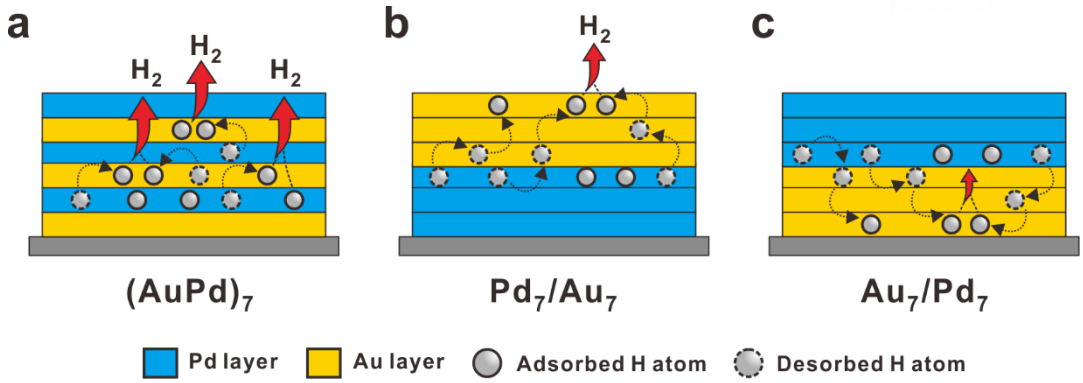

Figure 5.27. Schematic description of HER mechanism with (a) $(AuPd)_7$, (b) Pd_7/Au_7, and (c) Au_7/Pd_7 multilayer electrodes. Gray balls with solid line represent adsorbed H (H_{ads}) and desorbed H with dashed line

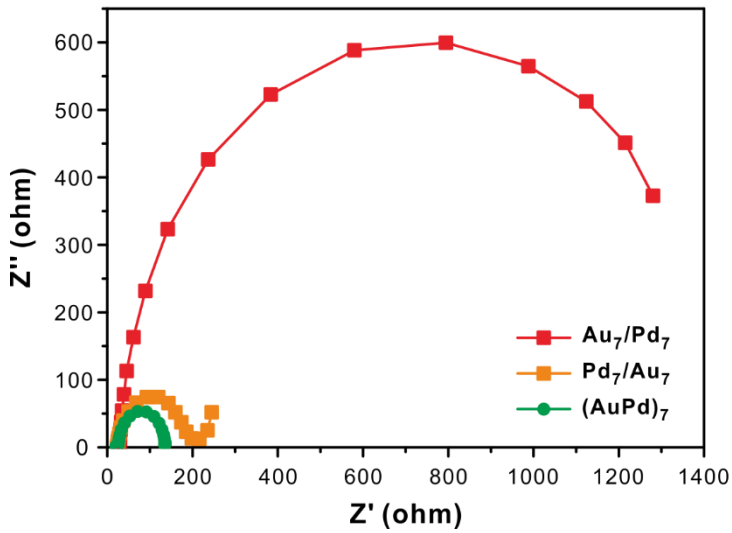

Figure 5.28. Nyquist plots of three different multilayered film electrodes (Au_7/Pd_7, Pd_7/Au_7, and $(AuPd)_7$) measured in a frequency range of 100 kHz to 50 mHz at -0.276 V (*vs*. RHE) in 1.0 M KOH with 10 mM HMF.

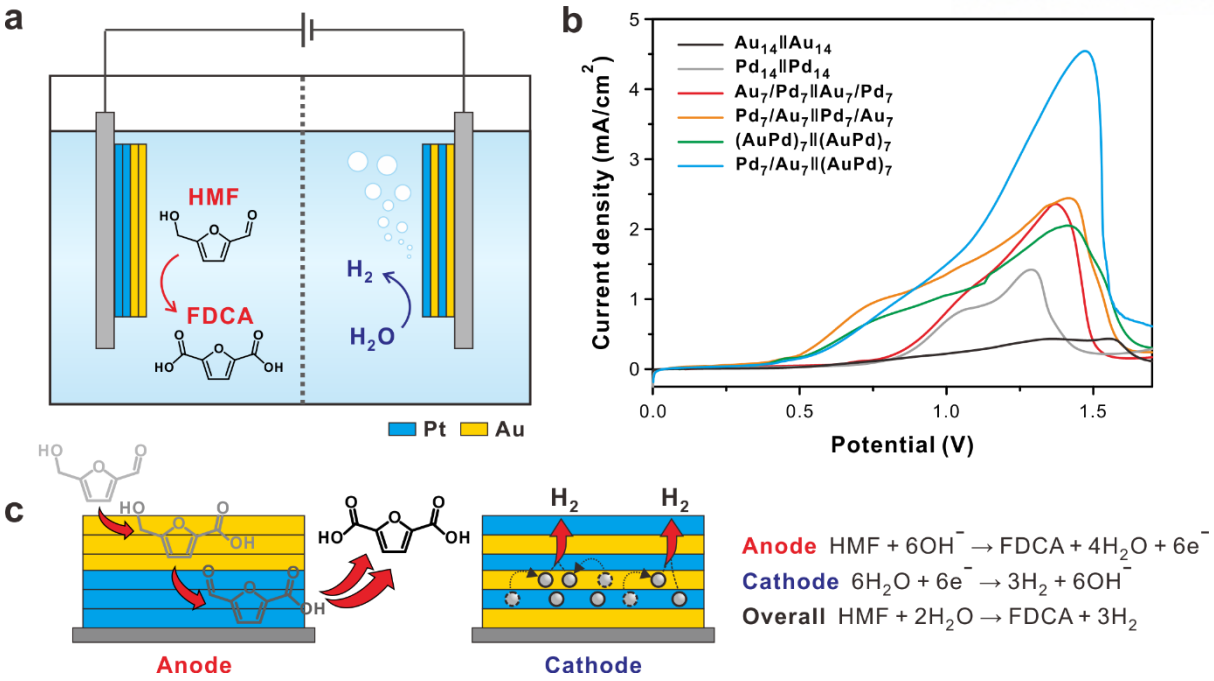

Figure 5.29. (a) Illustration of the optimized two-electrode full-cell system in this study to simultaneous generation of H_2 in cathode and FDCA in anode. (b) LSV curves of two-electrode full-cell system for HMF oxidation in 1.0 M KOH solution with 10 mM HMF using a scan rate of 2.0 mV s^{-1}. (c) Schematic description of $(AuPd)_7$ multilayer electrode for cathode and Pd_7/Au_7 multilayer for anode. Gray balls with solid line represent adsorbed H (H_{ads}) and desorbed H with dashed line.

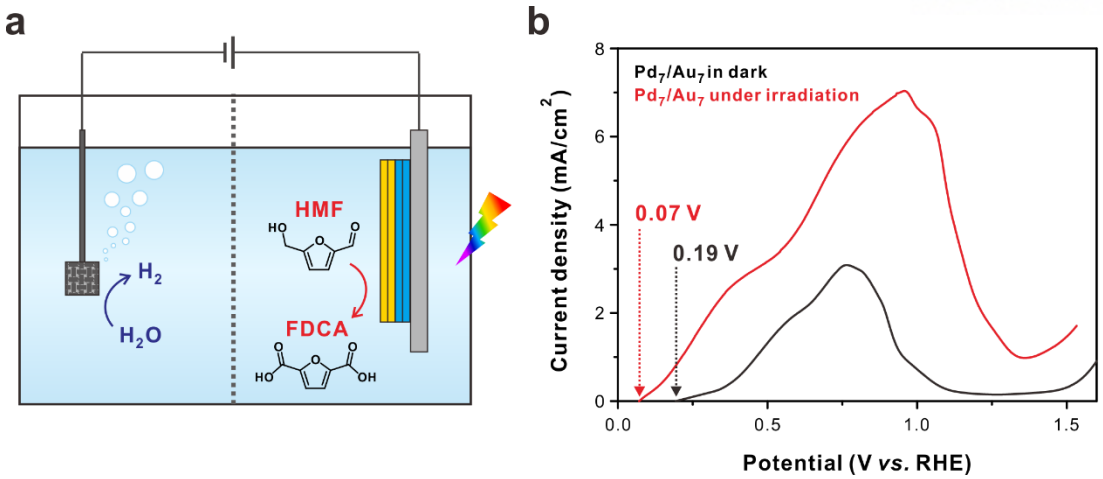

Figure 5.30. (a) Schematic description of photo-electrocatalytic HMF oxidation with Pd_7/Au_7 electrode. (b) LSV curves for HMF oxidation with and without irradiation.

5.3.5. Conclusion

In summary, we systematically examined LbL-assembled bimetallic electrodes to reveal the architecture–activity relationship for electrochemical biomass reforming and H_2 production. The electrocatalytic activity with LbL-assembled multilayer electrode is mainly governed by the thickness and the architecture of the electrodes, even with the same composition of NPs. In the case of HMF oxidation, while Au NPs are favorable for converting HMF into the intermediate HFCA, Pd NPs can rapidly convert HFCA into the final product FDCA. Thus, the observed product distribution was highly sensitive to the species of the outer layer. Even with the identical composition of NPs, when Au NPs were located at the outer layer, as in the case of Pd_7/Au_7 electrode, the yield of FDCA was higher compared with that for Au_7/Pd_7, due to the enhanced mass transfer of HFCA into inner-layer Pd NPs. In the case of the HER, an architecture with adjacent Pd and Au (fully alternating $(AuPd)_7$ electrode) was highly desirable for the rapid spillover of hydrogen from the Pd NPs to the Au NPs. The $(AuPd)_7$ electrode exhibited a better performance, with a lower overpotential (–0.10 V (*vs.* RHE) at –0.2 mA cm^{-2}) and a higher current density (–8.62 mA cm^{-2} at –0.4 V (*vs.* RHE)), than the other bimetallic electrodes (Pd_7/Au_7 and Au_7/Pd_7).

Furthermore, we fabricated a full-cell electrochemical system with the optimized electrodes for HMF oxidation and the HER. When we combined the Pd_7/Au_7 electrode as the anode and $(AuPd)_7$ as the cathode, the full-cell electrocatalytic performance was successfully maximized with the highest current density (4.54 mA cm^{-2}) among all the assembled combinations of electrodes.

We believe this concept can be potentially extended to combine the HER with many other organic reactions for establishing valuable electrochemical reforming systems. Moreover, our systematic study involving LbL-assembled electrodes can be extended to the rational design of other highly active and selective catalysts for various oxidation reactions in ecofriendly processes.

5.3.6. References

(1) Werpy, T.; Petersen, G. Golden, CO (USA): 2004.

(2) Goldemberg, J., Ethanol for a Sustainable Energy Future. *Science* **2007,** *315*, 808-810.

(3) Ermakova, M. A.; Ermakov, D. Y.; Kuvshinov, G. G., Effective Catalysts for Direct Cracking of Methane to Produce Hydrogen and Filamentous Carbon: Part I. Nickel Catalysts. *Appl. Catal. A* **2000,** *201*, 61-70.

(4) Jin, H.; Wang, J.; Su, D.; Wei, Z.; Pang, Z.; Wang, Y., In Situ Cobalt–Cobalt Oxide/N-Doped Carbon Hybrids as Superior Bifunctional Electrocatalysts for Hydrogen and Oxygen Evolution. *J. Am. Chem. Soc.* **2015,** *137*, 2688-2694.

(5) Jiang, N.; You, B.; Sheng, M.; Sun, Y., Electrodeposited Cobalt-Phosphorous-Derived Films as Competent Bifunctional Catalysts for Overall Water Splitting. *Angew. Chem. Int. Ed.* **2015,** *54*, 6251-6254.

(6) Luo, J.; Im, J.-H.; Mayer, M. T.; Schreier, M.; Nazeeruddin, M. K.; Park, N.-G.; Tilley, S. D.; Fan, H. J.; Grätzel, M., Water Photolysis at 12.3% Efficiency Via Perovskite Photovoltaics and Earth-Abundant Catalysts. *Science* **2014,** *345*, 1593.

(7) Zeng, K.; Zhang, D., Recent Progress in Alkaline Water Electrolysis for Hydrogen Production and Applications. *Prog. Energy Combust. Sci.* **2010,** *36*, 307-326.

(8) Liu, J.; Liu, Y.; Liu, N.; Han, Y.; Zhang, X.; Huang, H.; Lifshitz, Y.; Lee, S.-T.; Zhong, J.; Kang, Z., Metal-Free Efficient Photocatalyst for Stable Visible Water Splitting Via a Two-Electron Pathway. *Science* **2015,** *347*, 970.

(9) Take, T.; Tsurutani, K.; Umeda, M., Hydrogen Production by Methanol–Water Solution Electrolysis. *J. Power Sources* **2007,** *164*, 9-16.

(10) Chen, Y. X.; Lavacchi, A.; Miller, H. A.; Bevilacqua, M.; Filippi, J.; Innocenti, M.; Marchionni, A.; Oberhauser, W.; Wang, L.; Vizza, F., Nanotechnology Makes Biomass Electrolysis More Energy Efficient Than Water Electrolysis. *Nat. Commun.* **2014,** *5*, 4036.

(11) Zhao, X.; Dai, L.; Qin, Q.; Pei, F.; Hu, C.; Zheng, N., Self-Supported 3d PdCu Alloy Nanosheets as a Bifunctional Catalyst for Electrochemical Reforming of Ethanol. *Small* **2017,** *13*, 1602970.

(12) Schalenbach, M.; Carmo, M.; Fritz, D. L.; Mergel, J.; Stolten, D., Pressurized PEM Water Electrolysis: Efficiency And gas Crossover. *Int. J. Hydrog. Energy* **2013,** *38*, 14921-14933.

(13) Yu, Z.-Y.; Lang, C.-C.; Gao, M.-R.; Chen, Y.; Fu, Q.-Q.; Duan, Y.; Yu, S.-H., Ni–Mo–O Nanorod-Derived Composite Catalysts for Efficient Alkaline Water-to-Hydrogen Conversion Via Urea Electrolysis. *Energy Environ. Sci.* **2018,** *11*, 1890-1897.

(14) van Putten, R.-J.; van der Waal, J. C.; de Jong, E.; Rasrendra, C. B.; Heeres, H. J.; de Vries, J. G., Hydroxymethylfurfural, a Versatile Platform Chemical Made from Renewable Resources. *Chem. Rev.* **2013,** *113*, 1499-1597.

(15) Bozell, J. J.; Petersen, G. R., Technology Development for the Production of Biobased Products

from Biorefinery Carbohydrates—the Us Department of Energy's "Top 10" Revisited. *Green chem.* **2010,** *12*, 539-554.

(16) Saha, B.; Dutta, S.; Abu-Omar, M. M., Aerobic Oxidation of 5-Hydroxylmethylfurfural with Homogeneous and Nanoparticulate Catalysts. *Catal. Sci. Technol.* **2012,** *2*, 79-81.

(17) Siyo, B.; Schneider, M.; Radnik, J.; Pohl, M.-M.; Langer, P.; Steinfeldt, N., Influence of Support on the Aerobic Oxidation of HMF into FDCA over Preformed Pd Nanoparticle Based Materials. *Appl. Catal. A* **2014,** *478*, 107-116.

(18) Davis, S. E.; Houk, L. R.; Tamargo, E. C.; Datye, A. K.; Davis, R. J., Oxidation of 5-Hydroxymethylfurfural over Supported Pt, Pd and Au Catalysts. *Catalysis Today* **2011,** *160*, 55-60.

(19) Mishra, D. K.; Lee, H. J.; Kim, J.; Lee, H.-S.; Cho, J. K.; Suh, Y.-W.; Yi, Y.; Kim, Y. J., $MnCo_2O_4$ Spinel Supported Ruthenium Catalyst for Air-Oxidation of HMF to FDCA under Aqueous Phase and Base-Free Conditions. *Green chem.* **2017,** *19*, 1619-1623.

(20) Kwon, Y.; Schouten, K. J. P.; van der Waal, J. C.; de Jong, E.; Koper, M. T. M., Electrocatalytic Conversion of Furanic Compounds. *ACS Catal.* **2016,** *6*, 6704-6717.

(21) Kwon, Y.; Birdja, Y. Y.; Raoufmoghaddam, S.; Koper, M. T. M., Electrocatalytic Hydrogenation of 5-Hydroxymethylfurfural in Acidic Solution. *ChemSusChem* **2015,** *8*, 1745-1751.

(22) Chadderdon, D. J.; Xin, L.; Qi, J.; Qiu, Y.; Krishna, P.; More, K. L.; Li, W., Electrocatalytic Oxidation of 5-Hydroxymethylfurfural to 2,5-Furandicarboxylic Acid on Supported Au and Pd Bimetallic Nanoparticles. *Green chem.* **2014,** *16*, 3778-3786.

(23) You, B.; Jiang, N.; Liu, X.; Sun, Y., Simultaneous H_2 Generation and Biomass Upgrading in Water by an Efficient Noble-Metal-Free Bifunctional Electrocatalyst. *Angew. Chem. Int. Ed.* **2016,** *55*, 9913-9917.

(24) You, B.; Liu, X.; Jiang, N.; Sun, Y., A General Strategy for Decoupled Hydrogen Production from Water Splitting by Integrating Oxidative Biomass Valorization. *J. Am. Chem. Soc.* **2016,** *138*, 13639-13646.

(25) Song, F.; Li, W.; Yang, J.; Han, G.; Liao, P.; Sun, Y., Interfacing Nickel Nitride and Nickel Boosts Both Electrocatalytic Hydrogen Evolution and Oxidation Reactions. *Nat. Commun.* **2018,** *9*, 4531.

(26) You, B.; Liu, X.; Liu, X.; Sun, Y., Efficient H_2 Evolution Coupled with Oxidative Refining of Alcohols Via a Hierarchically Porous Nickel Bifunctional Electrocatalyst. *ACS Catal.* **2017,** *7*, 4564-4570.

(27) Luo, J.; Cote, L. J.; Tung, V. C.; Tan, A. T. L.; Goins, P. E.; Wu, J.; Huang, J., Graphene Oxide Nanocolloids. *J. Am. Chem. Soc.* **2010,** *132*, 17667-17669.

(28) Gittins, D. I.; Caruso, F., Spontaneous Phase Transfer of Nanoparticulate Metals from Organic to Aqueous Media. *Angew. Chem. Int. Ed.* **2001,** *40*, 3001-3004.

(29) Gu, M.; Kim, B.-S., Unraveling the Importance of Controlled Architecture in Bimetallic Multilayer Electrode toward Efficient Electrocatalyst. *Nano Energy* **2016,** *30*, 658-666.

(30) Gu, M.; Choi, J.; Lee, T.; Park, M.; Shin, I.-S.; Hong, J.; Lee, H.-W.; Kim, B.-S., Diffusion Controlled Multilayer Electrocatalysts Via Graphene Oxide Nanosheets of Varying Sizes. *Nanoscale* **2018,** *10*, 16159-16168.

(31) Lee, T.; Min, S. H.; Gu, M.; Jung, Y. K.; Lee, W.; Lee, J. U.; Seong, D. G.; Kim, B.-S., Layer-by-Layer Assembly for Graphene-Based Multilayer Nanocomposites: Synthesis and Applications. *Chem. Mater.* **2015,** *27*, 3785-3796.

(32) Ahn, E.; Lee, T.; Gu, M.; Park, M.; Min, S. H.; Kim, B.-S., Layer-by-Layer Assembly for Graphene-Based Multilayer Nanocomposites: The Field Manual. *Chem. Mater.* **2017,** *29*, 69-79.

(33) Ahn, E.; Gaiji, H.; Kim, T.; Abderrabba, M.; Lee, H.-W.; Kim, B.-S., Graphene Oxide Nanosheet as a Two-Dimensional Polyelectrolyte: pH-Responsive Behavior of a Multilayered Nanomembrane. *J. Membr. Sci.* **2019,** *585*, 191-198.

(34) Ardemani, L.; Cibin, G.; Dent, A. J.; Isaacs, M. A.; Kyriakou, G.; Lee, A. F.; Parlett, C. M. A.; Parry, S. A.; Wilson, K., Solid Base Catalysed 5-HMF Oxidation to 2,5-FDCA over Au/Hydrotalcites: Fact or Fiction? *Chem. Sci.* **2015,** *6*, 4940-4945.

(35) McKenna, S. M.; Mines, P.; Law, P.; Kovacs-Schreiner, K.; Birmingham, W. R.; Turner, N. J.; Leimkühler, S.; Carnell, A. J., The Continuous Oxidation of HMF to FDCA and the Immobilisation and Stabilisation of Periplasmic Aldehyde Oxidase (PaoABC). *Green chem.* **2017,** *19*, 4660-4665.

(36) Ahn, E.; Kim, B.-S., Multidimensional Thin Film Hybrid Electrodes with MoS_2 Multilayer for Electrocatalytic Hydrogen Evolution Reaction. *ACS Appl. Mater. Interfaces* **2017,** *9*, 8688-8695.

(37) Huang, D.; Lu, J.; Li, S.; Luo, Y.; Zhao, C.; Hu, B.; Wang, M.; Shen, Y., Fabrication of Cobalt Porphyrin. Electrochemically Reduced Graphene Oxide Hybrid Films for Electrocatalytic Hydrogen Evolution in Aqueous Solution. *Langmuir* **2014,** *30*, 6990-6998.

(38) Li, Y.; Wang, H.; Xie, L.; Liang, Y.; Hong, G.; Dai, H., MoS_2 Nanoparticles Grown on Graphene: An Advanced Catalyst for the Hydrogen Evolution Reaction. *J. Am. Chem. Soc.* **2011,** *133*, 7296-7299.

(39) Sheng, W.; Myint, M.; Chen, J. G.; Yan, Y., Correlating the Hydrogen Evolution Reaction Activity in Alkaline Electrolytes with the Hydrogen Binding Energy on Monometallic Surfaces. *Energy Environ. Sci.* **2013,** *6*, 1509-1512.

(40) Seh, Z. W.; Kibsgaard, J.; Dickens, C. F.; Chorkendorff, I.; Nørskov, J. K.; Jaramillo, T. F., Combining Theory and Experiment in Electrocatalysis: Insights into Materials Design. *Science* **2017,** *355*, eaad4998.

(41) Allara, D. L.; Baca, A.; Pryde, C. A., Distortions of Band Shapes in External Reflection Infrared Spectra of Thin Polymer Films on Metal Substrates. *Macromolecules* **1978,** *11*, 1215-1220.

(42) Łukaszewski, M.; Czerwiński, A., Selected Electrochemical Properties of Pd–Au Alloys: Hydrogen Absorption and Surface Oxidation. *J. Solid State Electr.* **2008,** *12*, 1589-1598.

(43) Al-Odail, F. A.; Anastasopoulos, A.; Hayden, B. E., The Hydrogen Evolution Reaction and Hydrogen Oxidation Reaction on Thin Film PdAu Alloy Surfaces. *Phys. Chem. Chem. Phys.* **2010,** *12*,

11398-11406.

(44) Guo, R.; Xu, X.; Xia, Y.; Huang, W.; Li, Z.; Teng, B., Insights into Electrocatalytic Hydrogen Evolution Reaction in Acidic Medium at in-Situ Dispersed Pt Atoms on Nanoporous Gold Films. *J. Catal.* **2018,** *368*, 379-388.

(45) Devanathan, M. A. V.; Stachurski, Z.; Tompkins, F. C., The Adsorption and Diffusion of Electrolytic Hydrogen in Palladium. *P. Roy. Soc. Lond. A* **1962,** *270*, 90-102.

(46) Cornejo-Romero, J.; Solis-Garcia, A.; Vega-Diaz, S. M.; Fierro-Gonzalez, J. C., Reverse Hydrogen Spillover During Ethanol Dehydrogenation on TiO_2-Supported Gold Catalysts. *Molecular Catal.* **2017,** *433*, 391-402.

(47) Conner, W. C.; Falconer, J. L., Spillover in Heterogeneous Catalysis. *Chem. Rev.* **1995,** *95*, 759-788.

(48) Vayssilov, G. N.; Rösch, N., Reverse Hydrogen Spillover in Supported Subnanosize Clusters of the Metals of Groups 8 to 11. A Computational Model Study. *Phys. Chem. Chem. Phys.* **2005,** *7*, 4019-4026.

(49) Lucci, F. R.; Darby, M. T.; Mattera, M. F. G.; Ivimey, C. J.; Therrien, A. J.; Michaelides, A.; Stamatakis, M.; Sykes, E. C. H., Controlling Hydrogen Activation, Spillover, and Desorption with Pd–Au Single-Atom Alloys. *J. Phys. Chem. Lett.* **2016,** *7*, 480-485.

(50) Clavero, C., Plasmon-Induced Hot-Electron Generation at Nanoparticle/Metal-Oxide Interfaces for Photovoltaic and Photocatalytic Devices. *Nat. Photonics* **2014,** *8*, 95.

(51) DuChene, J. S.; Sweeny, B. C.; Johnston-Peck, A. C.; Su, D.; Stach, E. A.; Wei, W. D., Prolonged Hot Electron Dynamics in Plasmonic-Metal/Semiconductor Heterostructures with Implications for Solar Photocatalysis. *Angew. Chem. Int. Ed.* **2014,** *53*, 7887-7891.

(52) Sousa-Castillo, A.; Comesaña-Hermo, M.; Rodríguez-González, B.; Pérez-Lorenzo, M.; Wang, Z.; Kong, X.-T.; Govorov, A. O.; Correa-Duarte, M. A., Boosting Hot Electron-Driven Photocatalysis through Anisotropic Plasmonic Nanoparticles with Hot Spots in Au–TiO_2 Nanoarchitectures. *J. Phys. Chem. C* **2016,** *120*, 11690-11699.

Chapter 6. Summary and Outlook

This thesis describes new approaches to develop graphene-based nanomaterials and their practical applications in various fields. The presence of various functional groups renders GO as an excellent platform for hosting or growing other functional materials through chemical modification including covalent or noncovalent functionalization. For example, diverse functionalities can be achieved by the chemical modification of GO, making it easy to host and grow functional nanomaterials on the surface of graphene. Based on this technique, we report various approaches to synthesize uniquely functionalized GO-derivatives. Moreover, we have explored their potential uses as additives in non-aqueous suspensions, carbocatalysts for biomass reforming, and electrocatalysts for oxygen reduction, hydrogen evolution, and biomass reforming reaction. We anticipate that this thesis will provide a versatile strategy for the customization of GO-derivatives to achieve high performances in desirable applications through the appropriate choice of functional moieties.

GO-based nanomaterials can also be hybridized with novel nanomaterials not only using chemical modification, but through an LbL assembly method. LbL assembly has great advantages to allow the precise control of multilayer films and to obtain structural insight on engineered composites. In this thesis, we systematically examined LbL-assembled bimetallic electrodes to reveal the architecture–activity relationship for electrochemical reactions. The internal architecture of the LbL-assembled multilayer electrodes could be precisely controlled and their electrocatalytic performance could be modified by changing the nanoarchitecture of the electrode, including the thickness and position of the metal nanoparticles (NPs). Interestingly, even with a composition of the identical constituent NPs, the electrodes exhibited highly tunable electrocatalytic performance depending on their structures.

Based on this systematic study involving customized GO-derivatives and LbL-assembled films, we believe graphene-based nanomaterials can be extended to the rational design of other efficient utilizations for a wide range of fields.

List of Publications

(Currently, November 2019)

†These authors contributed equally to this work.

1) **Minju Park**,† Minsu Gu,† and Byeong-Su Kim*, "Tailorable Bifunctional Electrochemical Biomass Reforming and H_2 Production: Architecture–Performance Relationship in Bimetallic Multilayer Electrodes" **2019**, under review

2) **Minju Park**, Joonhee Lee, and Byeong-Su Kim*, "Bifunctional Graphene Based Carbocatalysts to Reform Biomass from Glucose to 5-Hydroxymethylfurfural" **2019**, under review

3) Dongki Hong, Yuri Choi, Jaegeon Ryu, Jinhong Mun, Wooyeong Choi, **Minju Park**, Yongwon Lee, Nam-Soon Choi, Geunsik Lee*, Byeong-Su Kim*, and Soojin Park*, "Homogeneous Li deposition through the control of carbon dot assisted Li dendrite morphology for high-performance Li metal batteries" *J. Mater. Chem. A*, **2019**, *7*, 20325-20334

4) Katsuhiko Ariga*, Eungjin Ahn, **Minju Park**, and Byeong-Su Kim*, "Layer-by-Layer Assembly: Recent Progress from Layered Assembly to Layered Nanoarchitectonics" *Chem. Asian J.*, **2019**, *14*, 2553-2566

5) Dongseok Kim,† Minsu Gu,† **Minju Park**,† Taehyung Kim,† and Byeong-Su Kim*, "Layer-by-Layer Assembly for Photoelectrochemical Nanoarchitectonics*" Mol. Syst. Des. Eng.*, **2019**, *4*, 65-77

6) Minsu Gu*, Jaewon Choi, Taemin Lee, **Minju Park**, Ik-Soo Shin, Jinkee Hong, Hyun-Wook Lee, and Byeong-Su Kim*, "Diffusion controlled multilayer electrocatalysts via graphene oxide nanosheets of varying sizes" *Nanoscale*, **2018**, *10*, 16159–16168

7) Eungjin Ahn,† Minsu Gu,† **Minju Park**,† Taemin Lee,† Sa Hoon Min,† and Byeong-Su Kim*, "Layer-by-Layer Assembly for Graphene-Based Multilayer Nanocomposites: The Field Manual" *Chem. Mater.*, **2017**, *29*, 69-79

8) **Minju Park**, Kyonghwa Song, Taemin Lee, JinHyeok Cha, InWoong Lyo, and Byeong-Su Kim*, "Tailoring Graphene Nanosheets for Highly Improved Dispersion Stability and Quantitative Assessment in Non-Aqueous Solvent" ACS Appl. Mater. Interfaces, 2016, 8, 21595–21602

9) **Minju Park**,† Taemin Lee,† and Byeong-Su Kim*, "Covalent Functionalization Based Heteroatom Doped Graphene Nanosheet as a Metal-Free Electrocatalyst for Oxygen Reduction Reaction" *Nanoscale*, **2013**, *5*, 12255-12260

Acknowledgements

설렘과 꿈을 안고 UNIST에 처음 발을 들인 후 어느덧 10년이라는 세월이 지났습니다. 2기 입학생으로 들어와 많은 우여곡절을 겪었지만 학교와 함께 성장할 수 있음에 뿌듯하고 보람찼습니다. 좋은 시설과 환경으로 많은 것을 누리며 연구에 매진할 수 있도록 도와준 모교에 감사합니다.

학위 논문을 준비하며 처음 연구실에 들어왔을 때의 기억들을 더듬어보게 되었습니다. 2011년 12월 26일 학부 인턴십 프로그램으로 처음 KBS group 가족이 된 후 벌써 8년이라는 시간이 흘렀네요. 들어온 지가 정말 엊그제 같은데, 이제는 Ph.D 라는 무거운 학위증을 들고 졸업한다는 것이 실감이 잘 나지 않습니다. 긴 시간 동안 많은 분들의 격려와 도움이 있었기에 잘 끝마칠 수 있었습니다. 가장 먼저 저의 지도 교수님이신 김병수 교수님께 감사의 말씀을 드립니다. 교수님과 저와의 인연은 참 깊었던 것 같아요. UNIST 학부 입시 면접에서 처음 뵌 후 입학 후에도 먼저 알아 봐주셔서 정말 감사했습니다. 유기화학과 무기화학도 잘 구분하지 못하던 학부생이 교수님의 유기화학 수업을 듣고 흠뻑 반해 KBS group의 문을 두드리게 되었고, 늘 다정하고 세심하게 지도해주셔서 감사합니다. 교수님 덕분에 학부생 시절에 논문 성과도 내어보고 이렇게 연구자의 길로 들어설 수 있었습니다. 앞으로 더욱 성장하여 멋진 연구자의 모습으로 훗날 다시 찾아 뵐 수 있었으면 좋겠습니다.

학위 논문을 심사해주신 UNIST 이동욱 교수님, 송현곤 교수님, 김건태 교수님, 류정기 교수님 감사합니다. 디펜스가 끝난 후 “박박사 축하하네” 라고 말씀해 주셨을 때 그 뭉클함을 간직하고 초심을 잃지 않는 연구자가 되겠습니다. 그리고 싱가폴에서 연구할 수 있는 기회를 주셨던 싱가폴 국립 대학 Kian Ping Loh 교수님 감사합니다.

긴 시간동안 KBS group에서 함께할 수 있었던 구성원분들께도 감사합니다. 연구실의 오랜 화석이었던 만큼 고마운 사람들과 전하고 싶은 말이 너무나도 많지만 줄여서 몇 자 적어봅니다. 먼저 처음 랩실에 들어와 철없던 저희들을 맞아주신 서은용 박사님, 이태민 박사님, 최유리박사님 감사합니다. 선배님들께서 잘 일구어 놓은 연구실에서 덕분에 편하게 연구할 수 있었습니다. 필재오빠, 수은언니, 은경언니, 은희언니, 수현오빠 늘 연구실 막내를 잘 챙겨주셔서 감사했습니다.

머나먼 미국땅에서 열심히 공부하고 있는 기영오빠, 학부생 때부터 오빠는 정말 똑똑하고 아는 것 많은 사람이라 생각했는데, 타국에서 열심히 박사과정 하시는 모습 보니 역시! 라는 생각이 드네요. 훗날 꼭 성공할 자신이 있다던 자신감 넘치던 오빠 모습이 몇 년이 지난 지금도 잊혀지지 않아요. 저도 분명 오빠라면 그렇게 될 거라 믿고 있습니다. 학부 시절부터 오랜 기간 보아 온 응진오빠, 학위 기간 내내 고민 있을 때마다 제 징징거림을 받아주시고 항상 친동생처럼 아낌없는 조언과 응원 주심에 감사했습니다. 덕분에 고민이 있으면 가장 먼저 오빠를 찾았던 것 같아요. 미국에서의 연구들도 좋은 결과 있으시길 바라겠습니다. 카본팀의 정신적지주 민수오빠, 학부생 때는 오빠하면 가장 먼저 축구인의 이미지가 떠올랐는데 이제는 어엿한 연구자로서 축구할 때 열정적이었던 에너지를 멋진 연구 결과들로 보여주셔서 저도 참 본받고 싶다는 생각이 많이 듭니다. 같이 연구 진행하면서도 많이 배우고 있어요. 멀리 떨어져 있지만 앞으로도 재밌는 연구들 같이 할 수 있었으면 좋겠습니다. 밝은 에너지의 대명사 이슬언니, 다사다난한 일들이 참 많았지만 늘 밝은 모습으로 친구처럼 잘 챙겨주셔서 감사했습니다. 갑작스럽게 떠나셔서 제대로 인사도 나누지 못하고 아쉽지만 앞으로 언니의 앞길에는 행복한 일들만 가득하기를 바랍니다.

동기로 입학했던 병호! 너가 석사로 전환한다고 했을 때 어찌나 아쉬웠는지. 지금은 잘 돼서 너무

축하한다. 늘 실험실의 궂은일을 묵묵히 맡아 하는 너를 보며 동기였지만 많이 배우고 참 고마웠어. 졸업 후에도 가난한 대학원생들을 위해 늘 먼 길 찾아와주고 술까지 사주는 당신은 천사.. 이 은혜는 꼭 잊지 않겠어. 준희오빠! 저희가 드디어 졸업을 하게 되었습니다!! 이 기쁨을 함께 누릴 수 있어 너무 기쁘네요. 까탈스러운 저와는 다르게 세심하고 다정한 오빠를 동기로 만난 것은 정말 행운이라고 생각해요. 같이 연구를 할 기회는 많이 없었지만, 졸업 전 오빠와 이름이 같이 들어간 논문도 써볼 수 있어서 참 의미있었습니다. 셋 다 떨어져 있지만 졸업 후에도 동기 모임 계속 하는거죠?

석사 졸업 후 멋진 직장인으로 성장한 영규, 재은, 해리, 균혁, 송아 석사기간 동안 고생 많았고, 다들 좋은 곳에서 잘 지내는 모습 보기 좋아. 그리고 태형이, 민성이! 연대까지 이사하느라 정말정말 고생 많았어. 선배로서 잘 챙겨주지 못하는 것 같아 늘 미안한 마음과 고마운 마음. 너희는 똑똑하고 열심히 하니 멋지게 박사과정 끝마칠 거라고 믿어. 태형아 앞으로 카본팀의 미래는 너에게 달렸다. 민성이 처음 방장할 때는 너무 착해서 잘 할 수 있으려나 걱정했는데 이제는 어엿한 방장! 너무 스트레스 받지 말고 이 또한 지나가리라 생각하면 편할거야. 준희 오빠의 뒤를 이어 고분자팀을 잘 이끌어 나가길. 윤경이 은별이 같이 연대에 오지는 못했지만 앞으로 더 좋은 소식 들리길 기다릴게. 듬직한 동석이 다른 곳에서도 박사 생활 잘 할거라 믿는다. 나중에 학회에서 만나도 모르는 척 하기 없기. 어느덧 카리스마 넘치는 선배가 된 영주, 그리고 늘 긍정 에너지가 넘치는 소희. 더운 여름날 같이 이사하느라 정말 고생했어! 너희가 없었다면 정말 힘들었을 거야. 새롭게 들어온 기환이, 일오, 주원이, 수빈이도 남은 기간 후회없이 연구실 생활 잘 하기를! 모두들 사회에 나가서도 좋은 인연으로 만날 수 있었으면 좋겠습니다.

또 대학원 생활을 핑계로 살뜰히 챙기지 못했음에도 늘 먼저 연락해주고 찾아주는 고등학교 친구들 민화, 수진이, 예진이, 초등학교때부터 함께한 동현이, 경모, 창멤버 명현이, 익진이, 사촌이자 친구인 인호, 대학교 동기들 성은이, 지영이, 현탁이, 영원한 술팸 멤버들 샘물이, 채웅이, 동협이 고맙다. 각자의 자리에서 모두들 열심히 살고 있는 것 같아 기쁩니다.

마지막으로 가장 고마운 우리 가족들. 엄마, 아빠, 수오! 욕심 많은 딸이 오랜 시간 공부에 매진했음에도 단 한번도 쓴 소리 없이 서포트 해주신 부모님께 무엇보다도 큰 감사를 드립니다. 언제나 저를 믿어주셨기에 이렇게 학위과정을 무사히 끝마칠 수 있었습니다. 오래오래 건강하고 행복하게 제 곁에 계셔 주셨으면 합니다. 사랑합니다.

박사 학위를 받고 난 후에는 무엇이든 잘 아는 척척박사가 되어 있을 줄 알았는데, 이제서야 연구를 어떻게 해야 하는지 깨우쳐 나가고 있는 듯합니다. 학위 기간 동안의 경험들을 바탕으로 부족하지만 독립된 연구자로서의 길을 걸어가고자 합니다. 더욱 성장하는 모습 보여드리도록 하겠습니다. 다시 한번 모든 분들께 감사의 말씀을 전합니다.

2019년 12월 박민주